The Diagnosis of Electronegative Magnetron Plasmas

Thesis submitted in accordance with the requirements of the University of Liverpool for the degree of Doctor in Philosophy

by

Steven Christopher Scribbins

September 16, 2014

ACKNOWLEDGEMENTS

Acknowledgement must be given to a number of individuals whose assistance enabled the successful completion of this work. The author would like to thank the Ph.D. supervisor, Prof. James Bradley, as well as Dr. Paul Bryant, John Lynch, Alan Edwards, Alan Roby, Bernd Liebig, Michael Bowes, Thomas Petty and Frédéric Moix (all of the University of Liverpool), Dr. Robert Dodd (of the University of Nottingham, formerly University of Liverpool) and Dr. Roy McAdams (of CCFE) for their kind assistance.

This work was part-funded by the RCUK Energy Programme under grant EP/I501045 and the European Communities under the contract of Association between EURATOM and CCFE. The views and opinions expressed herein do not necessarily reflect those of the European Commission.

Contents

List of Contributions

Publications

- The spatial distribution of negative oxygen ion densities in a dc reactive magnetron discharge 2013 *J. Phys. D: Appl. Phys.* **46** 045203

Oral presentations

- 2-D Spatial distributions of negative oxygen (O-) ion densities and other plasma properties in a reactive DC magnetron; Society of Vacuum Coaters Annual TechCon 2012, Santa Clara, California.

Poster presentations

- Spatial distribution of negative oxygen (O-) ion density in a reactive dc magnetron determined using laser photodetachment; 13th International Conference on Plasma Surface Engineering, 2012, Garmisch-Partenkirchen, Germany.
- Spatial distribution of plasma properties in a reactive dc magnetron, determined using laser photodetachment and Langmuir probing; Institute of Physics Plasma Conference 2012, Oxford, UK.

List of Figures

List of Tables

Chapter 1

Introduction

The magnetron sputtering tool has existed in various forms since the early 1960's [1], and has since that time developed into a widely used device for the production of engineering-quality thin films and coatings on substrate surfaces [2]. The versatility of the magnetron has seen it become the subject of a great deal of study, ultimately allowing the magnetron to be used with a high degree of precision and control to lay down a wide variety of different surfaces and coatings. There are two basic types of magnetron device, classified as 'balanced' (type 1) and 'unbalanced' (type 2). The conventional type 1 case operates using a magnetic field structure where the magnetic null point in this geometry is high above the target surface. In this configuration, the plasma electrons are unlikely to escape the magnetic trap, and the ion flux to a substrate positioned above the null is low. The unbalanced (type 2) magnetron, first developed by Window and Savvides in 1986 [3], is constructed with the null-point of the magnetic geometry much closer to the target surface. The result is that electrons can escape the magnetic trap more easily, and the ion flux to a substrate above the null is greatly enhanced. The magnetron used in this study is of a type 2 unbalanced design.

In addition to the sputtering applications, the tendency of magnetron plasmas to produce negative ion species in reactive discharges allows an opportunity to study hydrogen plasmas which are of interest to the nuclear fusion community. Specifically, any fusion reactor capable of producing commercial electricity is likely to require a negative ion-sourced beam of neutral deuterium atoms [4]. Here, negative deuterium (an isotope of hydrogen) must be produced in large populations in a plasma environment in order to produce high-power neutral beams [5] for the delivery of heating power and fuel to the primary fusion plasma [4, 6]. As such, it is useful to diagnose directly the formation

and behaviour of H^-. Direct measurements of H^- in neutral beam plasmas, however, are relatively sparse, since the research focus (and, consequently, funding) in the fusion community is predominantly directed towards the primary fusion plasma and understanding thereof. While a magnetron is unlikely to be utilised for negative ion production in a fusion context, the laser photodetachment apparatus at Liverpool provides a convenient facility to perform measurements of plasmas which are similar in temperature ($2-5\,\mathrm{eV}$), pressure ($\leq 10\,\mathrm{mTorr}$) and density ($\sim 10^{16}-10^{17}\,\mathrm{m}^{-3}$) to those of a neutral beam source. Therefore, in addition to the considerations relevant to surface engineering fields, this project aims to develop an understanding of the methods of enhancing production of the negative hydrogen (H^-) ion in fusion neutral beam source plasmas for tokamaks.

Various techniques have been suggested for increasing the negative ion yield in low-temperature hydrogen plasmas, which can be investigated in the magnetron environment; in particular, the use of different surface materials (tungsten, tantalum, carbon [7–9]) may play a role in H^- production. Furthermore, spatially and temporally resolving the H^- concentrations under various conditions may provide additional insights. This investigation of hydrogen plasmas is being performed in collaboration with the neutral beams research group at Culham Centre for Fusion Energy (CCFE), where development of the Small Negative Ion Facility (SNIF) has necessitated experimental studies of neutral beam source plasmas in the same or similar environments. At SNIF, direct diagnostic capability is limited by the design of the machine and therefore an effort is being made to utilise the magnetron as a diagnostic device for obtaining data that is relevant to the experimental undertaking at Culham. It is hoped that use of the photodetachment diagnostic to study negative hydrogen ions will yield useful data to assist with further development of SNIF and related projects.

While in general, magnetron sputtering plasmas are well diagnosed and relatively well understood [10], the picture is still incomplete. One particular aspect of magnetron plasma behaviour that is not fully developed is the presence of negatively charged ions in reactive discharges [11]; for example, in oxygen and chlorine plasmas. Negative ions in such plasmas play a role in the growth of thin film coatings manufactured using these gases [12, 13], and may adversely impact the quality of a growing film at the substrate [14–17]. Knowledge of the quantities as well as production, transport and destruction mechanisms of negative ions under different conditions (DC, pulsed-DC, RF and HiPIMS discharges, various powers and pressures) is useful for surface engineering applications. Oxygen, for example, is used in the production of titania (TiO_2), silica (SiO_2), tantalum pentoxide (Ta_2O_5) and

indium-tin-oxide (ITO) for optical applications. Aluminium oxide (Al_2O_3) and Al-doped zinc oxide (ZnO) are also common surface coatings manufactured with magnetrons. Sputtering in oxide plasmas for atomic layer deposition is therefore a convenient industrial process, despite the disadvantages of the presence of negative ions. This project aims to build a more developed understanding of the role and behaviour specifically of negative oxygen (O^-) ions in magnetron sputtering plasmas, by measuring directly their quantities, under various plasma operating conditions resolved spatially and temporally within the plasma, making use of the laser photodetachment technique [18] in conjunction with a Langmuir probe. It is hoped that this information can provide insights into the behaviour of negative ions in reactive magnetron plasmas, to ultimately allow for a greater maniuplation of their role in sputtering applications.

The technique to be employed for these studies is known as laser-induced electron photodetachment. This itself is not a new technique. It has been applied to the measurement of negative ions in various plasmas and sources for some years. Indeed, laser photodetachment of O_2^- was reported as early as 1968 [19]. Equivalently, the use of Langmuir probes as a basic plasma diagnostic dates back to Langmuir himself in the 1920s [20, 21]. The combination of Langmuir probing and laser photodetachment has been extensively used [22], and the eclipse technique was developed by Kajita and Kado in the early 2000's [23, 24]. This combination of techniques provides a useful tool for measuring directly the density of negative ions within a plasma, and is being used at Liverpool for exactly this purpose. At least as far as magnetron devices are concerned, the use of photodetachment to study negative ion densities is unique to Liverpool and this experiment [25, 26]. It therefore provides unique data and insights to the production and transport mechanisms of negative oxygen ion species in magnetrons.

This thesis is split broadly into three parts. In the first part (chapters 2 - 4), the experimental background and experimental setup relevant to the whole project is covered, along with basic characterisation and calibration of the plasma and equipment. In the second part of the thesis (chapters 5 and 6) the study of the time and space-resolved distribution of negative ion densities and other plasma quantities in a typical O_2/Ar magnetron discharge is covered, with consideration given to previous negative ion work by other researchers specific to this magnetron experiment, as well as more general discussion of negative ions in the wider magnetron context. The final part (chapter 7) will cover the study of hydrogen plasmas in the magnetron, with a view to investigating the quantities of negative hydrogen ions produced, as well as briefly discussing the means of increasing the H^- yield.

Chapter 2

Magnetron Background

2.1 The Magnetron Discharge

The magnetron plasma discharge is a magnetically enhanced DC glow discharge, in which the plasma is sustained by the emission of secondary electrons due to ion impacts on the cathode surface. In a simple diode glow discharge, electrons with energies above a certain threshold emitted from a cathode collide with neutral gas atoms, causing ionisation of these atoms and the release of further electrons into the plasma. These electrons so liberated can then go on to cause further ionisation events, thus liberating further electrons and so-on. This process is referred to as an *electron avalance* or *cascade*, and, in addition to the cathode potential, is necessary to sustain the plasma. However, in order for this process to work effectively, the plasma must be operated at relatively high pressures (typically 10 mTorr - 10 Torr [27]) which are not ideal for sputtering applications.

In a magnetically enhanced glow discharge - i.e. the magnetron discharge, in which the cathode is also magnetised, these liberated electrons are confined by the magnetic field into a particular region of the plasma (often referred to as a magnetic "trap"). Due to the presence of both an **E**-field and a **B**-field, they experience an $\mathbf{E} \times \mathbf{B}$ drift within this region, causing them to travel along a path dictated by the magnetic field geometry; normally a magnetic 'tunnel' parallel and adjacent to the target [2]. The effect here is to increase the number of ionising collisions which the electrons experience before they escape the plasma, in a region close to the target where the ion species are easily captured by the cathode. As a result, therefore, of undergoing a higher number of ionising events than would otherwise be the

case, the magnetron arrangement is capable of sustaining a plasma at much lower pressures than a simple glow discharge. Furthermore, the fact that such ionisation processes occur in the vicinity of the target allows the plasma ions to be subsequently accelerated through the high cathode fall potential (typically in excess of 300 V) to energies exceeding the sputter threshold of the target material (typically $\sim 10^2$ eV), therefore readily contributing to the sputtering process. When these energetic ion species from the discharge atmosphere impact on the surface of the target, thereby causing sputtering, they can also cause ejection of electrons from the target surface into the plasma. This is known as secondary electron emission. These secondary electrons contribute significantly to plasma ionisation, since they appear in a region where they are easily confined by the magnetic field. In sputtering applications this combination of effects (being able to generate ions capable of exceeding the sputter threshold while maintaining a low pressure discharge) is highly desirable, as any material sputtered from the cathode surface must first traverse the plasma before coming to rest on the substrate where the film is to be grown. Since the mean free path of a particle in a gas (or plasma) environment is a function of the gas (or plasma) pressure, it follows that lower pressure plasmas allow sputtered material to traverse the plasma volume more easily.

It should be noted that in most cases, the first ionisation energy of the source gas atoms is much higher than the electron temperature of the plasma. In the case of argon, for example, the ionisation energy is 15.8eV; this is much higher than the typical electron energy in most gas discharges. As such, it is normally only the high energy tail of the electron energy distribution function which has sufficient energy to contribute to ionisation events. Therefore, the density of ions in a magnetron plasma is typically several orders of magnitude lower than the neutral gas density. In the magnetron case, for example, ion densities are often $\sim 10^{16} - 10^{17}\,\mathrm{m}^{-3}$ where the neutral gas is usually $\sim 10^{19}\,\mathrm{m}^{-3}$ [27].

There are a number of magnetron geometries which are used for sputtering applications. Perhaps the simplest of these is the planar disc geometry. In this example, the cathode is simply a circular disc comprised of whichever material is desired to be sputtered. Directly behind this cathode, an arrangement of permanent magnets is constructed such that a tunnel-like magnetic geometry is formed parallel to the target surface. Figure 2.1 shows a schematic diagram of the magnetron arrangement. Rectangular (or oval) and cylindrical, and multiple-cathode geometries also exist, however an in-depth discussion of these systems is beyond the scope of this project.

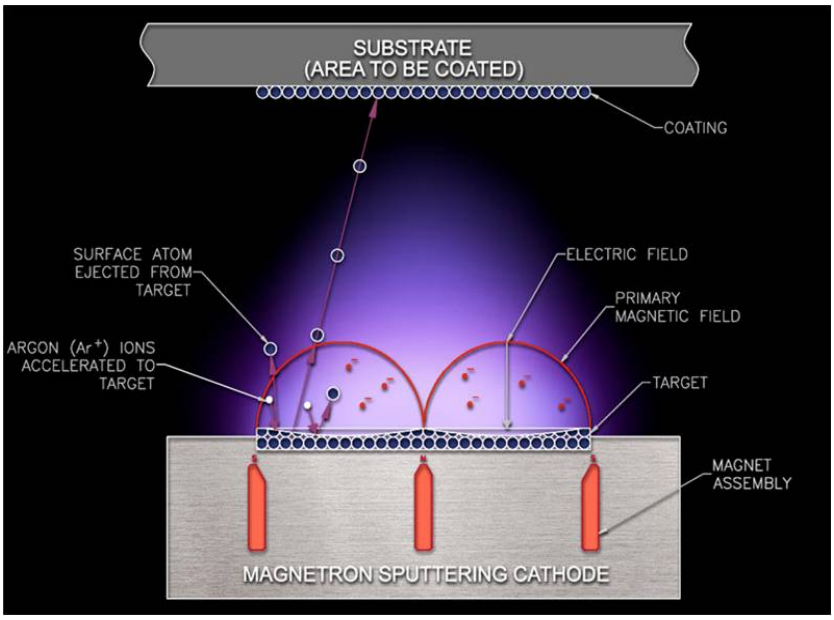

Figure 2.1: Schematic cross-sectional diagram of a circular planar magnetron, showing a summary of the sputtering process

2.2 Overview of Magnetron Phenomena

Over the last 30 years reactive magnetron sputtering has been employed as a tool for the deposition of engineering quality thin films and coatings including a large range of metal oxides [28–31].

There are typically two methods by which stoichiometric metal oxide thin films can be formed at the substrate in these discharges; either to sputter a metal target, (a single element, a combination or doped) in an Ar/O_2 mixture or alternatively to sputter a ceramic target of the required film composition in Ar or Ar/O_2 mixtures.

Since the early work with DC [31] and RF [32] sputtering, many reactive magnetron sputtering processes nowadays employ mid frequency (5-350Hz) pulsed-DC [33] or mid-frequency AC (sinusodial) waveforms [34] for the power delivery. To gain a better understanding of the basic fundamental plasma processes in these magnetised discharges and to characterise their operation, plasma diagnostic tools including Langmuir probing, mass-energy analysis and optical emission spectroscopy have been used [10]. It should be noted that in most magnetron plasmas, only the electrons are considered magnetised. Due to the ion mass being significantly larger than that of electrons, the ion Larmor

radius is typically some tens of centimetres or even metres depending upon position within the plasma and local field strength, making their gyroradius somewhat larger than the typical field gradient scale lengths ($\sim 10^{-2}$ m in the magnetron). As such, the ions are treated as being unmagnetised within the magnetron discharge.

It has been shown through a number of detailed energy-resolved mass spectroscopic studies that the presence of oxygen in the magnetron plasma leads to the formation of negatively charged ions, namely O^-, O_2^- as well as charged metal oxide species MO_x (of the target material). See for example the work of Mráz [35–37], Depla [38–40] and Welzel [41] et al.

These negative ions originate at the cathode target and can be broadly categorised as high, medium and low energy populations [36]. High energy components arriving at the substrate can have energies in excess of say 500 eV. These ions are those that have been created near the target surface by desorption of O^- (or desorption of O followed by electron attachment), and subsequently accelerated across the cathode fall potential and reach the mass analyser with few or no collisions. The medium energy component is generated by sputtering of MO^- or MO_x^- clusters which are then accelerated across the cathode fall and subsequently dissociated by collisions in the plasma bulk. The low energy components are those that have suffered dissociation or multiple scattering events en route to the analyser and the energies at which they are detected are often a clear signature of particular impact events. In particular, these low energy ions are thought to be formed by dissociative attachment of O_2 within the plasma bulk (reaction 1, Table 2.1).

It has been shown that energetic negative ions are accelerated away from the target as beams of ions [38, 39] and are easily capable of overcoming the sheath potential at any substrate, whether electrically biased or isolated (floating) to bombard the growing film. This can cause considerable re-sputtering of the surface [42] so altering the film properties. For instance this process has been seen to lower the refractive index and crystallinity of Al_2O_3 films [39] and increase the resistivity, lower Hall mobility and carrier concentration in Al-doped ZnO films [43].

The mass spectral analysis technique lends itself beautifully to determining the energy distribution of mass-selected negative ions arriving to a surface or substrate. Typically this is the grounded orifice of the analyser itself, often positioned at the substrate position. In some cases the analyser is built into a substrate; however it does not readily provide absolute fluxes nor therefore negative ion densities in the plasma. It also necessarily rejects negative ions with energies below the equivalent of the potential drop across

the ion sheath adjacent to the instrument orifice. This barrier is of the order of the local electron temperature in the bulk plasma, usually 2-4 eV [10]. Therefore negative ions created in the plasma bulk with temperatures close to the neutral gas temperature, through processes such as dissociative electron attachment [27] cannot be observed. Although they do not re-sputter the film, these ions in sufficient quantities can alter the electrical conditions across the plasma and at the plasma-substrate boundaries so changing the ion flux arriving there [44]. Low temperature negative ions have been studied in detail in many other low-pressure electronegative gases (e.g. O_2, F, H, CH) containing plasmas such as RF etching tools [45, 46] and neutral beam sources [47].

	Reaction	**Equation**	**Ref.**
1	Dissociative Attachment	$O_2 + e \longrightarrow O + O^-$	[48]
2	Ion-ion Recombination	$O^- + {O_2}^+ \longrightarrow O + O_2$	[48]
3	Ion-ion Recombination	$O^- + {O_2}^+ \longrightarrow 3\,O$	[48]
4	Ion-ion Recombination	$O^- + O^+ \longrightarrow 2\,O$	[48]

Table 2.1: Dominant chemical reactions involving O^- in the magnetron

2.3 Summary of Previous Work

2.3.1 Initial Photodetachment Experiments

Much of the groundwork for the studies conducted in this project was laid down by R.D. Dodd and S.-D. You *et al.* between 2009 and 2011 [11, 25, 49–52], measuring negative ion densities at various pressures, powers, Ar:O_2 neutral gas ratios and probe biases, as well as at differing distances along the centreline of the plasma and in pulsed mode at fixed postions. In those works, a number of trends were identified in RF, DC and pulsed-DC plasmas.

The early work described in [11] highlighted a trend (in the RF case) of increasing electron density, n_e, and negative ion density, n_-, with total chamber pressure, and a decrease of electron temperature, T_e, with pressure. These trends are unsurprising; T_e decreases with pressure due to enhanced collisional cooling process as a result of the shorter mean free path, and n_e can easily be attributed to the higher ionisation rate of higher pressure plasmas. Both of these trends are well known in magnetrons and other discharges.

The negative ion density in this case is seen to increase with pressure up to a threshold of around 12 mTorr, and then decrease rapidly. This rapid decrease at higher pressure is attributed to reduced sputter yield at higher pressures: as the pressure increases, so too does the extent of target poisoning, therefore reduced quantities of negative species may be being released at the target. This observation, however, is inconsistent with other results [53]. In general, it was found that negative species are produced in considerably greater quantities in RF discharges than in DC; the fraction of negative ions in DC was found to be $\sim 100\times$ less than in RF. It is worth noting, however, that in this work the Langmuir probe was not eclipsed with a blocking wire as in subsequent works due to the authors at the time being unaware of the eclipse technique. As a result saturation of the photodetached current, ΔI_{pd} with increasing laser energy density was not observed. Laser energy density was therefore set in the linear regime in order to prevent overestimation of densities due to probe surface ablation.

Of perhaps greater interest is the outcome of the work published in [25]. O^- densities were measured in the magnetron operating in DC mode at a range of powers, oxygen partial pressures and total pressures at a fixed distance from the cathode, on the centreline of the plasma. Here, a number of interesting results were documented. As discussed in more detail in section 3.2, operation of the laser at 532 nm provides laser photons with sufficient energy to detach electrons from both O^- and $O_2{}^-$. Operating in 1064 nm mode, when the photon energy is sufficient to detach electrons from $O_2{}^-$ but not from O^- revealed that the quantity of $O_2{}^-$ is less than 2% of the total, and as such their presence in the plasma can be ignored. This simplification allows for a much more straightforward interpretation of photodetachment measurements in the oxygen case, when combined with the optimisation of the photodetachment technique as previously discussed.

2.3.2 Effects of varying O_2 content for fixed power and pressure

Dodd *et al.* measured electron densities, temperatures and negative ion densities with varying discharge power, O_2 partial pressure and total pressure, and consequently identified a number of key trends within the plasma. With an optimal set of laser diagnostic and probe parameters (beam radius $R_b = 2$ mm, probe bias $V_b = 30$ V, blocking wire diameter $D_{bw} = 0.38$ mm and laser energy density $E/S = 240\,\mathrm{mJ\,cm^{-2}}$) and power and total pressure fixed at 200W and 10mTorr respectively, the negative ion fraction (electronegativity), α,

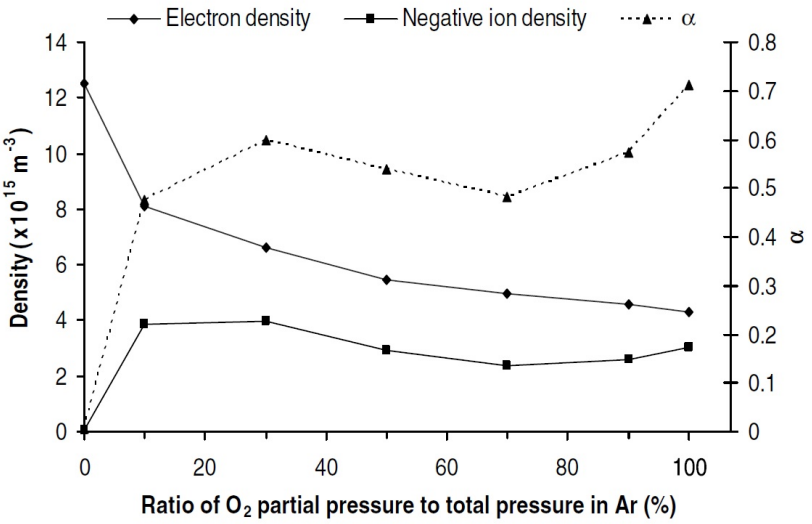

Figure 2.2: A plot of the negative ion density (n), electron density (n_e) and $\alpha(= n/n_e)$ versus the O_2 partial pressure in a 200 W 10 mTorr discharge. Image from [25].

negative ion density, n_-, electron temperature, T_e, local plasma potential, V_p, and electron density, n_e, were plotted as a function of O_2 partial pressure. Negative ion fraction, α, and density, n_-, were both observed to increase sharply as O_2 concentration is increased to 10%, reaching a "broad maximum" from 10-30%, before dipping again to a minimum at 70% O_2 (see figure 2.2).

Despite the observation that n_- reaches a maximum at relatively low oxygen content, and even decreases with higher O_2 partial pressures, electron density was observed to decrease continuously as the oxygen content of the working gas was increased from 0% to 100%. This apparent discrepancy was attributed to a decrease in cathode current which occurs as a result of an increase in target poisoning at higher O_2 concentrations. The decrease in electron density is particularly sharp as the oxygen content increases up to 10%, due to the formation of O^- by dissociative attachment in the bulk plasma (see Table 2.1). Although the electron density is seen to decrease, it was also observed that electron temperature increases roughly linearly with O_2 partial pressure, which may be a consequence of increasing cathode fall potentials with increasing oxygen content, thus leading to higher energy secondary electrons which can more efficiently heat the bulk plasma.

As outlined in [54], mass spectroscopic studies of O_2/Ar discharges with a titanium target showed that both O^+ and $O_2{}^+$ densities increase with

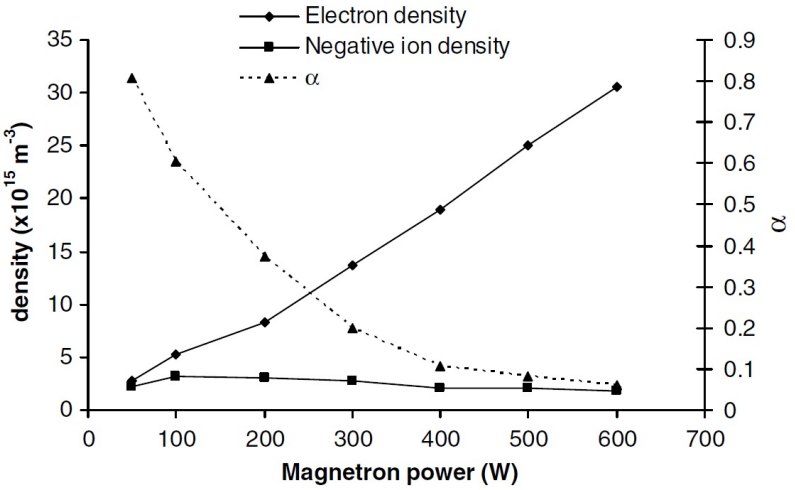

Figure 2.3: A plot of the negative ion density (n), electron density (n_e) and $\alpha(= n/n_e)$ against magnetron power for a 10% O_2 10 mTorr discharge. Image from [25].

increasing O_2 content, and their corresponding ion energy distribution functions showed significant high-energy tails - normally caused by ionisation of high energy sputtered neutrals within the plasma bulk, indicating that a significant fraction of positive oxygen species originate from the poisoned target. Coupled with the fact that the dominant O^- loss mechanisms are ion-ion recombination with these positive species (and with Ar^+ - see section 5.1), this suggests that as O_2 content increases, the destruction rate grows while formation rate falls, leading to an overall decline in O^- density as partial pressure increases above 30%.

2.3.3 Effects of varying discharge power for fixed pressure and O_2 content

With O_2 content set to 10% and a total pressure of 10mTorr, the discharge power was varied in the range 50 W - 600 W. Electron density was found to increase linearly with power, a trend also observed by Straňák *et al.* [55]. While α was found to decrease, negative ion density (see figure 2.3) and electron temperature varied little over the range of powers, with n_- reaching a maximum between 100 W-200 W.

Since the electron density increases with power, the O^- density might also be

expected to rise due to an increased rate of dissociative attachment; however this is not observed. Instead, the quantities of O^+ and $O_2{}^+$ rise with power, leading to the dominant reactions 2, 3 and 4 (Table 2.1) neutrals having greater influence on the O^- concentrations at higher powers. From this it can be inferred that fraction of negative ions with high energies (such as those created at the target) comprise only a small fraction of the total O^- density and consequently that dissociative attachment may be the dominant bulk creation process for negative ions.

The plasma potential is also seen to have a relatively strong dependence on power, evidenced by a decrease over the range of discharge powers. In low power discharges, there is considerably more target poisoning than at higher powers - i.e. the target is covered in an insulating layer of TiO_x - due to lower sputter rate at low power. The sputter rate is known to increase with power, therefore the amount of TiO_x on the target surface can be expected to decrease, while the quantity on the other chamber surfaces can be expected to grow. This shifting of the insulating film from the cathode to the walls can lead to a general decrease in V_p as the plasma electrons are hindered from finding a path to ground.

2.3.4 Effect of varying pressure for fixed power and O_2 content

When power and O_2:Ar ratio were fixed, and total pressure varied from 2-25 mTorr, some interesting results were observed. Perhaps the least surprising of these is the decrease in T_e and V_p with increasing pressure. In weakly ionised low pressure plasmas, the decrease in pressure leads to lower ionisation rates and lower electron densities; thus, the cathode fall and boundary sheaths exhibit higher potential drops (the plasma potential is higher) and therefore there is a greater depth of penetration of electric fields into the plasma volume, which leads in turn to higher temperatures. Negative ion fraction and density are both observed to increase with pressure in [25]. This is consistent with observations made by Stoffels *et al.* [46] in RF plasmas, who identified by modelling the dominant mechanisms of production and loss of O^-: namely, dissociative attachment (reaction 1, Table 2.1) and ion-ion recombination (reactions 2-4, Table 2.1) respectively.

2.3.5 Effect of varying position on the centreline for fixed discharge parameters

In the pulsed-DC case, observations were made by Dodd *et al* [51] at various positions along the centreline of the discharge. The magnetron in that paper was pulsed with a commercial magnetron power supply (Advanced Energy Inc. Pinnacle Plus) operating at typical pulse parameters: namely, a frequency of 100kHz with a fixed average power of 400W. This power supply pulses in a bipolar mode with a positive potential at the target of ∼+30V in the off-time.

The negative ion density in this case was observed to have a strong dependence on position, with peak density $n_- \sim 1 \times 10^{16}\,\mathrm{m}^{-3}$ being observed at a position 75 mm away from the target surface (see figure 2.4). Plasma densities were also observed to have a spatial dependence, although the variation with distance from the target was much less than in the negative ion case. The electron density distribution observed by Dodd (figure 2.5) is known to arise from the magnetic mirroring of electrons in the region of the magnetic null.

O^- density was seen to vary little in time during the on-phase, with a peak immediately after the discharge is struck, declining slowly until the off time, where a small drop is observed. Dodd attributed the consistency of measurements throughout the pulse cycle to the presence of metastable vibrationally-excited O_2 molecules O_2^M, known to have a high electron attachment cross section at temperatures typical of the magnetron discharge [56], within the plasma bulk.

2.3.6 Effect of pulsing the discharge for various duty cycles

In the study described in [49], pulsed discharges that were non-typical of commercial sputtering plasmas were examined in order to gain insights into the reaction chemistry which may be equally applicable at higher powers. A unipolar pulsed discharge was operated for a 50μs on-phase followed by a variable off-phase. Duty cycles of 5%, 12.5%, 25% and 50% were used, with total on-phase power of 100 W, leading to an average power varying from 5 W to 50 W as the duty cycle was increased from 5 to 50%. This experiment was performed for a fixed position in the plasma (75 mm from the target, on the discharge centreline), with O_2 partial pressure set to 10%.

Chief among the findings was the observation that negative ion density is seen to sharply increase in the off-phase of these discharges, and the temporal

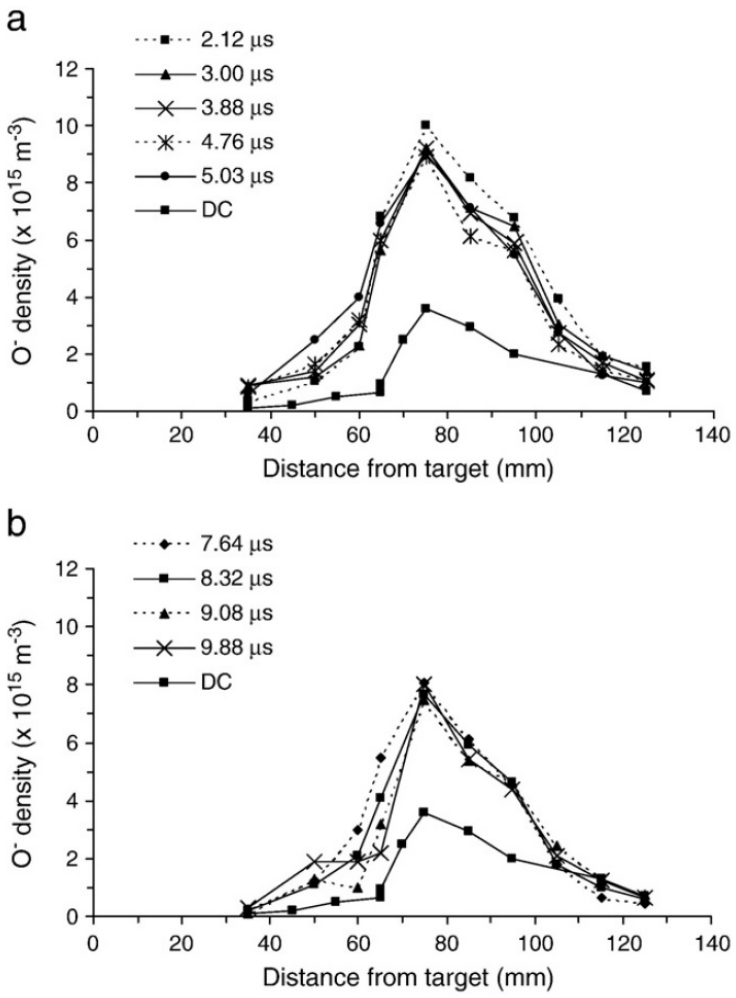

Figure 2.4: A plot of the O^- density against distance along the central axis for a number of chosen times during a) the on-time and b) the off-time. Steady-state measurements made in 200 W DC magnetron conditions are also shown. Image from [51].

evolution of the negative ion density is strongly modulated by the duty cycle, with much higher off-phase O^- densities being observed for higher duty cycles. This is illustrated in figure 2.6. It is suggested that the dependence of n_- on the duty cycle is a result of a build-up of O_2^M within the plasma. If the off-phase duration is long enough for the metastable molecules to be lost to the chamber walls, no build-up is observed, and peak O^- density is not affected by the presence of lingering O_2^M from the previous cycle. If, however, O_2^M molecules produced in the bulk do not have sufficient time to decay before

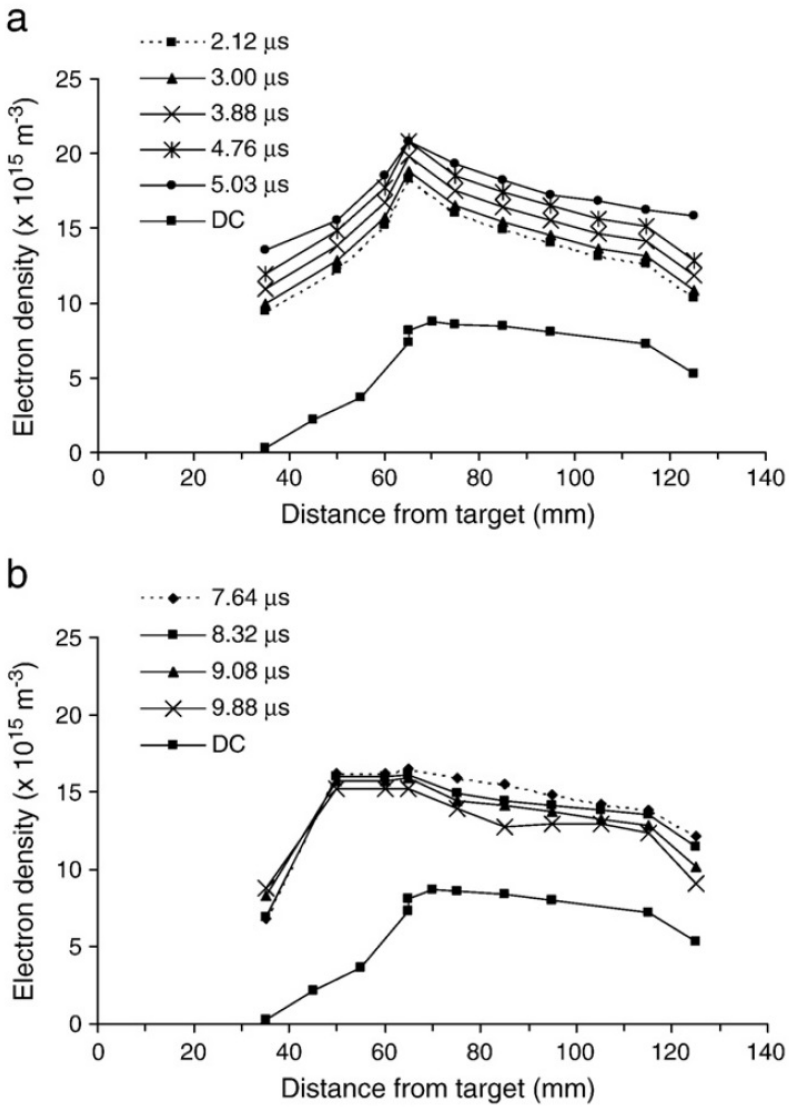

Figure 2.5: Plot of the electron densities against distance along the central axis for a number of chosen times during a) the on-time and b) the off-time. Steady-state measurements made in 200 W DC magnetron conditions are also shown. Image from [51].

the on-phase of the next cycle, this may lead to an increase in O_2^M within the bulk and consequently a higher off-phase O^- density than for longer off-phase durations.

These results indicate a channel for O^- production which is consistent with other papers, and gives strong supporting evidence that O^- is predominantly

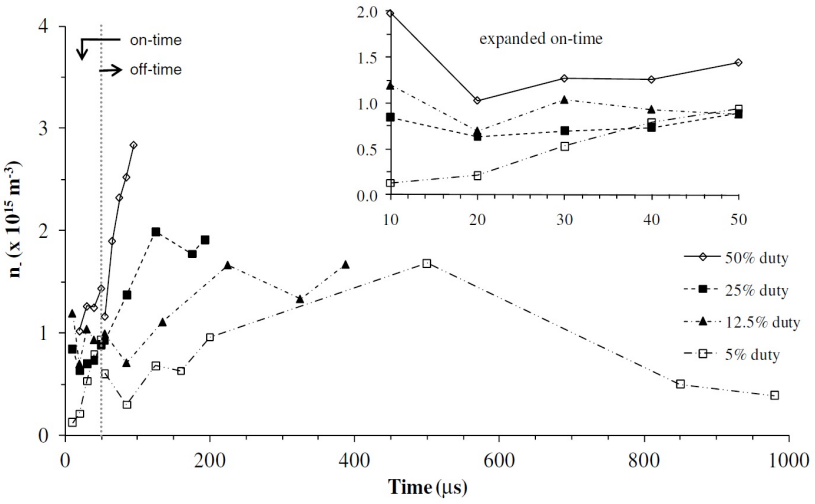

Figure 2.6: The temporal evolution of negative ion (O^-) density for the four chosen duty cycles and for 10% O_2 partial pressure. Image from [49].

produced by dissociative attachment of vibrationally excited metastables in the plasma bulk. Modelling performed by Panda *et al* [48] supports this idea, with the caveat that the O^- densities are particularly sensitive to discharge power, reducing significantly as power is increased. This is thought to be a consequence of enhanced dissociation of O_2 at higher powers, leading to less O_2^M being produced.

This concludes the summary of the uses, principles, reactive applications and negative ion implications relevant to the results discussion in this thesis.

Chapter 3

Experimental Setup

3.1 The Langmuir Probe

The Langmuir probe is a versatile tool for measuring a range of plasma quantities. All Langmuir probe characteristics in this study were collected using a Hiden Analytical Ltd. ESPIon Advanced Langmuir Probe system, and the corresponding ESPSoft control software, and analysis performed using spreadsheet software. Parameters of significance to this study are those of plasma potential V_p, electron temperature T_e, native electron current I at the bias voltage V_b (for calculation of the quantity α after photodetachment) and plasma density n.

Plasma potential in this case is perhaps the least important quantity, as it is estimated only for the purpose of determining the bias to which the probe must be set in order to correctly record the photodetachment current (see section 3.2). Furthermore, it is difficult to measure with accuracy the plasma potential from a Langmuir probe current-voltage characteristic, especially so in the magnetised plasma case due to the rounding of the "knee" which occurs at the plasma potential. The situation is complicated further in the magnetron case, as the sputtering process in oxygen discharges tends to coat the chamber walls in insulating material, resulting in the chamber becoming progressively insulated from ground. This in turn results in a drift of the plasma potential towards more negative values over time, as the electrons are increasingly inhibited from finding a path to ground. The plasma potential, according to theory, is identified by the point at which exponential increase of current in the transition region ceases; that is to say the point at which the electron current saturates, as no further electrons can be collected. In

practice, this is not observed as sheath expansion leads to increasing current as the bias voltage is increased, however it is still possible to estimate the plasma potential in a number of ways. One such method relies on the fact that the plasma potential can be identified mathematically as a turning-point on the $I-V$ plot. As such, it appears as a maximum on a plot of dI/dV, or as a zero crossing-point on a plot of d^2I/dV^2. The capability to differentiate the $I-V$ characteristic is included in the Hiden ESPIon acquisition software (which was used to record the Langmuir probe characteristics in all cases) thus facilitating a convenient method of estimating plasma potential *in situ* without the need for a complete analysis of the characteristic. It should be noted, however, that even this method is not without error - particularly in positions of strong magnetic field, where the knee is indistinct or even obscured completely, the maximum/zero-crossing point can still be difficult to identify.

Electron temperatures used in this study were measured in the conventional way: that is to say, by finding the inverse of the slope of a linear fit to the exponential region on a semilog plot of $\ln(I)$ against V. In most cases in the magnetron, this part of the characteristic is easily identifiable, however again in the case of the more strongly magnetised region, it is considerably less distinct. Nevertheless, the temperature is relatively simple to extract, and provides a useful insight into the plasma behaviour, particularly as it allows identification via rate coefficients of the dominant plasma chemistry for the various particle species.

The plasma density is commonly equated, by the assumption of quasi-neutrality to the electron density n_e, as $n = n_e = n_i$. Typically, the plasma potential and electron temperature are used together to determine this quantity from a Langmuir probe characteristic. The plasma potential, if measured accurately, yields trivially the current at that potential. Using this current, and the thermal speed of the electrons derived from the measured temperature, it is possible to estimate the electron density of the plasma. This method, however, is subject to rather large uncertainty, stemming from the difficulties of accurately measuring plasma potential and temperature from the conventional Langmuir probe. In many cases, densities, temperatures and plasma potentials are not sought using the Langmuir probe, as other diagnostics (for example Thompson scattering, or a hot 'emissive' probe) can provide more accurate information. In this study, however, such facilities are unavailable. Therefore, since plasma density is needed with some accuracy to determine the negative ion fraction, another method of Langmuir probe analysis must be used, which ideally would not require accurate knowledge of temperature or plasma potential.

Fortunately, just such a method was developed by Mott-Smith and Langmuir, and is referred to as the Orbital Motion Limited (OML) technique [21]. In this method, the *ion* density can be calculated from the gradient of the slope fitted to the ion saturation region of a plot of I^2 against V, according to:

$$I \xrightarrow[T_i \to 0]{} A_p n_i q \frac{\sqrt{2}}{\pi} \left(\frac{|qV|}{m_i} \right)^{1/2} \tag{3.1}$$

Where I is probe current, A_p is the probe surface area, n_i is ion density, q is the elementary charge, V is the probe potential and m_i the ion mass. Squaring both sides, it becomes clear that the gradient, K, of a linear fit to I^2 against V in the ion region is given by:

$$K = A_p^2 n_i^2 q^2 \frac{2}{\pi^2} \frac{q}{m_i} \tag{3.2}$$

Rearranging for n_i, we have:

$$n_i^2 = \frac{K \pi^2 m_i}{2 A_p^2 q^3} \tag{3.3}$$

yielding ion density in terms of an easily measurable gradient and known physical quantities.

It is important to be aware, however, that this simplification relies on a number of unreasonable assumptions; primarily, that the sheath edge exists at some arbitrarily infinite distance from the probe, and that plasma ions spiral along a gently increasing potential gradient towards the probe without being disturbed from such a path by collisional events. In most real plasmas such assumptions cannot be justified, yet despite these limitations the OML technique can give surprisingly good results outside of its intended range [57]. The simplicity of the OML method gives it a number of other advantages over other methods, despite the limited applicability. The Allen-Boyd-Reynolds (ABR) theory relies on repeatedly solving differential equations to extract plasma parameters from the I-V curve, and the Bernstein-Rabinowitz-Laframboise (BRL) method requires 'clean' characteristics and computational anaylsis. The OML method requires neither complication, and instead offers a simple analytical method of calculating plasma density. Furthermore, the ABR method tends to underestimate the density, and BRL to overestimate; OML, however, performs unexpectedly well even in situations where it theoretically should not apply.

3.2 Laser Photodetachment

3.2.1 Review of Laser Photodetachment Technique

The earliest record in the literature of the term "laser photodetachment" is Hall, Robinson and Branscomb 1965 [58], where the authors are concerned with the photodetachment of I^- by a double-photon impact process. In that work, a ruby laser was used to illuminate a population of negative ions in an ammonia/iodine hot cathode arc discharge. In subsequent years the photodetachment technique was used extensively to determine the electron affinities of various atomic and molecular species by photodetachment of their negative ions, including He [59] and O_2 [60] among numerous other molecular ions [61]. The technique was used extensively thereafter to perform diagnostics on a wide range of negative ion species in various environments and contexts [62, 63], becoming firmly established as a simple, convenient and versatile experimental tool for this purpose. The use of photodetachment to measure negative ion densities in hydrogen plasmas was performed by Bacal in 1979 [64], and again to measure the thermal velocity of H^- in 1990 [65].

Studies of negative ions using laser photodetachment are extensive and considerable volumes of literature relating to this topic were produced throughout the 1980s and 1990s, using various lasers including ruby lasers, dye-lasers [66], and more recently Nd:YAG [67] laser systems. In 1991, the combination of laser detachment with the probe technique was investigated by Amemiya and Suzuki [68], and subsequently refined - to account for ablation of the probe surface by impinging laser photons - by the development of the 'eclipse' technique [24]. Langmuir probe assisted laser photodetachment is a therefore a relatively straightforward technique, developed over a number of years, to determine locally the density of negative ions in a plasma [22]. This method has been successfully used on a planar reactive magnetron system at Liverpool, sputtering over a range of different operating conditions (Ar/O_2 mixture ratios, gas pressure and powers) in DC [25] RF [11] and pulsed-DC [49, 51] modes. O^- density measurements have also been made at selected single positions and along a line on the central axis of the discharge [50].

3.2.2 Experimental Arrangement

Laser photodetachment involves the illumination of a column of plasma, defined by the beam diameter, by a short duration laser pulse [69]. By

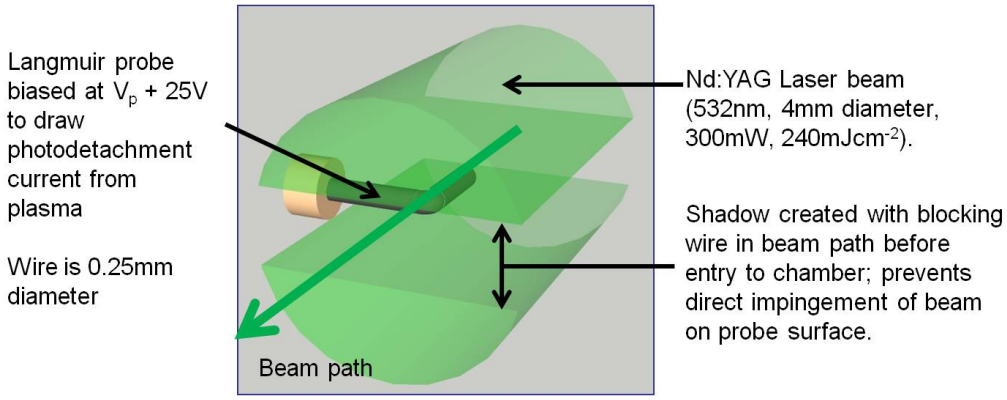

Figure 3.1: Schematic illustration of the Langmuir probe-assisted eclipse laser photodetachment technique, showing the Langmuir probe situated in the beam path. A shadow is cast in the beam path by a blocking wire positioned 'upstream' of the probe, before the beam enters the plasma.

choosing photon energies ($h\nu$) above the electron affinity of the selected negative ion, detachment will occur resulting in a new electron in the plasma that can be collected by a positively biased electrical probe positioned in the path of the beam. This is illustrated in figure 3.1. The electron affinity of O^- is 1.46 eV and so the second harmonic of a Nd:YAG laser ($\lambda = 532$ nm) with $h\nu = 2.33$ eV is chosen in our study, having a laser pulse duration is 5-6 ns at a 10 Hz repetition rate and a manufacturer-stated beam divergence < 0.5 mrad. To verify the beam divergence, the optical path length from the variable aperture to the chamber window was measured to be $l = 874\,\text{mm}\pm10\text{mm}$. The beam diameter is set to 4 mm at the variable aperture, and measured to be 4.2 mm at the window surface. This gives a divergence of ≈ 0.3 mrad over the optical path prior to entering the plasma chamber.

In addition to O^-, oxygen plasmas also contain O_2^- ions, which can suffer electron detachment at these photon energies, however these ions only constitute about 2% of the total negative ions in the plasmas [25] and we ignore their presence. In the case of H^-, the electron affinity is 0.75 eV. Here, the 2.33 eV photons are also sufficient to detach the surplus electron from the hydrogen atom, but insufficient to cause ionisation of the H atom to H^+ (13.6eV). The fraction of negative ions that suffer electron detachment in the beam Δn_- as a proportion of the original total n_- is given by

$$\frac{\Delta n_-}{n_-} = 1 - \exp\left(-\frac{E}{S}\frac{\sigma_{pd}}{h\nu}\right) \tag{3.4}$$

where E is photon energy per pulse, S is the beam cross-sectional area and σ_{pd} is the photodetachment cross section ($6.5 \times 10^{-18}\,\mathrm{cm}^2$ for O^- [70]). For sufficient energy density, $\Delta n_-/n_-$ approaches unity. Provided all the liberated electrons in the vicinity of the probe are collected by the probe we can relate the transient photodetachment current detected ΔI_{pd} to the local negative ion density n_- by

$$\frac{\Delta I_{pd}}{I_e} \approx \frac{n_-}{n_e} \tag{3.5}$$

where I_e is the electron current to the probe prior to photodetachment and n_e is the native electron density. This relation is valid provided the liberated electrons are thermalised on a timescale of the order of their transport to the probe, which is a reasonable assumption in our case [25]. To ensure the Langmuir probe sweeps up all the detached electrons in its vicinity it is biased positively into the electron saturation region of the probe characteristic.

In depositing plasmas the Langmuir probe tip (and its support stem) may become coated with conducting or insulating material. This material can be ablated, ejecting neutrals into the plasma, if a high-powered laser is incident upon it. Ablation has the effect of raising ΔI_{pd} to a value above the expected saturation current described by equation 3.4. Kajita et al. [23, 24] attributed this anomalous current detection to several possible mechanisms, including thermionic electron emission (due to laser irradiation and electron current heating if the probe is biased sufficiently above plasma potential) and direct laser ablation of the probe surface. To mitigate this, a blocking wire is placed in the path of the beam prior to entry into the plasma. This creates a shadow which prevents laser photons from directly impinging on the probe surface, thus removing the ablation signal from the measurement and allowing the correct value of ΔI_{pd} to be determined; the method is consequently known as "eclipse laser photodetachment". A small fraction of the collection volume adjacent to the probe is also shadowed by this blocking wire, and therefore photodetachment cannot occur in this region. In order to minimise this shadowed volume adjacent to the probe, the blocking wire thickness is made as close as possible to the thickness of the probe wire. While it is impossible to remove this shadowed volume completely, it can be assumed that its magnitude is small compared to the total collection volume, and it subsequently contributes only a small uncertainty to the final measured value of n_-. A photograph of the optical arrangement used for this study is shown in figure 3.2.

The photodetachment technique as described here was extensively optimised

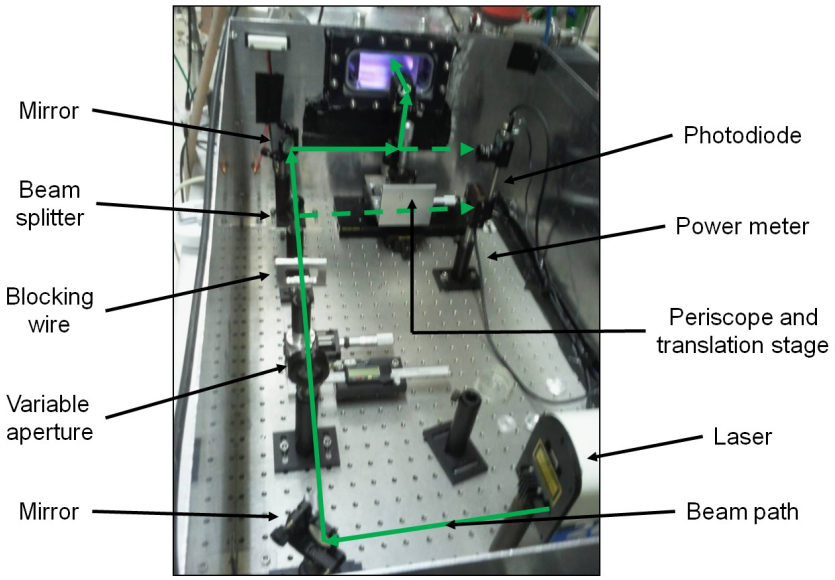

Figure 3.2: A photograph of the optical arrangement, showing various components for beam manipulation and monitoring.

for operation in this particular magnetron experiment by Dodd *et al.* [25]. Photodetachment signals were recorded over a range of laser energy densities with various blocking wires, in order to verify experimentally the theoretical curve described by equation 3.4. It was found that good agreement with this theoretical curve was obtained in all cases for laser energy densities in the linear regime (see figure 3.3), however in the "saturation" regime, considerable contributions from the ablation effect were observed in the case of no blocking wire. In order to efficiently remove any ablation signal from the photodetachment measurement, the blocking wire used to eclipse the probe was placed 'upstream' from the probe in the path of the beam. The effect of this is also shown in figure 3.3. The optimal wire diameter was found to be slightly larger than the probe diameter, with the best fit to the theoretical curve being observed with a $380\,\mu$m blocking wire. With this condition satisfied, any diffraction of the laser photons around the blocking wire would leak into the eclipsed area, as advised in [24].

In order for the photodetachment technique to be valid, it is necessary for the electrons detached by the laser photons to thermalise with the background plasma electrons before they are captured by the probe. Dodd determined that the Maxwellisation time (that is, the time taken for the detached electrons to reach thermal equilibrium with the background plasma) [22], τ_m, of the detached electrons is $\sim 10^{-6}\,$s, which suggests that these electrons are at least

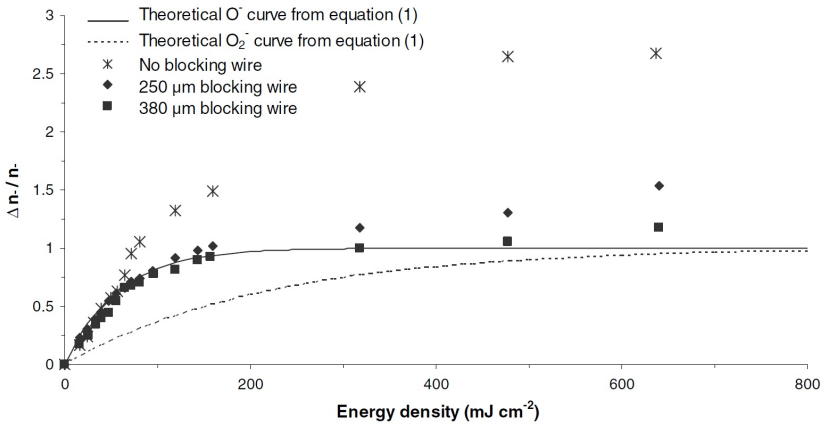

Figure 3.3: A plot of the photodetachment fraction ($\Delta n_-/n_-$ with n the negative ion density) as a function of laser beam energy density (at 532 nm), for a number of different BW diameters. Image from [25]

partially thermalised when they are collected. It is therefore reasonable to make the assumption that the photodetached electrons are thermalised, thus validating the method in this case.

By varying the bias voltage on the probe for a range of laser beam diameters, it is possible to determine the optimal beam diameter and bias voltage in a given plasma. In the case of the magnetron, it was found that increasing the bias voltage increases the measured photodetachment current. This increase in measured current continues with increasing bias, despite the fact that the photodetachment current should saturate when all the negative ions in the beam path are detached. This continual increase in ΔI_{pd} with bias voltage is due to the expanding collection radius of the probe with increasing bias. As the bias voltage increases, the electric field of the collection radius (which at high voltages can exceed the beam width) may be accelerating negative ions from outside the beam into the beam path, thus increasing the photodetachment signal.

Since the parameter of interest is $\Delta I_{pd}/I_e$ to determine the electronegativity, α, this was also plotted against probe bias by Dodd (figure 3.4, see also 4.2). Here it can be seen that at higher probe biases, the current ratio reaches a maximum close to a threshold voltage, and then begins to decrease slightly as the bias is increased beyond this threshold. This threshold voltage can be estimated as a function of beam radius and probe radius, and indicates the bias at which the collection region of the probe exceeds the beam diameter. For sufficiently large beam diameters, the photodetached current is independent

of beam radius for biases below this threshold. Furthermore, as the trends plotted in figure 3.4 show, the condition that the collection region must be inside the beam can be relaxed for large beam radii; evidenced by the close agreement of $\Delta I_{pd}/I_e$ with bias for increasing beam size above 3mm diameter.

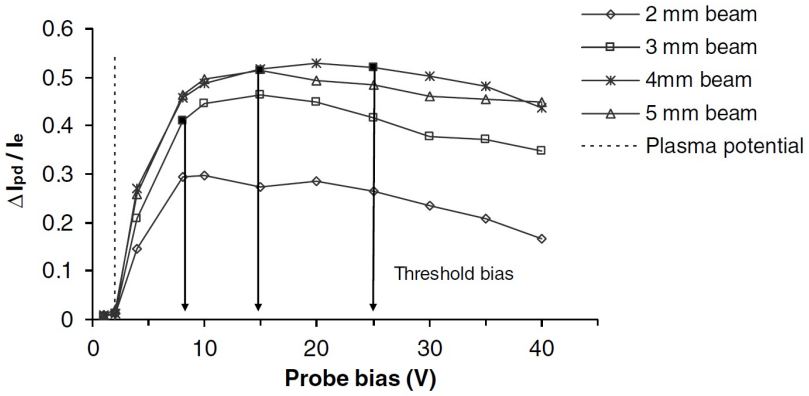

Figure 3.4: A plot of the ratio of the photodetached electron current to the electron current ($\Delta I_{pd}/I_e$) against probe bias (relative to ground potential) for a number of different laser beam diameters. Image from [25].

With this information it is possible to identify optimal beam and bias conditions for photodetachment in the magnetron, to allow for confident measurement of $\Delta I_{pd}/I_e$, and therefore α and subsequently n_-. In [25] this is determined to be a 4 mm beam size for biases slightly above the threshold, typically with $V_{bias} \sim V_p + 30V$.

Collection and interpretation of the photodetachment current signals is somewhat simpler than that of the Langmuir probe characteristic, and considerably less involved. Once the Langmuir probe characteristic has been obtained, and the plasma potential V_p estimated using the derivative method, the probe can be switched to a static dc bias such that the probe potential is held positive with respect to the local plasma potential.

This is achieved with an extraction circuit which serves to draw the photodetachment current from the plasma so that it can be captured with an oscilloscope. The circuit used in this case was developed and analysed by Bryant [71] (illustrated in figure 3.5) and gives the truest recording of the temporal current profile that can reasonably be obtained. A bias voltage is applied with a DC power supply directly to the probe. A large capacitor ($C_{bp} = 1000\,\mu$F) serves to 'shunt' the transient photodetachment signal over the power supply to ground, such that it does not pick up any distortion from the internal circuitry of the power supply. The photodetachment signal

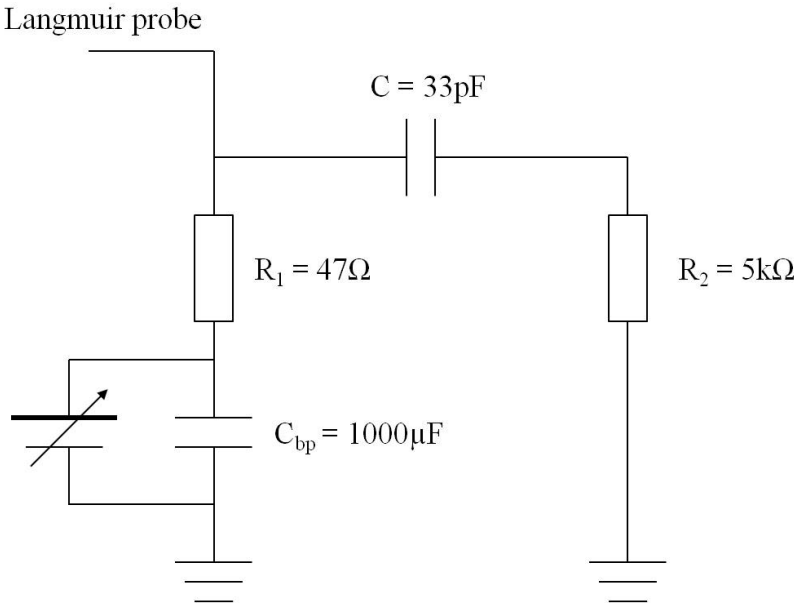

Figure 3.5: Circuit diagram of photodetachment current extraction circuit.

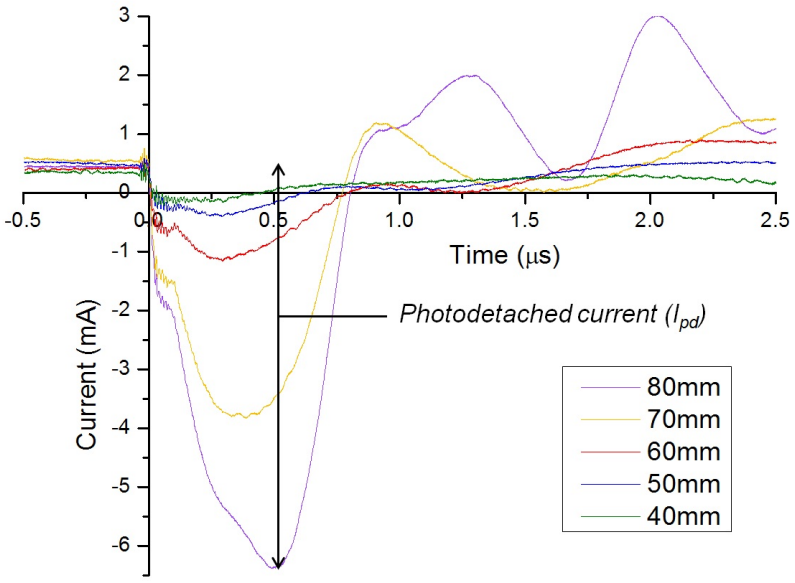

Figure 3.6: Photodetachment current temporal profiles for a range of positions along the plasma centreline. Currents were calculated from potentials measured across a 51 Ω resistor.

is measured with a voltmeter across $R1 = 51\,\Omega$. The capacitor $C = 33\,\text{pF}$ filters the dc background current from the measured signal, and the resistor $R2 = 5\,\text{k}\Omega$ serves to reduce the input impedance of the voltage probe such that the measured photodetachment signal is not artificially suppressed (as observed by Bryant).

Figure 3.6 shows example photodetachment current signals at different positions along the centreline of the discharge, with the laser being fired at $t = 0\,\text{s}$. The oscilloscope is triggered using the laser pulse as detected using a photodiode (see figure 3.8). The photodetachment signal is recorded on the oscilloscope using a voltage probe, and the current due to photodetachment as shown in figure 3.6 (also called the 'opto-galvanic' signal) is obtained trivially from Ohm's law, as $\Delta I_{pd} = \Delta V_{pd}/R1$ where ΔV_{pd} is the initially captured voltage signal. With the photodetachment current so obtained, and using the native current I_e as read from the Langmuir probe characteristic (it is simply the measured current at the bias potential), the negative ion density can be calculated according to equation 3.7.

3.3 Magnetron and Photodetachment Systems

3.3.1 The Magnetron Apparatus

The experimental system used in this study is photographed in figure 3.1, and is identical to that described in [25]. A schematic diagram is shown in figure 3.8. It consists of a VTech 150 series unbalanced magnetron (Gencoa Ltd, UK) mounted vertically above a grounded electrode in a 10 litre aluminium vacuum chamber. The 150 mm diameter circular titanium target (purity >99.95%) is surrounded by a ground shield. Regulated dc power is supplied by a Pinnacle Plus power supply (Advanced Energy Inc.) and a base pressure of $1 \times 10^{-4}\,\text{Pa}$ ($1 \times 10^{-6}\,\text{mbar}$) is achieved using a turbomolecular pump backed by a rotary pump. Oxygen and argon gases of pure research grade (>99.99% purity) are fed into the vacuum chamber via two 20 sccm (MKS Instruments Ltd) mass-flow controllers and the chamber pressure is regulated using a Baratron gauge in conjunction with the controllers. This set-up allows control and regulation of partial and total pressures up to a maximum of 3.3 Pa (25 mTorr).

In order to ensure efficient photodetachment of electrons from the O^- and H^-

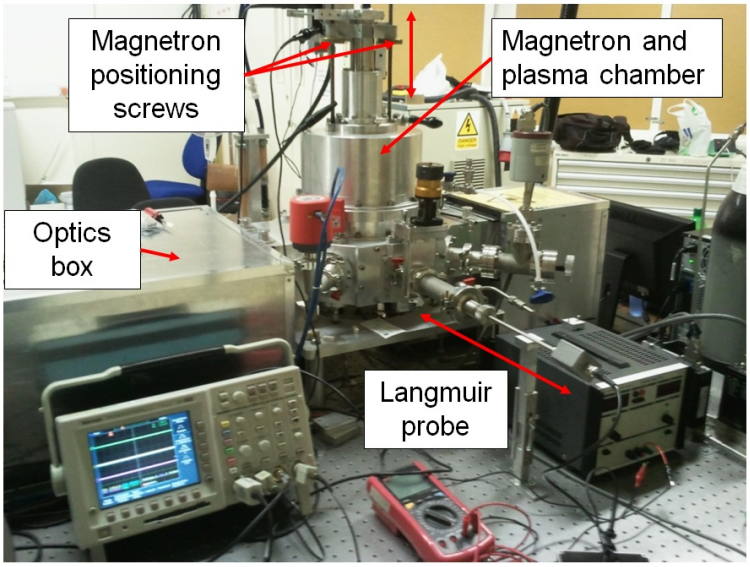

Figure 3.7: A photograph of the experimental system, showing the magnetron chamber and Langmuir probe.

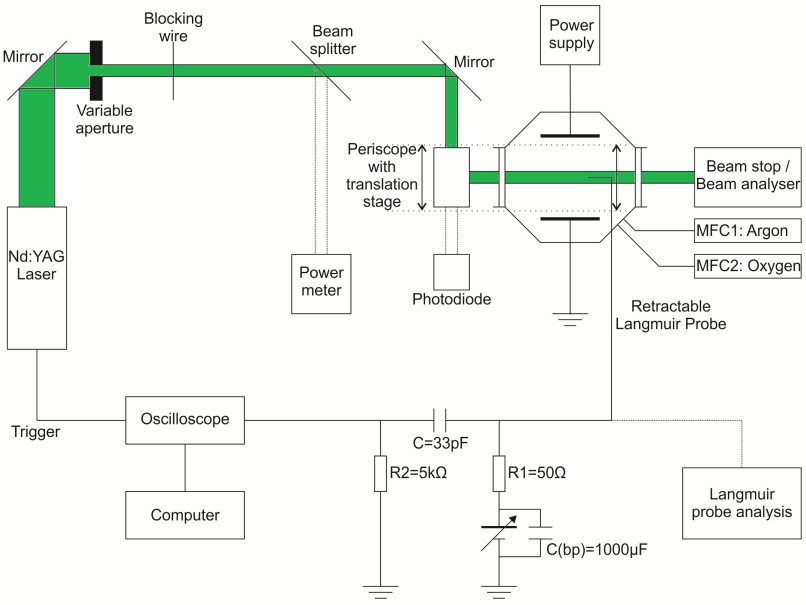

Figure 3.8: Schematic diagram of the experimental setup for O_2/Ar dc discharges. For hydrogen experiments, H_2 is substituted for O_2 via MFC2.

ions, a pulsed Q-switched Nd:YAG laser (Quantel Brilliant B), frequency-doubled to 532 nm is used. The laser beam intensity is attenuated to provide a pulse energy of 30 mJ per pulse, with energy density of

246 mJ cm^{-2}±5%, previously shown to be optimum for this arrangement [25], ensuring the condition $\Delta n_-/n_- \approx 1$. Aligned co-axially with the laser beam is a 250 μm diameter 'L'-shaped cylindrical probe of 10 mm total length (a 7 mm long extension parallel to the beam axis and a 3 mm short extension). The probe is shadowed with a 300 μm diameter blocking wire, and biased 25 V±10% positive with respect to the plasma potential, V_p (typically -10 V to +3 V in the regions of interest). The plasma potential is estimated at each probe position from the zero crossing point of the second derivative of the electron current I_e versus retarding potential, V (namely $d^2I_e/dV^2 = 0$). To determine the plasma parameters, probe characteristics are obtained using a commercial probe acquisition system (ESPIon from Hiden Analytical Ltd). In order to ensure repeatability in the probe data, a chamber clean with pure argon plasma is performed regularly and a current-voltage characteristic recorded. During probe data acquisition the probe is held at a -80 V parking potential between measurements in order to minimise the effects of deposition on the probe.

3.3.2 Spatial Resolution and Measurements

Spatially-resolved laser photodetached measurements in the system are made by moving independently the Langmuir probe, the magnetron and the line-of-sight of laser beam. The latter is done using Vernier screw gauges to reposition the mirror optics prior to beam entrance through the window. Doing this allows measurements to be made in a plane defined by -30 mm≤r≤30 mm and 30 mm≤z≤100 mm where r is the radial distance between the probe centre and the discharge centreline, and z is the axial distance of the probe from the target. This area is limited by the window dimensions and magnetron travel. A photograph of a typical argon discharge as seen through the laser beam entry window is shown in figure 3.9, illustrating the positioning of the Langmuir probe and the method of scanning the mid-plane of the discharge. Measurements can be made every 5 mm in the r-direction, and (if necessary) up to every 0.01 mm in the z direction. For practical purposes, a spatial resolution of 5 mm was used in both r and z. The spatial resolution in r is defined by the probe length (10 mm) and in z by probe sheath width (<1 mm). Due to the precision of calibration of the $r = 0$ mm, $z = 0$ mm position, there is an estimated uncertainty in all positions of ±1 mm in r and z.

The photodetachment signal ΔI_{pd} and native electron current I_e are measured directly from the digital oscilloscope (300 MHz bandwidth), and averaged 512

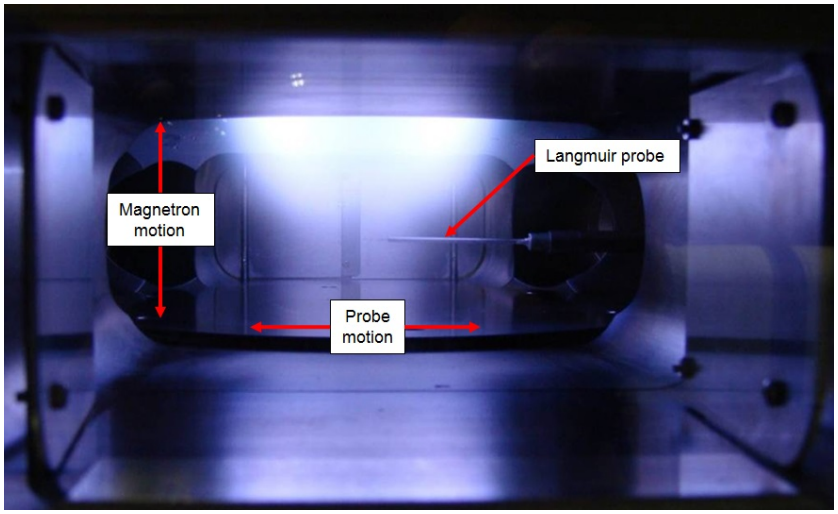

Figure 3.9: A photograph of a typical argon discharge viewed through the laser beam entry window, showing the method of scanning the discharge midplane. The Langmuir probe is also visible.

times to enhance the signal-to-noise ratio. From the ratio of these quantities the degree of electronegativity $\alpha = \Delta I_{pd}/I_e$ is readily determined. A Langmuir probe characteristic is also recorded for each probe position and analysed using the orbital motion limited (OML) approach [21] (see section 4.1.1), to determine the ion density, n_i, independently of the electron temperature T_e. Although it has been shown that in highly electronegative plasmas (typically for $\alpha > 2$) the Bohm criterion which regulates the ion flux is modified [44, 72], in our case (as will be shown later) α is in general lower than this value. Therefore, our probe analysis is performed assuming no effect from negative ions.

In the oxygen analysis it is assumed that Ar^+ and O^+ ions were present in equal qualities. This ratio was observed approximately in data collected using mass spectrometry (not presented here), and is also observed in HiPIMS [29] and RF [73] discharges. The average mass of $m_i = 28$ amu is therefore used to determine ion density n_i. In the case of hydrogen, no other gases are present in the discharge so the ion mass m_i is assumed to be 1 amu. The electron density n_e is not sought using the probe technique since its value is somewhat unreliable for high magnetic field regions of the discharge [74]. The positive ions are assumed to be un-magnetised and their collection to the probe is unaffected by the magnetic field.

From the assumption of quasi-neutrality $n_e + n_- = n_i$, equation 3.5 can be

rewritten as

$$\frac{\Delta I_{pd}}{I_e} \approx \alpha = \frac{n_-}{n_i - n_-} \tag{3.6}$$

so providing an estimate of the negative ion density n_- from the independently measured α and n_i values, namely:

$$n_- = \left(\frac{\alpha}{1+\alpha}\right) n_i \tag{3.7}$$

3.3.3 Pulsing and Time-resolution

In the case of pulsed-dc, the setup is the same as that shown in figure 3.8 with the addition of a home-made signal 'chopper' to convert the high-power dc input into a pulsed waveform with variable pulse width and duty cycle (see figure 3.10). This allows delivery of unipolar mid-frequency pulsed power to the cathode. In order to successfully time-resolve the measurements in a pulsed plasma, the laser must be triggered externally by a TTL input signal such that it is synchronised with the desired timestep when operating in pulsed mode. A Stanford delay generator was therefore used to generate the trigger pulses necessary for temporal synchronisation of the laser pulse and discharge pulse, in order to record photodetachment signals at the appropriate timesteps. A similar synchronisation was also required to trigger the ESPIon system to record the time resolved current-voltage characteristic.

Synchronising the laser was achieved by external triggering of the flashlamp. By using the input voltage to the cathode as an input trigger, it was possible to generate a trigger signal synchronised with the start of the discharge pulse. A consequence of using this method is that, although the flashlamp is controlled externally, the laser pulse itself occurs some time after the flashlamp is triggered. This was observed to be $\sim 185\,\mu$s$\pm 2\mu$s. Therefore, although the TTL signal triggered by the discharge potential occurs at $t = 0\,\mu$s$\pm 0.2\,\mu$s, the laser pulse is not synchronised with $t = 0$. As such, it is necessary to introduce a delay on the TTL pulse, in order to synchronise the laser pulse with the beginning of the subsequent discharge pulse. This is illustrated in figures 3.11a and 3.11b. This setup allows a time resolution of $t = (t_0 + \delta t) \pm 2\,\mu$s, where t_0 is the beginning of the pulse and δt is the desired time-step.

In order to ensure that the laser repetition rate of 10 Hz is maintained, a delay from the beginning of the TTL pulse is introduced, in order to ensure

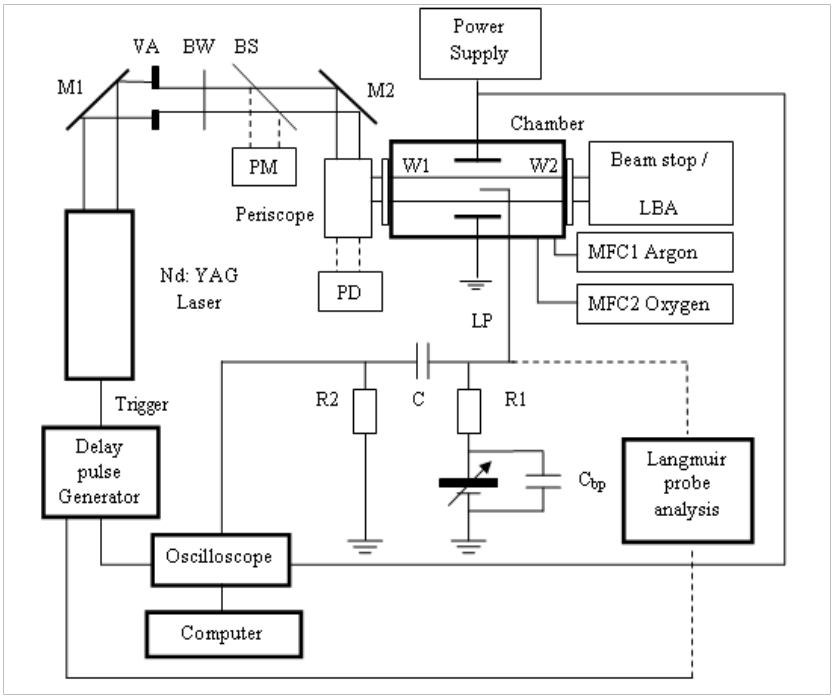

Figure 3.10: Schematic diagram of the experimental setup for O_2/Ar pulsed-dc discharges. For hydrogen experiments, H_2 is substituted for O_2 via MFC2.

that trigger signals are only sent to the laser every 0.1 s. This means that the laser is not triggered by each discharge pulse (operating at 5kHz).

3.4 Summary

The experimental systems used in this study have been described, and the principles underlying the Langmuir probe and photodetachment diagnostics outlined. A Gencoa Ltd, UK VTech 150 series unbalanced magnetron was used to discharge oxygen/argon and hydrogen gas atmospheres. A 1 cm 'L'-shaped cylindrical Langmuir probe, situated in the path of a 532 nm Nd:YAG laser beam with an energy density of 240 mJ cm^{-2} was used to collect current-voltage characteristics and photodetachment current signals. By moving the magnetron and probe/laser arrangement relative to one-another, it was possible to map spatially the plasma quantities obtained using these diagnostics (ion density, negative ion density, temperature, and electronegativity, as well as estimates of plasma potential). With use of a Stanford delay generator to manually trigger the laser pulse, it was possible

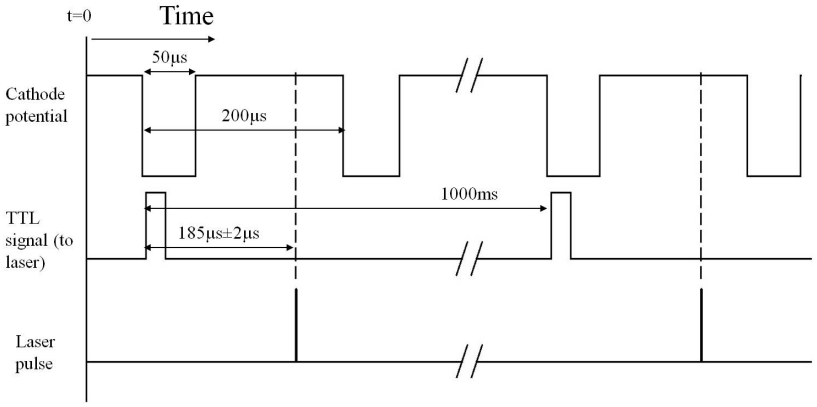

(a) Unsynchronised timing diagram.

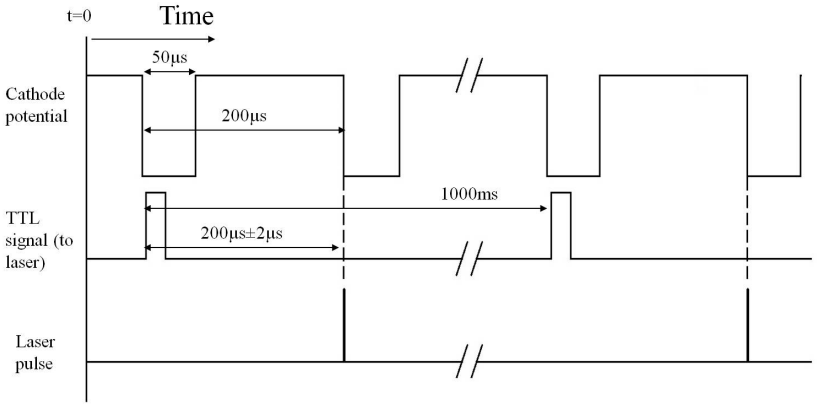

(b) Synchronised timing diagram.

Figure 3.11: Timing diagrams showing the a.) unsynchronised and b.) synchronised discharge waveform, TTL pulse and laser pulse

to resolve temporally the same information.

Chapter 4

Calibration and Plasma Characterisation

4.1 Basic Plasma Characterisation

Several preliminary studies were performed to verify the findings of Dodd, You *et al*, and to provide basic calibration information for the instruments. The optimal parameters for laser energy density, probe bias, O_2 partial pressure and discharge power, as indicated by Dodd's results summarised in section 2.3 are:

- Energy density $E/S = 240\,\mathrm{mJ\,cm^{-2}}$, requiring a laser power of $\sim$ 300 mW for a 4 mm-diameter beam firing at 10 Hz (2 mm radius, as in [25]).
- Probe bias $V_b \approx 30\,\mathrm{V}$ with respect to the local plasma potential
- O_2 partial pressure $\sim$ 10-30 % of the working gas admixture.
- Discharge power $P = 200\,\mathrm{W}$

The effect of laser energy density on negative ion fraction $\Delta n/n_-$ is shown in figure 4.1. Values were measured for a 4 mm-diameter beam operating at 532 nm, with a 300 μm blocking wire, in order to verify equation 3.4 is valid for the magnetron discharges. Consistent with the observations of Dodd, the photodetached fraction follows the theoretical curve closely in the linear region at low energy densities, and is overestimated above the saturation threshold at $E/S \approx 240\,\mathrm{mJ\ cm^{-2}}$. In order for 3.5 to apply, all negative ions within the beam volume must be detached. Laser energy densities are

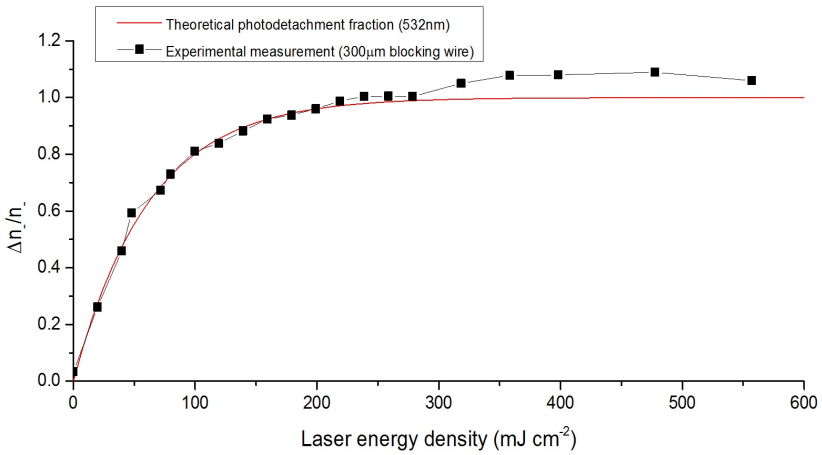

Figure 4.1: A plot of the negative ion fraction ($\Delta n/n_-$) as a function of laser energy density, for a 532 nm beam and a 300 μm-diameter blocking wire. Oxygen content was set to 20%, discharge power to 200 W and total pressure 10 mTorr.

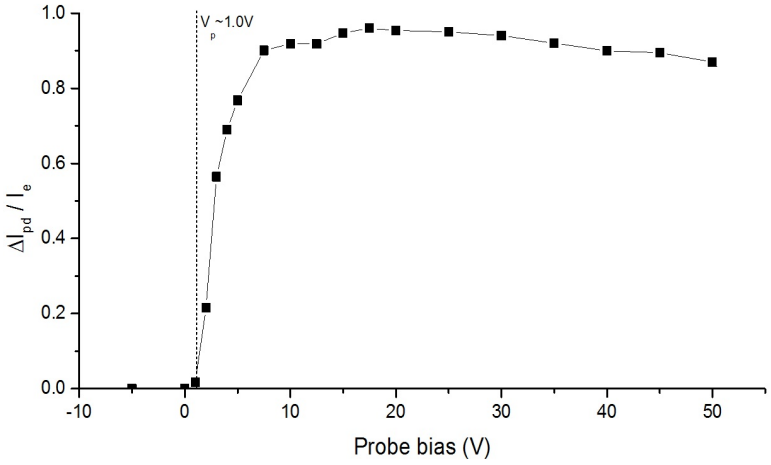

Figure 4.2: A plot of the photodetached current fraction ($\Delta I_{pd}/I_e$) as a function of probe bias, for a 300 mW 4 mm-diameter beam, 300 μm-diameter blocking wire. Oxygen content was set to 20%, discharge power to 200 W and total pressure 10 mTorr.

therefore chosen to be as close as possible to the saturation threshold. Using a laser energy density of 240 mJ cm^{-2}, a beam diameter of 4 mm and a pulse repetition rate of 10 Hz, this gives a beam power of $\approx$ 301 mW. Given an estimated uncertainty in measured beam power of $\pm$5% due to instrument

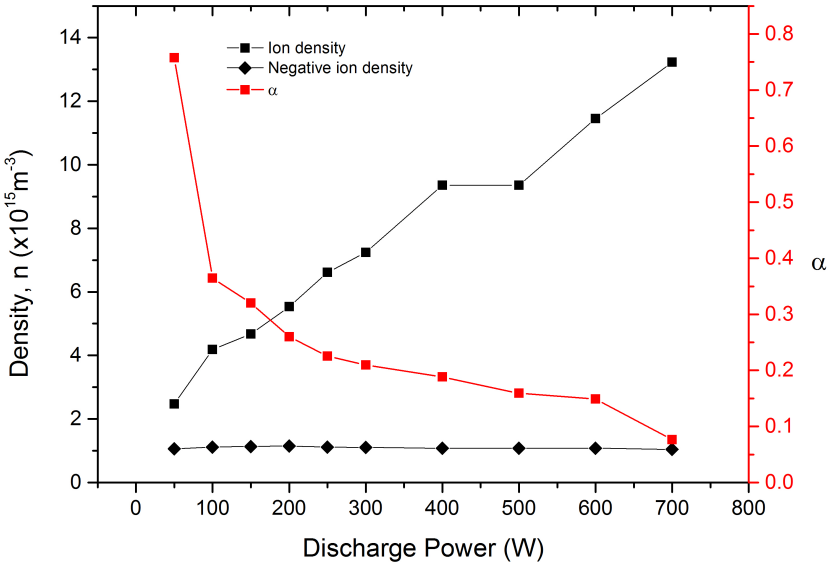

Figure 4.3: A plot of the negative ion density (n), electron density (n_e) and $\alpha(= n/n_e)$ against magnetron power for a 20% O_2 10mTorr discharge, measured with a 300mW beam and probe bias of +25V with respect to the plasma potential.

calibration laser power was set to 300 mW, a value used in all subsequent oxygen experiments and consistent with that used by Dodd.

The photoelectron current ratio $\Delta I_{pd}/I_e$ was plotted as a function of probe bias for a 4 mm beam, shown in figure 4.2. In comparison with figure 3.4, the decline in $\Delta I_{pd}/I_e$ (assumed to be α) at higher bias voltages is less pronounced; however the same trend is observed with peak values being measured at $V_b \approx 17$ V, slightly lower than in [25]. In order to avoid underestimation of α by setting the bias voltage too high, experiments were performed with a probe bias of +25 V with respect to plasma potential V_p.

Figure 4.3 shows ion density, negative ion density and α against discharge power for a 20% O_2 discharge at 10 mTorr, with n_- plotted on separate axes in figure 4.4. Figure 4.5 shows the same quantities against O_2 partial pressure for a 10 mTorr 200 W discharge. The trends shown reproduce faithfully those observed by Dodd, although absolute values vary somewhat. The difference in absolute values can be attributed to the variability of plasma potential and discharge current in poisoned mode which arises as a result of insulating sputtered coatings on the chamber walls, meaning that different values are observed in different experiments, for nominally the same plasma conditions. This effect can be mitigated somewhat by conditioning the chamber (by

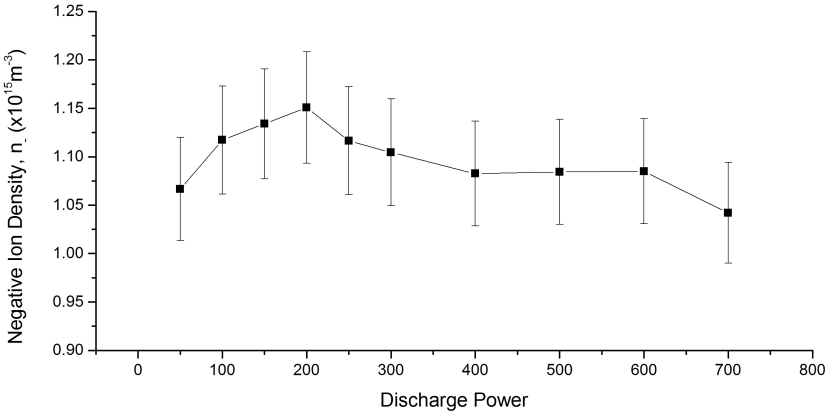

Figure 4.4: A plot of the negative ion density against magnetron power for a 20% O_2 10mTorr discharge, measured with a 300mW beam and probe bias of +25V with respect to the plasma potential.

sputtering in pure argon between experiments) until discharge current and voltage are stable (in a 200 W 10 mTorr pure argon metallic discharge, cathode voltage stabilises at 269 V$\pm$1 V and current at 0.75 A$\pm$0.01 A - this provides a convenient "benchmark" for conditioning the chamber), however it is difficult in practice to generate identical chamber conditions from experiment to experiment when operating in poisoned mode.

Although the negative ion density appears to vary very little compared to ion density and α over the range of discharge powers, when plotted on a separate axis (see figure 4.3 inset) a small peak is visible at a power of 200W, broadly similar to that observed by Dodd (figure 2.3). Note that Dodd calculates n_e, rather than n_i as in this case. Similarly, the negative ion density was observed to peak at 20% O_2, again consistent with Dodd's measurement.

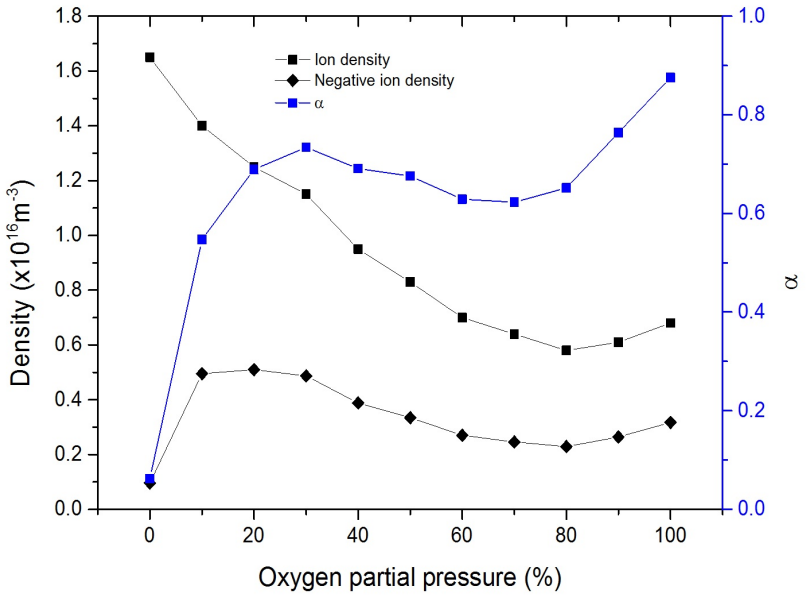

Figure 4.5: A plot of the negative ion density (n), electron density (n_e) and $\alpha(= n/n_e)$ against O_2 partial pressure for a 200 W 10 mTorr discharge, measured with a 300 mW beam and probe bias of +25 V with respect to the plasma potential.

4.1.1 Validation of OML Approach

In the case of this study, simple estimations of the Child sheath and ion mean free path were calculated in order to determine whether the sheath can be considered collisionless, thereby validating to some extent the choice of OML as the probe analysis method. The Child Law sheath for an unbiased probe is given by:

$$s = \frac{\sqrt{2}}{3}\lambda_D \left(\frac{2V_p}{T_e}\right)^{3/4} \tag{4.1}$$

where the Debye length

$$\lambda_D = \sqrt{\frac{\epsilon_0 k_B T_e}{q^2 n_e}} \tag{4.2}$$

Using typical plasma densities $n_e \sim 10^{16}\,\mathrm{m}^{-3}$, temperatures $T_e \sim 2\,\mathrm{eV}$, plasma potentials $V_p \sim 1.0\,\mathrm{V}$, and taking the temperature in Kelvin as

$$T(K) \approx 11,600\,T(eV) \tag{4.3}$$

we have

$$\lambda_D \sim 1 \times 10^{-4}\,\mathrm{m} \tag{4.4}$$

and the Child sheath radius

$$s \sim 4 \times 10^{-5}\,\mathrm{m}. \tag{4.5}$$

Extending the Child sheath estimate to typical bias voltages of some few tens of volts where V_p in equation 4.1 is replaced with the sum of the bias voltage and plasma potential, say $\Phi = V_p + V_b \sim 30\,\mathrm{V}$, we have

$$s \sim 4 \times 10^{-4}\,\mathrm{m}. \tag{4.6}$$

For an ion passing through a neutral gas, the mean free path

$$\lambda_i = (n_g \sigma)^{-1} \tag{4.7}$$

where n_g is the neutral gas density (from the ideal gas law, typically $\sim 10^{19}\,\mathrm{m}^{-3}$/mTorr in the magnetron case) and σ is the hard-sphere cross section given by

$$\sigma = \pi(r_1 + r_2)^2 \tag{4.8}$$

For a 10 mTorr plasma

$$n_g \approx 10^{20}\,\mathrm{m}^{-3} \tag{4.9}$$

Taking the atomic radius for argon to be the Van der Waals radius ($r_1 = 188 \times 10^{-12}\,\mathrm{m}$) and the Ar^+ ion radius to be the Pauling ionic radius ($r_2 = 154 \times 10^{-12}\,\mathrm{m}$) we have

$$\sigma \sim 4 \times 10^{-19}\,\mathrm{m}^2 \tag{4.10}$$

and hence the mean free path

$$\lambda_i \sim 3 \times 10^{-2}\,\mathrm{m} \tag{4.11}$$

It should be noted that since there are ions present in the plasma, a thorough treatment of this problem would require more involved calculations of scattering cross-sections based on Coulomb potential functions. Fortunately, since the ion densities are typically ~ 1000 times smaller than the neutral gas density, the probability of a collision between two ions is significantly smaller than between an ion and a neutral, and the ion contribution to the mean free path can be somewhat neglected. In general, however, the presence of ions within the plasma would serve to shorten λ_i to some degree. Even so, given the difference in ion and neutral densities, it is reasonable to expect that an ion can travel several millimetres or perhaps even centimetres before experiencing a collision event within the discharge. Since the mean free path, then, is much greater than the sheath thickness of $\sim 10^{-4}$ - 10^{-5} m, the assumption of a collisionless sheath is valid.

4.2 Beam Calibration

For the purposes of the laser energy density calculations and measurements described in 4.1, it was assumed that the laser beam profile is flat with energy density assumed to be constant across the beam. In order to verify this, measurements of the beam power and energy density were performed for various beam diameters. The beam is 9 mm in diameter at the output from the laser, however this can be reduced by employing apertures of various diameters to partially block the outer portion of the beam. Data sampling techniques were employed to obtain the average beam power over a period of 120 s at a sample rate of 10 Hz. For this analysis, the beam attenuation module was set to minimum attenuation (transmitting approximately 70% of the theoretical maximum laser output). The beam was directed onto an optical power detector (Gentec-eo) by a 99% reflectivity dielectric mirror.

Beam diameter (cm)	**Average power (W)**	**Energy per pulse (mJ)**	**Beam area (cm^2)**	**Energy density (mJ cm^{-2})**
0.90	3.00	300	0.64	470
0.60	2.37	237	0.28	840
0.50	1.81	181	0.20	920
0.40	1.23	123	0.13	980
0.30	0.67	67	0.07	950
0.20	0.25	25	0.03	800

Table 4.1: Behaviour of energy density with beam diameter.

Table 4.1 shows how the average beam power behaves as a function of beam diameter. Note that the energy density column is the average density across the beam profile. If a flat beam profile is assumed, where the average power is predicted to be proportional to the beam area and energy density remains constant, the energy density would not change with beam diameter. This would give an energy density equivalent to that of the full 9 mm beam at all diameters. Clearly this is not the case. It is more reasonable to assume (and compare with) a theoretical Gaussian energy distribution (with a somewhat arbitrary standard deviation of $\sigma = 2.1$). In this case, the beam energy density increases with smaller diameter, as the aperture blocks the low intensity 'wings' of the energy distribution profile. Table 4.2 shows the average powers as calculated from the theoretical flat and Gaussian beam profiles, and is plotted graphically in figure 4.6.

	Average power (W)		
Beam diameter (cm)	**Flat**	**Gaussian**	**Measured**
0.90	3.00	3.00	3.00
0.60	1.33	2.15	2.37
0.50	0.93	1.76	1.81
0.40	0.59	1.30	1.23
0.30	0.33	0.83	0.67
0.20	0.15	0.40	0.25

Table 4.2: Average beam power calculated as a function of beam area from assumed flat and Gaussian beam profiles. The measured values are also shown.

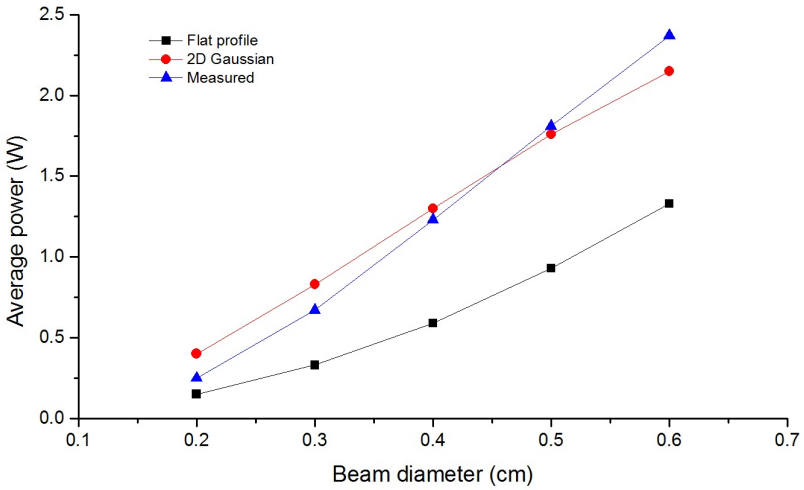

Figure 4.6: A plot of the average beam power calculated as a function of beam area from assumed flat and 2D Gaussian beam profiles. The measured values are also shown. Measured values match closely with the Gaussian profile.

The beam power most closely matches with the Gaussian profile at a diameter of 4-5 mm, which corresponds well with Dodd's selection of a 4 mm beam by other methods (see section 3.2).

Calibration of the laser power meter was necessary in order to properly monitor and control the beam energy density. Of significance is the power measured at the normal position of the power meter (see figure 3.8) and at the probe position. The beam power is attenuated from the full laser output

at each component in the beamline, and (by engineering design) only a small fraction of the full beam power is directed to the power meter. Similarly the amount the beam power deposited into the plasma at the probe position is attenuated slightly by small power losses at the mirrors and windows. Because of this, the laser power as measured at the 'PM' position (figure 3.11a) is not equal to the laser power at the probe position. As such it is necessary to determine a "conversion factor" for the power meter, in order to properly set the beam power. This was done by measuring the beam power at various positions in the beam path for three broad power levels: high, medium and low. The results of this are shown in table 4.3.

Measured power (mW)			
Full beam	**'PM' position**	**Probe position**	**Conversion factor**
195	10	50	5.0
880	40	170	4.3
1330	57	236	4.1

Table 4.3: Power as measured with the power meter at the normal position, beam output and probe position. A "conversion factor" to relate the power measured at the meter position to the power deposited at the probe is also calculated.

The average conversion factor of 4.5 was used to correct the power meter to allow the requisite energy density to be properly set. This allows the laser power to be controlled to a precision of $\pm 10\,\mathrm{mW}$ (an uncertainty slightly larger than the nominal 'jitter' at the beam output - $\pm 2\%$ - due to the calculated $4.5\times$ increase in measured values), sufficient to ensure the beam does not exceed the photodetachment saturation threshold while maintaining the assumption of $\Delta n_-/n_- \approx 1$.

Chapter 5

Time-Averaged 2D Spatial Distributions in O_2/Ar DC Plasmas

5.1 Experimental method

Despite the research successes outlined in chapter 2, there has been little or no work carried out to determine the 2-D density distribution of negative ions in the plasma bulk of the magnetron, including regions close to the substrate position. However, the angular distribution of energetic beam-like O^- ions has been measured and modelled for planar and rotatable magnetron discharges operating in argon-oxygen mixtures [38, 39] and the spatial distribution of low temperature O^- densities has been predicted from PIC-MCC modelling by Bultinck et al. [75]. The simulations in [75] were done for a 7 cm diameter circular magnetron and show peak O^- densities of $8\times10^{14}\,m^{-3}$ and $6\times10^{14}\,m^{-3}$ at 0.12 Pa and 0.24 Pa respectively, with the highest concentrations of O^- ions predicted in regions downstream of the cathode, outside the magnetic trap and away from the centre line. By varying the pressure it was found that the O^- density decreased with increasing O_2 partial pressure contradicting the experimental results of [25] and [55].

In this study the 2-D spatial distribution of O^- densities have been measured in the bulk plasma of a DC reactive magnetron discharge using the eclipse laser photodetachment method. The technique does not discriminate between negative ions based on their energy, therefore providing the total O^- density. Spatial measurements were made for three different total system pressures,

P_{tot} = 0.79, 1.59 and 2.40 Pa, keeping the O_2/Ar ratio constant at 20%. This corresponded to the three O_2 partial pressures of P_{O_2} = 0.16, 0.31 and 0.48 Pa respectively with the magnetron operating in fully poisoned mode. At the partial pressures used in this study, and with this particular system geometry, the plasmas showed long term stability in as much as there was little long term drift in target potential and current or in local plasma parameters. The applied power was kept constant at 200 W for all cases.

In previous studies the fraction of energetic O^- ions emanating from the target was estimated to be 10% of the total in the discharge [49].

5.2 Results and discussion

Figure 5.1a shows a 2-D map of the measured photodetachment current ΔI_{pd} for a total pressure of 1.59 Pa, together with the magnetic field vectors for a large area region of the plasma. The region of the magnetic trap is also identified. A radial profile for the $z = 75$ mm axial distance is plotted in figure 5.1b. The highest concentrations of ΔI_{pd} appear at distances far from the cathode, outside the last 'closed' field line, indicating the negative ions are concentrated in a toroidal ring around the central axis. The spatial distribution of native electron current I_e, positive ion density n_i, electronegativity α, and negative ion density n_- for this case are shown in figures 5.2, 5.3, 5.4 and 5.5 respectively, with α assumed to be the current ratio $\Delta I_{pd}/I_e$. The positive ion density shows high values in regions of the trap (that are accessible by the probe) and also along the discharge centre line incorporating the magnetic null, a distribution of plasma density similar to that seen elsewhere [76]. The spatial distribution of electronegativity α (fig 5.4) follows the general form of ΔI_{pd} as expected from its definition $\alpha = \Delta I_{pd}/I_e$ given I_e does not have too much spatial variation. High values of α up to 1.6 are seen to be concentrated in the upper corners of the measured region, off the centreline and above the closed field region of the magnetic trap. These are regions of relatively low positive ion density.

It is interesting to find regions where O^- densities easily exceed the electron density. On the centre line α has typical values of 0.2 - 0.4 consistent with those measured at those positions by Dodd et al. [25, 51]. The negative ion densities n_- calculated from equation 3.7 are shown in figure 5.5. The highest values appear in a narrow 3 cm wide annulus centred around the discharge centreline about 20 mm above the last closed field line at the top of the magnetic trap. The peak values $n_- \sim 9 \times 10^{15}\,\mathrm{m}^{-3}$ appear at $r = 10$,

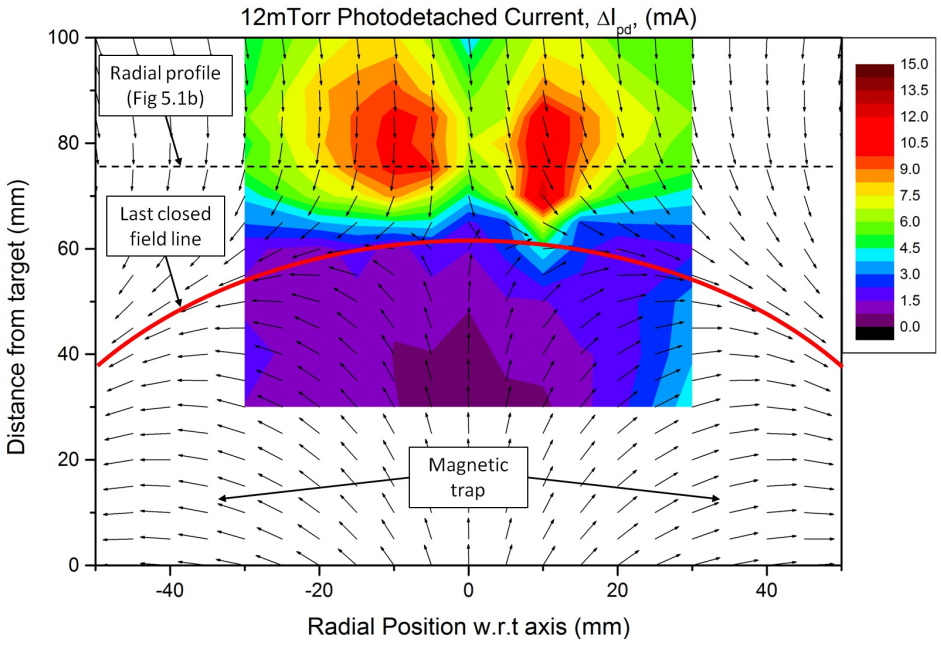

(a) Photodetached current distribution ΔI_{pd} (DC, 12 mTorr)

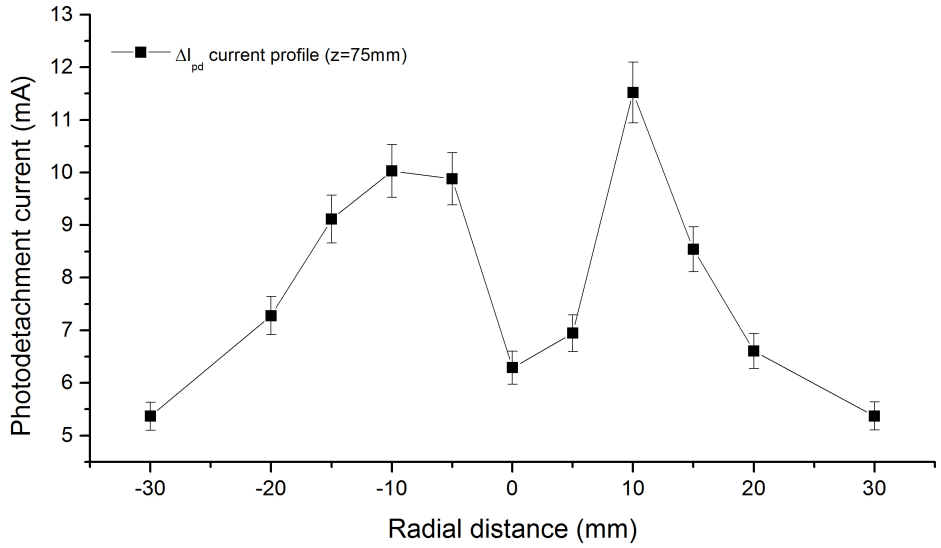

(b) Photodetached current ΔI_{pd} (DC, 12 mTorr) radial profile ($z = 75$ mm)

Figure 5.1: A 2-d plot of the measured photodetached current, ΔI_{pd} (mA). The magnetic field vectors (without magnitudes) are shown, together with a line representing the last closed flux surface separating the magnetic trap and the open plasma. A radial profile for the $z = 75$ mm position is also shown.

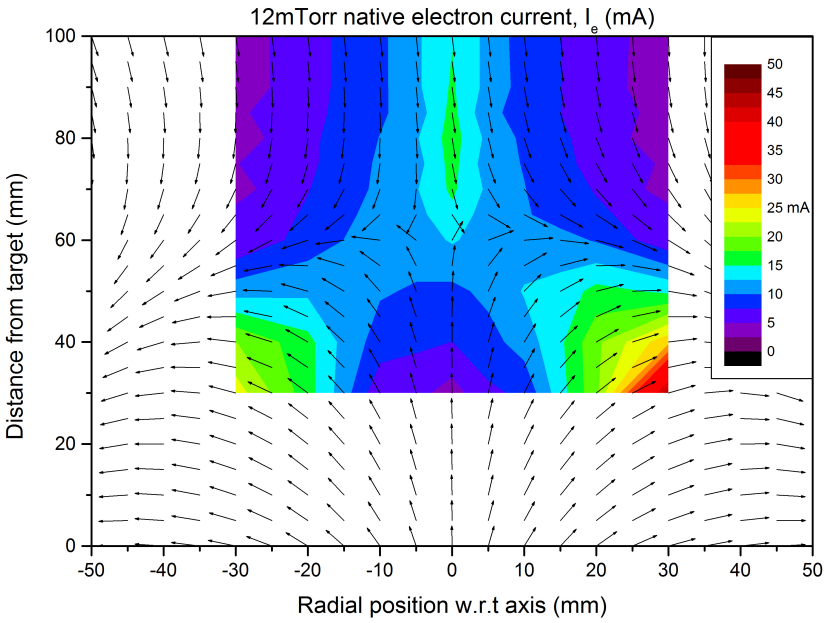

Figure 5.2: The 2-d plot of the native electron current I_e, at 1.59 Pa (12 mTorr) total pressure (0.31 Pa O_2 partial pressure).

and $r = -10$ mm, $z = 75$ mm. The measured n_- and α values are somewhat higher than those predicted from simulation [75, 77] however that model was developed for a small device operating at considerably lower pressure (0.02-0.24 Pa). The simulation gave peak values of $n_- \sim 2 \times 10^{15}\,\mathrm{m}^{-3}$ with $\alpha \sim 0.2$ and with a general shape of the O^- distribution with an annulus-like structure above the magnetic trap similar to our measurements. Although negative ions can be created throughout the magnetron discharge by a process of dissociative electron attachment ($e + O_2 \longrightarrow O^- + O$) with the fastest rates occurring where the electron densities are highest, it appears at this pressure 1.56 Pa/12 mTorr, at least, the negative ions accumulate in areas of most positive plasma potential and lower positive ion concentrations. That is, outside the magnetic trap region, where V_p is very negative [74, 78], and off the centreline where higher positive ion densities lead to their faster destruction through ion-ion recombination ($O^- + {O_2}^+ \longrightarrow O + O_2$, $O^- + {O_2}^+ \longrightarrow 3\,O$ and $O^- + O^+ \longrightarrow 2\,O$). Rate coefficient data collected by Panda et al. [48] and Bultinck et al. [75, 77] suggests that these are the most likely reactions in this case. Another channel for creation of O^- is through dissociative attachment of metastable oxygen (O_2^M, O_2^*) as also shown by Panda et al. [48]. Although these metastables can be created at copious rates, the decay of metastables into pairs of neutral oxygen atoms is far more dominant than the dissociative

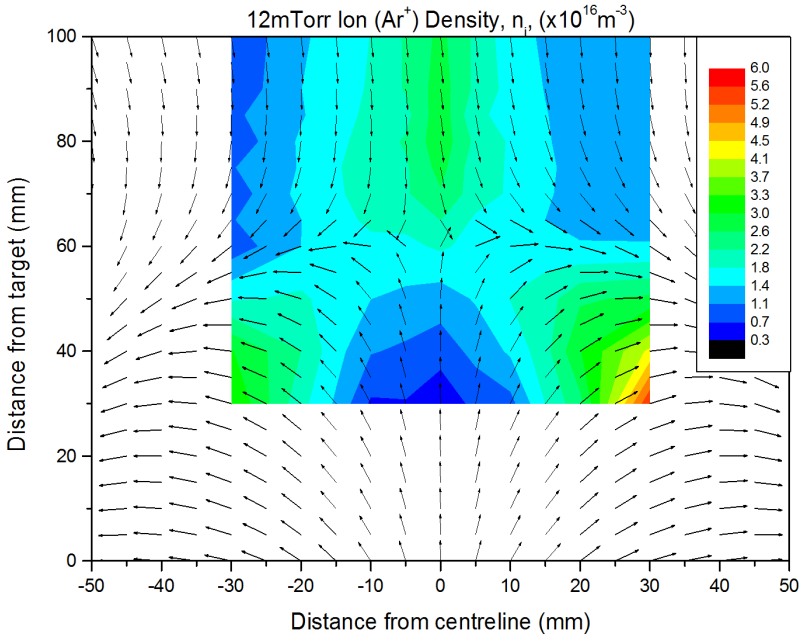

Figure 5.3: The 2-d plot of the spatial distribution of positive ion density, n_i, at 1.59 Pa (12 mTorr) total pressure (0.31 Pa O_2 partial pressure).

electron attachment of metastables to create O^- at the electron temperatures observed. However, for very low electron temperatures, for example in the afterglow of a pulsed discharge, high concentrations of O^- can be created from metastables as shown in [50].

Figures 5.6 - 5.9 show the affect of varying pressure on the distribution of α and n_-. At low pressure, 0.78 Pa/6 mTorr (figures 5.6 and 5.7), the negative ions (and correspondingly the α values) reside in a small annular region 30 mm above the top of the trap, however, at the highest pressure 2.40 Pa/18 mTorr, this distribution broadens radially and vertically and encroaches the top of the trap with negative ions now partially filling the central axis. With increasing O_2 partial pressure, the peak values of α and n_- rise, reaching $\alpha = 2.1$ and $n_- = 1.5 \times 10^{16}\,\mathrm{m}^{-3}$ respectively. This general trend with pressure can be understood from a simple model of the balance between creation and destruction rates of negative ions created in the bulk. As discussed in [25, 49] at pressures lower than around 4 Pa a balance between the negative ion formation rate

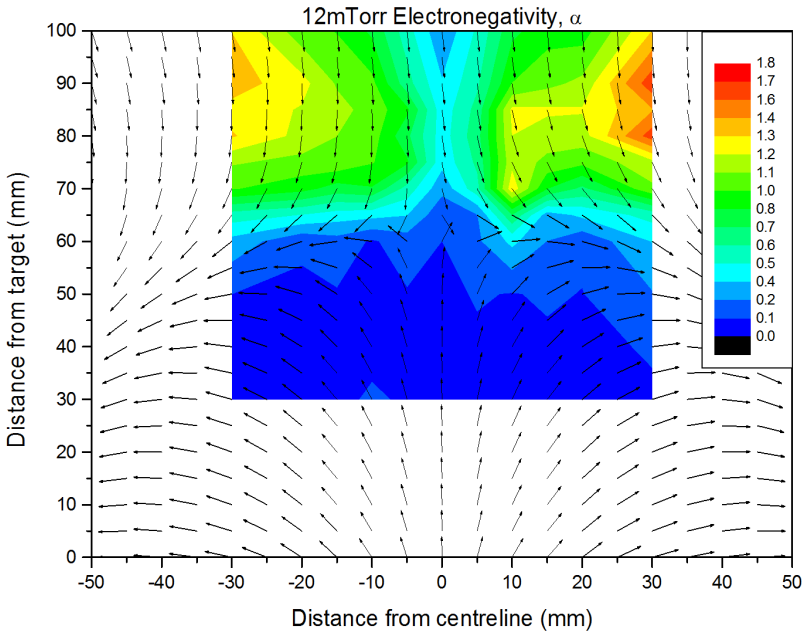

Figure 5.4: The 2-d plot of the spatial distribution of electronegativity, α, defined as the ratio of photodetached current to native electron current ($\Delta I_{pd}/I_e$) for 1.59 Pa (12 mTorr) total pressure (0.31 Pa O_2 partial pressure). Peak negative ion to electron density ratio, α =1.6.

$$\left(\frac{dn_-}{dt}\right)_{>0} = K_{da} n_{O_2} n_e \tag{5.1}$$

and the total ion-ion recombination loss

$$\left(\frac{dn_-}{dt}\right)_{<0} = K_{rec} n_- n_i \tag{5.2}$$

gives a prediction of the steady-state O^- density to be

$$n_- = \frac{K_{da} n_{O_2} n_e}{K_{rec} n_i} = \frac{K_{da} n_{O_2}}{K_{rec}\,[1+\alpha]} \tag{5.3}$$

where

$$K_{da} = 8.8 \times 10^{-17} \exp(-4.4/T_e)\,\mathrm{m^3\,s^{-1}} \tag{5.4}$$

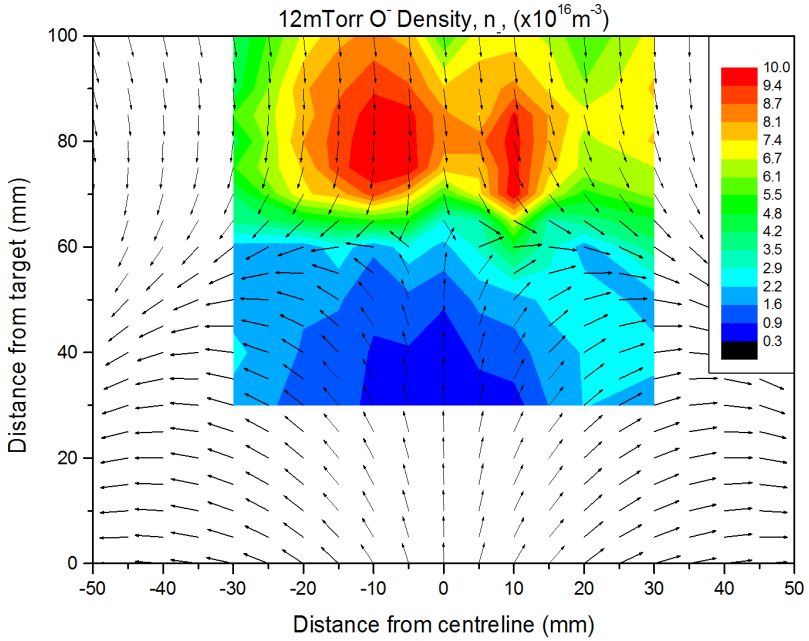

Figure 5.5: The 2-d plot of the spatial distribution of negative oxygen (O^-) density, n_- with magnetic field vector, for 1.59 Pa (12 mTorr) total pressure (0.31 Pa O_2 partial pressure).

is the rate constant for dissociative attachment [27] and

$$K_{rec} \approx 2.5 \times 10^{-13} \left[300/T_g\right]^{1/2} \text{ m}^3\,\text{s}^{-1} \tag{5.5}$$

is the rate constant for ion-ion recombination [48]. Here T_e is the electron temperature in eV, T_g is the neutral temperature in °K and n_i the total ion density given by $n(Ar^+) + n_{O_2^+} + n_{O^+}$. Since the rate constants for negative ion recombination with O^+, $O_2{}^+$ and Ar^+ are similar these have been lumped into a single rate constant (with $K_{rec} = 2.5 \times 10^{-13}\,\text{m}^3\,\text{s}^{-1}$) as in [25]. It has been assumed that there is no loss of species due to diffusion. For weakly electronegative plasmas ($\alpha \ll 1$)

$$n_- \propto n_{O_2} \propto P_{O_2} \tag{5.6}$$

P_{O_2} is the O_2 partial pressure $\propto$ to chamber pressure in this case. For strongly electronegative plasmas ($\alpha \gg 1$)

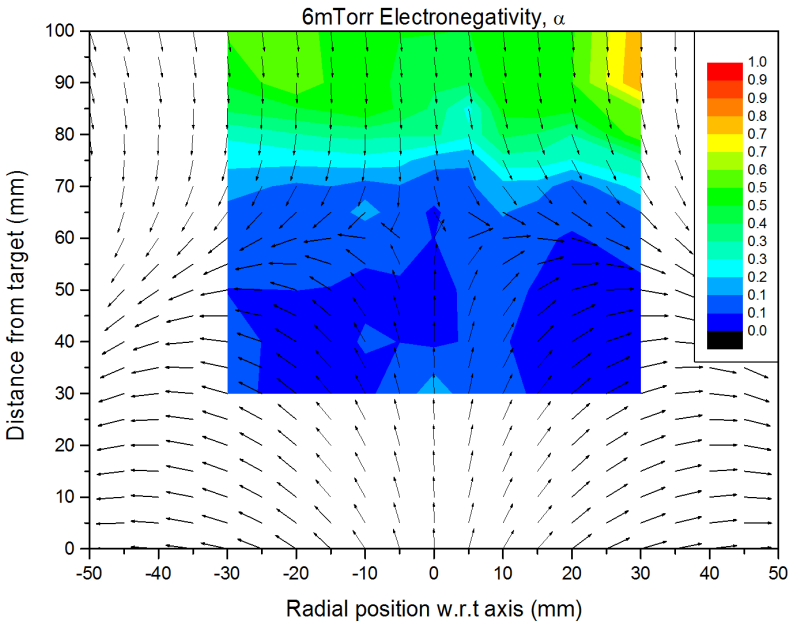

Figure 5.6: The 2-d plot of electronegativity, α, for 0.79 Pa (6m Torr) total pressure (0.16 Pa O_2 partial pressure). Peak negative ion to electron density ratio, α =0.8.

$$n_- \propto n_e^{1/2} n_{O_2}^{1/2} \propto n_e^{1/2} P_{O_2}^{1/2} \tag{5.7}$$

Therefore, the O^- densities are expected to increase at a rate at least as fast as $P_{O_2}^{1/2}$ and up to rates proportional to P_{O_2} as the oxygen partial pressure is increased. Unfortunately in the densest regions $\alpha \sim 1$, and so the values fall between the approximations in the simple model above. To test the above relations O^- density data from regions of high and low electronegativity in the discharge (in the annulus and at positions near the centreline close to the target) can be plotted against O_2 partial pressure. However, the above analysis does not take into account the transport (diffusion and mobility) of negative ions out of the different regions and therefore will always give similar densities for the same oxygen partial pressures in all regions of the discharge.

For the central region in particular, transport of negative ions to regions of more positive potential may be rapid, resulting in lower densities along all of the centreline. Introducing a loss time τ, an equation for the effective destruction (loss) rate of O^- ions (equation 5.2) can be modified to

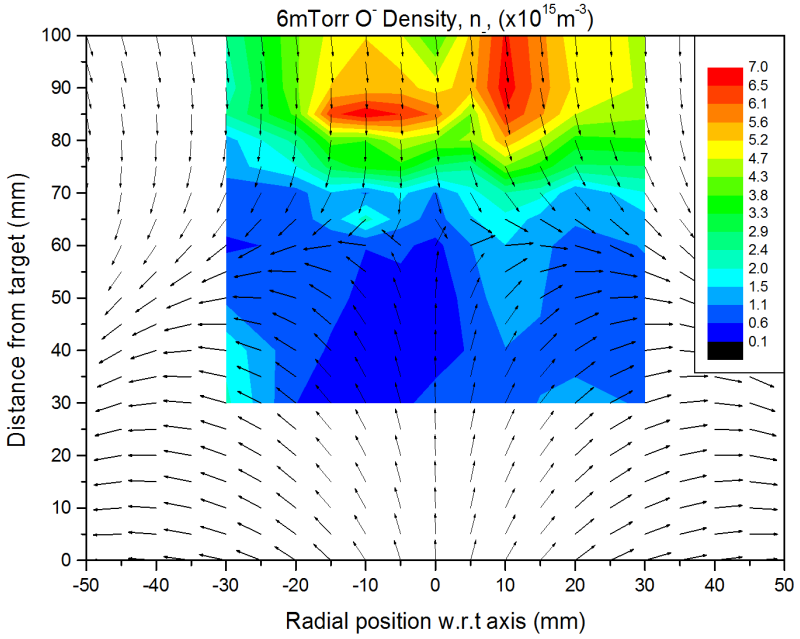

Figure 5.7: The 2-d plot of negative oxygen (O^-) density, n_- with magnetic field vector, for 0.79 Pa (6m Torr) total pressure (0.16 Pa O_2 partial pressure).

$$\left(\frac{dn_-}{dt}\right)_{<0} = K_{rec} n_- n_i + \frac{n_-}{\tau} \tag{5.8}$$

When equated to the creation rate the resultant density is given by

$$n_- = \frac{K_{da} n_{O_2} n_e}{[K_{rec} n_i] + \frac{1}{\tau}} \tag{5.9}$$

Figure 5.10 shows a number of experimentally determined values of n_- plotted against O_2 partial pressure for regions with $\alpha < 0.2$ (centreline) and for $\alpha > 1.8$ (in the annulus) together with predictions for the O^- density based on the simple transport model above. Here, best fit values of τ for the two regions have been found: these are $\tau \sim 10\,\mu$s for the central zone and $\tau \sim 100\,\mu$s for the dense region. For positions of low α, (close to the centreline towards the target) n_- increases linearly with pressure as predicted. In the dense annulus region with high α, n_- values depart from the simple predictions at low pressure.

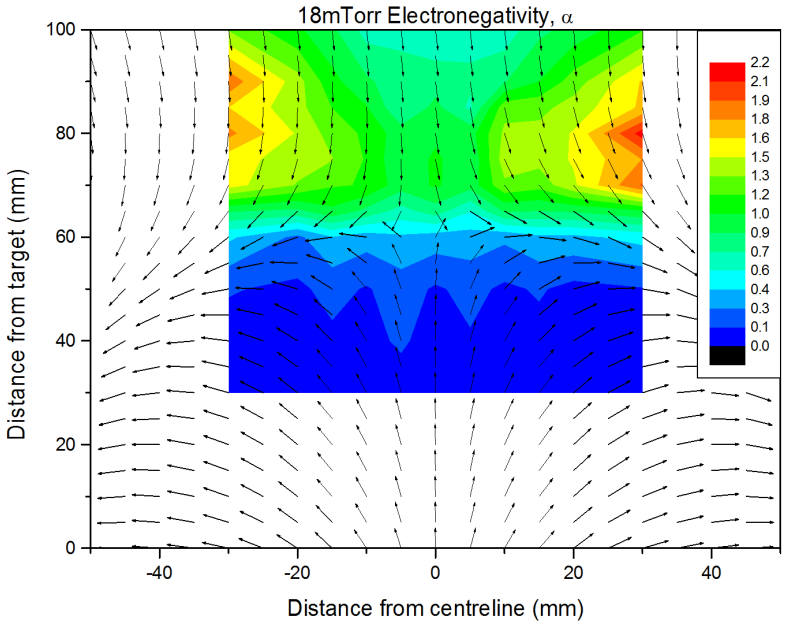

Figure 5.8: The 2-d plot of electronegativity, α, for 2.40 Pa (18 mTorr) total pressure (0.48 Pa O_2 partial pressure). Peak negative ion to electron density ratio, α =2.1.

Close to the centreline the rate of negative ion loss may be governed by drift (of velocity v_d) in the electric fields due to the potential gradients from central region to the more positive space potential regions outside and above the trap. Although the plasma potential measurements are somewhat unreliable from the probe study here (as described more below), previous studies using an emissive probe show consistently a few volts difference $\Delta\phi$ across the regions separated by a distance $L \sim 1$ cm [72]. This gives $\tau = L/v_d \sim 0.1/5 \times 10^3 \sim 20\,\mu$s for $v_d = (2e\Delta\phi/m_i)^{1/2}$, a figure consistent with measurements. For the outer dense regions diffusion may be the dominant transport process; however ion-ion recombination will account for most of the O^- losses. A diffusion coefficient, D for negative ions can be written as $D = 1/3\lambda v_{th}$ where λ is the mean-free path and v_{th} the ion thermal velocity, giving a characteristic loss time $\tau \sim L^2/D$. With $L = 1$ cm, $\lambda = 4$ cm, $v_{th} = 300\,\mathrm{m\,s^{-1}}$ (for a pressure of 2.4 Pa) we obtain $\tau \sim 100\,\mu$ s, again a figure consistent with the predicted τ from matching of model to the experimental data.

The results and the simple model suggest a picture where the transport rates of non-confined negative ions from regions where α is small is considerably

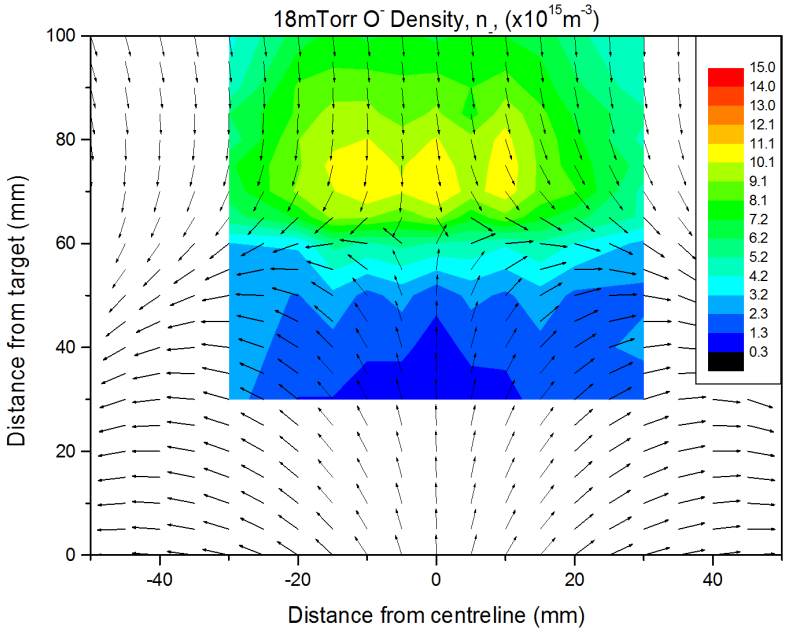

Figure 5.9: The 2-d plot of negative oxygen (O^-) density, n_- with magnetic field vector, for 2.40 Pa (18 mTorr) total pressure (0.48 Pa O_2 partial pressure).

higher than from in regions of high O^- density, where the more positive potentials hinder diffusion losses. However, this picture does not account for energetic negative ions in the plasma. A large proportion of the negative ions detected in regions of low α may in fact be energetic species from the cathode target, and we would not expect their density to rise with increased O_2 partial pressure as the surface conditions at the target are unaffected by additional oxygen in a fully poisoned system.

The measured trends and simple model description of increasing O^- density with pressure are contrary to the predictions in [77] where n_- was found to decrease not increase. The authors noted that the decreasing trend of the O density was unexpected, but may be a consequence of rising O^+ and $O_2{}^+$ densities with pressure, which lead to higher recombination rates and therefore a lowering of n_- upon O_2 addition. Their predictions do however show the same kind of spreading of O^- ions with increasing pressure, and such phenomena are associated with a growth in areas of positive plasma potential regions in the bulk plasma.

Here it is found that the plasma potential becomes more positive (5.5 to 6.5 V in the regions of high negative ion density) with increasing pressure

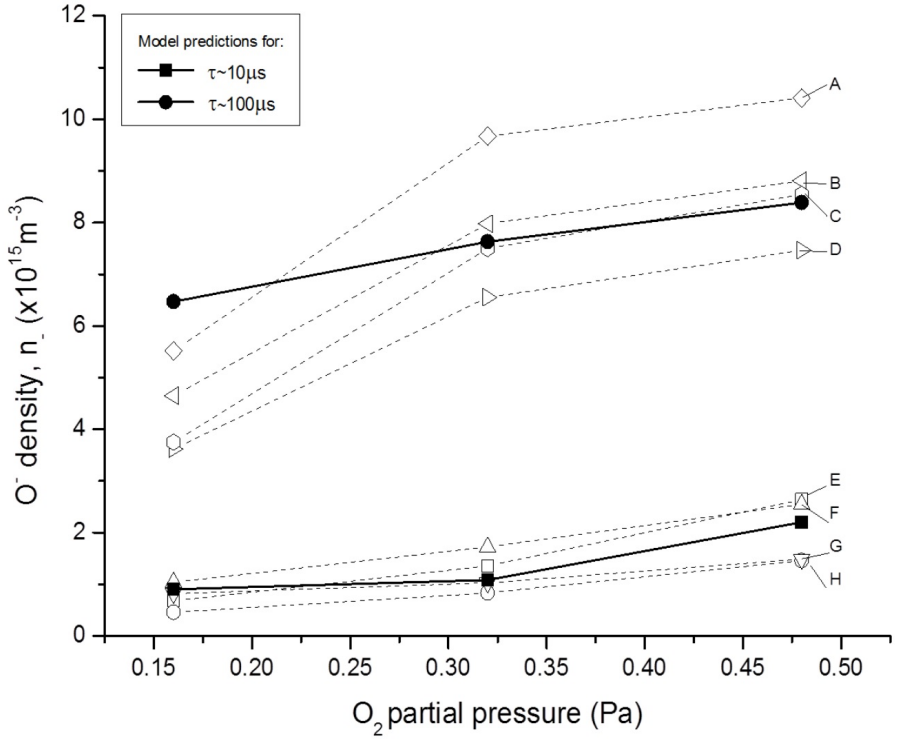

Figure 5.10: Plot of n_- against O_2 partial pressure (Pa) for different positions, for $\alpha < 0.2$ and $\alpha > 1$, with simple model predictions of these quantities. Co-ordinates (r,z) of positions are $A = (10, 80)$; $B = (15, 80)$; $C = (30, 80)$; $D = (20, 80)$; $E = (-5, 50)$; $F = (-5, 40)$; $G = (5, 50)$; $H = (5, 40)$. Solid lines represent simple predictions for n_- at $\alpha > 1$ ($\tau \sim 100\,\mu$s) and at $\alpha \ll 1$ ($\tau \sim 10\,\mu$s)

over the measured range, with a general expansion of the positive potential region also noted in [75, 77]. The measurements using the second derivative method as described in section 3.1 are however too prone to errors ($> \pm 1V$) to look at the fine detail, and the distributions are therefore not plotted. An emissive probe could be used to get more precise plasma potential values as demonstrated already in the magnetron [74].

Here it can be argued that since significantly higher O^- densities are observed than in [77] the larger density gradients lead to a faster rate of transport away from such regions, naturally spreading the ions to larger areas. Without a much more detailed analysis of the plasma chemistry taking into account the different magnetron arrangements, (this experiment and the simulation are of a different geometry with different pressure ranges), it may be difficult

to make reliable qualitative comparisons.

The dense negative ion regions, namely those areas for $z > 60\,\mathrm{mm}$ corresponds to part of the plasma where a substrate would normally sit. Although few of the measured O^- ions created in the plasma bulk are able to bombard an electrically isolated or negatively biased substrate, such high electronegativities ($\alpha > 2$) will change the Bohm criterion (as already mentioned, a modified Bohm criterion in electronegative plasmas is demonstrated [44, 72]), decreasing the positive ion flux to the growing film, when compared to a negative ion-free plasma of equal positive ion density. It is important that this effect is taken into account when making accurate assessments of the ion fluxes and ion energy (heat) fluxes to substrate mounted electrical probes.

5.3 Conclusions

The spatial distribution of negative oxygen ion O^- densities have been successfully measured using a combination of the eclipse-photodetachment technique and Langmuir probing in a low power circular dc reactive plasma for a range of pressures 0.78 to 2.40 Pa with fixed 20% oxygen partial pressure. O^- ions exist predominantly in the high potential regions of the plasma above the closed field region of the magnetic trap and confined to an annulus-shaped region around the central axis. With increasing pressure the O^- densities increase reaching a peak value $1.5 \times 10^{16}\,\mathrm{m}^{-3}$, corresponding to a concentration twice that of the electron density in that region. The area of highest O^- densities spreads out with increasing pressure, until O^- ions start to occupy the central magnetic field-free region on the centre line and encroach on the top of the magnetic trap. The results show highly electronegative plasma regions in the areas of the plasma that are typically occupied by the substrate during film growth.

Chapter 6

Time-Resolved 2D Spatial Distributions in O_2/Ar Pulsed Discharges

6.1 Experimental method

Following on from the steady-state DC study outlined in chapter 5, the spatial distribution study was extended to a pulsed-dc discharge, allowing the temporal evolution of the distribution to be plotted. Spatial measurements were made in a region of the plasma defined by 0 mm$\leq$r$\leq$ 30 mm relative to the discharge centreline and 30 mm$\leq$z$\leq$ 100 mm relative to the target surface, and at 10 μs intervals throughout the discharge pulse.

The discharge was operated with a unipolar dc power supply, pulsed with a 'chopper' circuit to control the duty-cycle and frequency. A 50 μs on-phase was chosen at a frequency of 5 kHz, giving a duty cycle of 25%. The discharge was current-regulated to give an average cathode current of 0.25 A over the pulse cycle (peak on-time current of 0.72 A) shown in figure 6.1. This ensured an average power of 100 W over the cycle (peak on-time power of 245 W). Calculated instantaneous power is plotted in figure 6.2.

O_2 partial pressure was set to 20% (as in the steady-state experiment), and the pressure was set to 10 mTorr (a pressure shown by Dodd to give optimal values for α [25]). The laser and probe parameters remain unchanged from those used in steady-state dc.

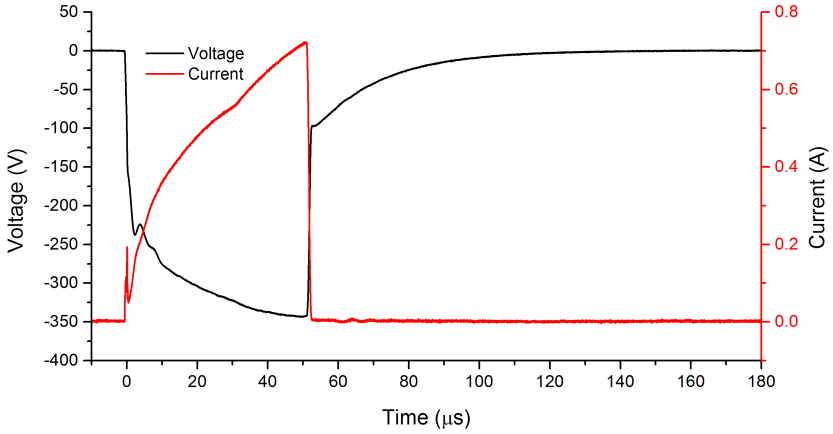

Figure 6.1: Current and voltage profiles for the pulsed discharge. Pulse frequency was set to 5 kHz for a 50 μs on-phase duration, giving a duty cycle of 25%.

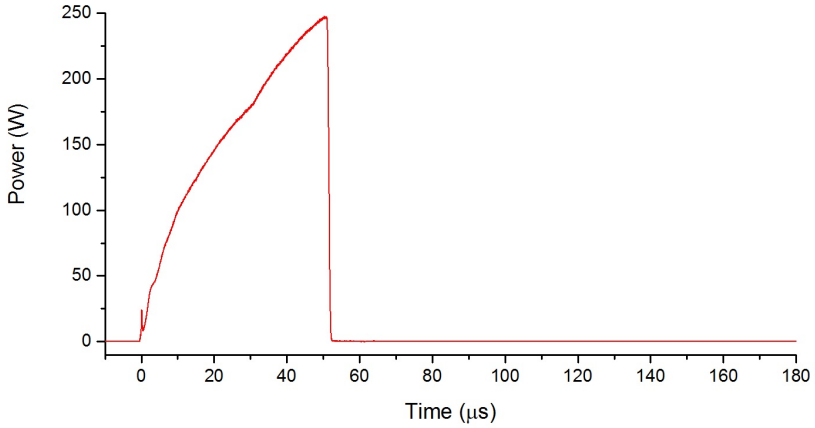

Figure 6.2: Calculated instantaneous power for the pulsed discharge. Peak on-time power was 245 W with an average of 100 W over the cycle.

6.2 Results and Discussion

The temporal evolution of on-phase ion density, with the magnetic field vector overlaid, is plotted in figures 6.3a - 6.3e and the off-phase densities in figures 6.4a - 6.4f. The on-phase distribution shows the now distinctive distribution of plasma density, following the same pattern as observed in the steady state dc case. That is, peak ion densities occur inside the magnetic trap, close to the racetrack area of the discharge, and away from the centreline. Higher

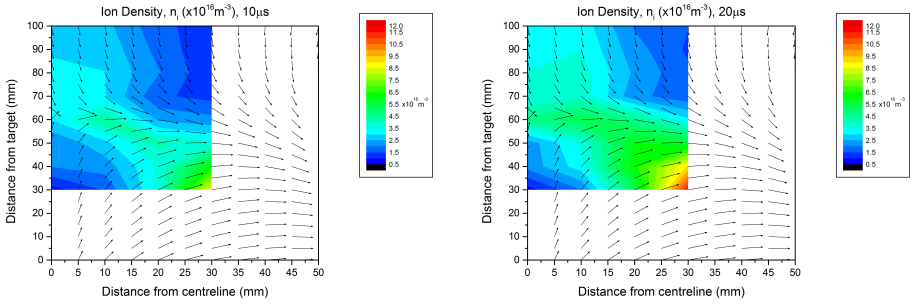

(a) 10 μs

(b) 20 μs

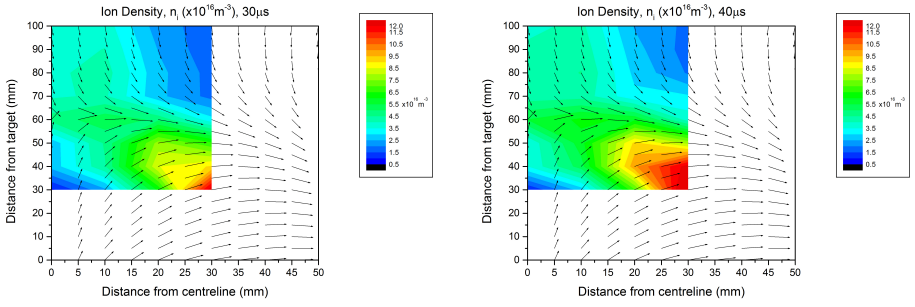

(c) 30 μs

(d) 40 μs

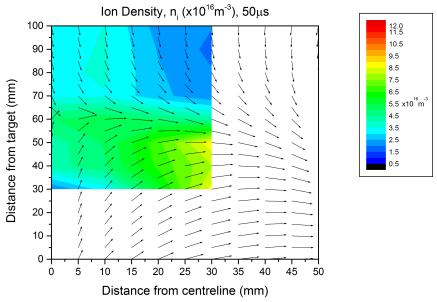

(e) 50 μs

Figure 6.3: The evolution of the spatial distribution of ion density n_i during the on-time of a pulsed discharge. O_2 partial pressure was 20% of the total pressure (10 mTorr). Average power over the pulse was 100 W, with a peak on-phase instantaneous power of 245 W.

densities are also observed on the centreline of the discharge, above the null and further away from the target. This distribution has also been observed in other discharges, and is known to be a result of the magnetic mirror at the null position. The plasma density shows a relatively uniform increase during the on-phase for most positions. The peak ion density in the on-phase

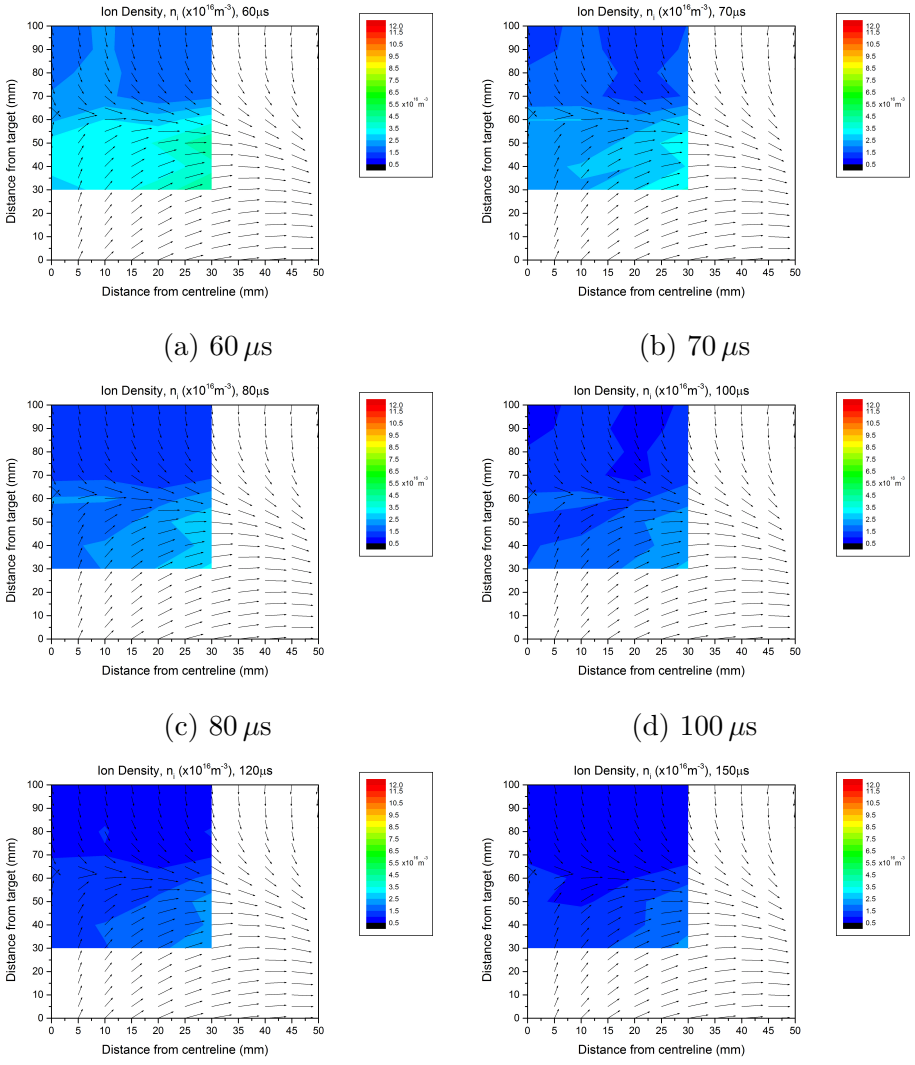

(a) 60 μs (b) 70 μs

(c) 80 μs (d) 100 μs

(e) 120 μs (f) 150 μs

Figure 6.4: The evolution of the spatial distribution of ion density n_i during the off-time of a pulsed discharge. O_2 partial pressure was 20% of the total pressure (10 mTorr). Average power over the pulse was 100 W, with a peak on-phase instantaneous power of 245 W.

of $n_i = 1.2 \times 10^{17}\,\mathrm{m}^{-3}$ occurs at 40 μs (near the end of the on-phase) at a position r=30 mm, z=30 mm. This is close to the racetrack region of the discharge, and well within the magnetic trap.

In the off-phase the ion density declines rapidly, with the ions appearing

to linger in the trap-region longer than elsewhere, with the higher densities on the centreline and above the null disappearing rapidly (within 10 μs of the transition), compared to those in the trap which remain in higher concentrations for upwards of 50 μs after the active phase. In order to compare the results with those of previous studies, the plasma density along the centreline of the discharge was plotted against the distance from target, for various timesteps in the on- and off-phases. This is shown in figures 6.5a (on-time) and 6.5b (off-time).

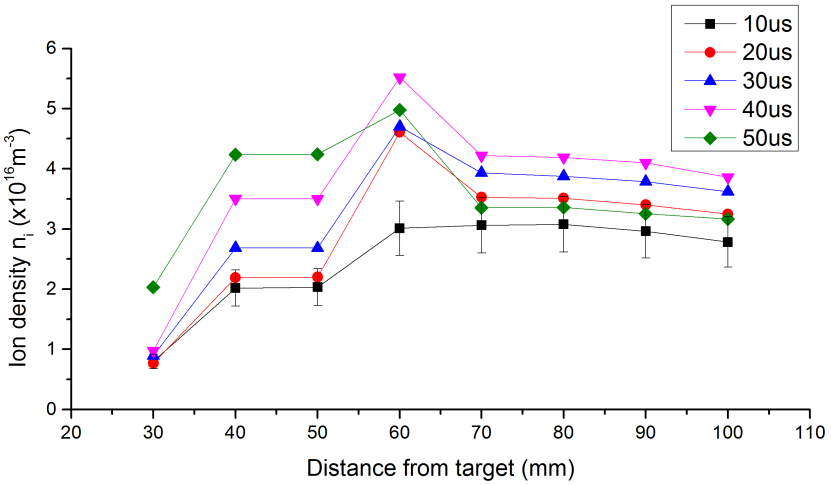

(a) On-time.

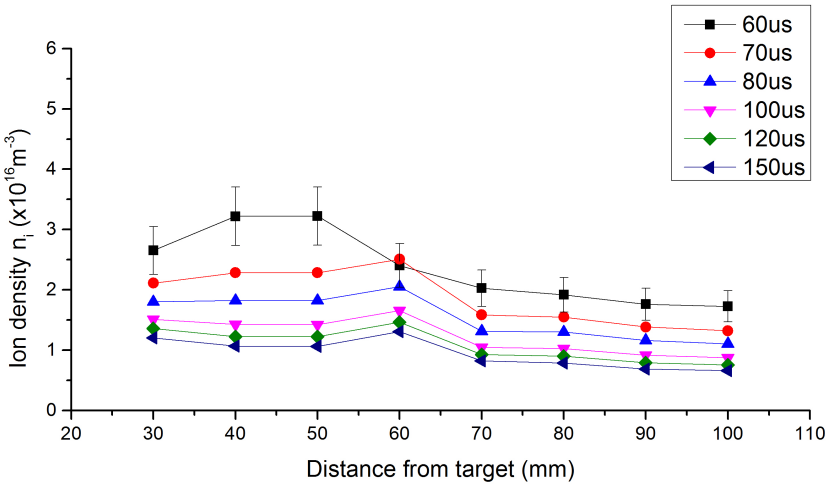

(b) Off-time.

Figure 6.5: The ion density of the pulsed plasma as a function of position on the centreline, shown for the a.) on- and b.) off-phases of the pulsed discharge.

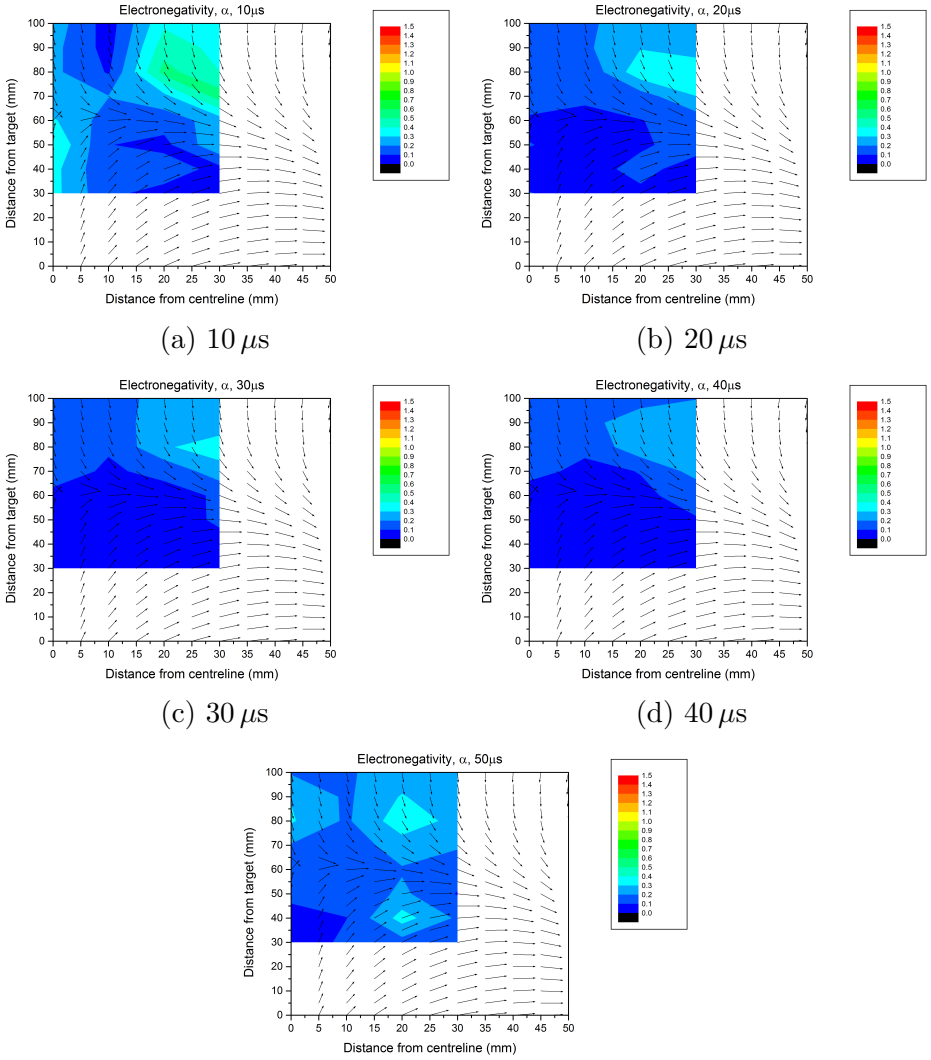

(a) 10 μs (b) 20 μs

(c) 30 μs (d) 40 μs

(e) 50 μs

Figure 6.6: The evolution of the spatial distribution of current ratio $\Delta I_{pd}/I_e = \alpha$ during the on-time of a pulsed discharge. O_2 partial pressure was 20% of the total pressure (10 mTorr). Average power over the pulse was 100 W, with a peak on-phase instantaneous power of 245 W.

This shows reasonably good agreement with the trends observed previously in the magnetron (figure 2.5), with densities showing a general increase through the on-time, then decreasing in the off, with a peak just above the null position. The discharge pulse used in the previous study was operated at a much higher frequency of 100 kHz and a 50% duty cycle, indicating that the

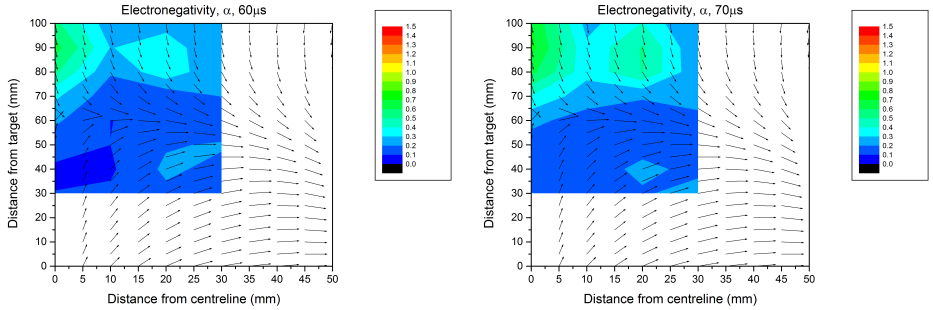

(a) 60 μs

(b) 70 μs

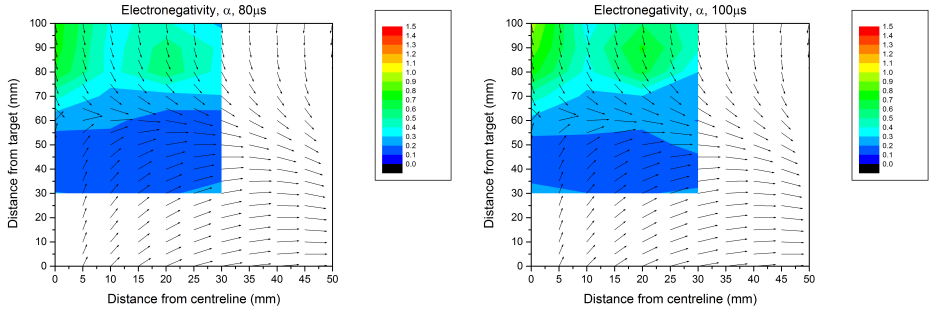

(c) 80 μs

(d) 100 μs

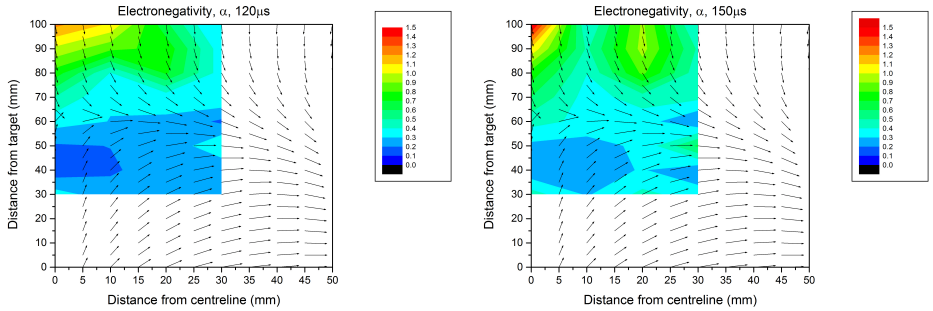

(e) 120 μs

(f) 150 μs

Figure 6.7: The evolution of the spatial distribution of current ratio $\Delta I_{pd}/I_e = \alpha$ during the off-time of a pulsed discharge. O_2 partial pressure was 20% of the total pressure (10 mTorr). Average power over the pulse was 100 W, with a peak on-phase instantaneous power of 245 W.

spatial distribution of ion densities, along the centreline at least, is relatively independent of pulse frequency and duty-cycle. Values in this case are up to a factor of 2-3 higher than in the previous study (depending on distance from the target), however it should be noted that the values plotted in figure 6.5 are ion density as calculated by the OML technique, and not electron

densities calculated from the current at the plasma potential, as plotted by Dodd. Furthermore, quasi-neutrality might suggest that the ion density, $n_i = n_e + n_-$, the sum of the electron and negative ion densities. The values of electron and O^- density published in [51], when summed, reach a maximum of $\sim 3 \times 10^{16}\,\mathrm{m}^{-3}$ at the peak position $\approx 60\,\mathrm{mm}$ from the target surface, still a factor of $\sim$2 less than the peak ion density measured here. This could be explained by the difference in analysis methods for the Langmuir probe characteristics (calculating n_e from I_e at V_p is known to be an error-prone method), or by the tendency of the magnetron to give different values on different experiments for nominally the same plasma parameters (as discussed in earlier chapters). It seems clear, however, that even if absolute values do not match, the density distribution of ions (and, by inference, electrons) is somewhat independent of discharge conditions, at least on the centreline of the discharge.

The current ratio $\Delta I_{pd}/I_e$ assumed to be $= \alpha = n_-/n_e$ is plotted in figures 6.6a - 6.6e (on-phase) and 6.7a - 6.7f (off-phase). Here, a distribution broadly similar to the 1.59 Pa (12 mTorr) dc case (figure 5.4) is observed throughout the on-phase of the pulse, with peak on-time values of $\alpha \approx 0.4 - 0.5$ being recorded off the centreline and away from the target, above the magnetic trap, with lower values elsewhere. These values for α are noticeably lower than in the steady-state dc measurements, although they are consistent with measurements made in previous studies [49, 51]. Also notable is a surge in α close to the phase transitions, with higher values being observed soon after the beginning of the on-phase (at $10\,\mu$s) and at the on-off phase transition ($50\,\mu$s). As in the steady-state dc discharge, there remains an annular structure positioned 15-20 mm off-axis where α is considerably higher than its surroundings. This distribution is sustained throughout the on and off phases of the pulse, although the shape becomes more distinct in the off-time. Values for α are seen to increase everywhere throughout the off-time, with a peak of $\alpha = 1.6$ being observed far into the off-phase at $150\,\mu$s. It is interesting to observe a shift in the distribution of α during the off-phase, with high values being measured on the centreline as well as in the regions of low ion density above the magnetic trap, an observation different from steady-state dc. This could be due to the extremely rapid fall-off in ion density on the centreline (figure 6.8a) which occurs at the transition. If we assume $n_e \approx n_i$, then a rapid drop of n_e would result in a similar drop of I_e and consequently an increase in α if the falloff in ΔI_{pd} is less rapid, as would appear to be the case (6.8b).

Negative ion density n_- is plotted in figures 6.9a - 6.10f. The general shape of the distribution resembles the distribution observed in dc, with peak densities

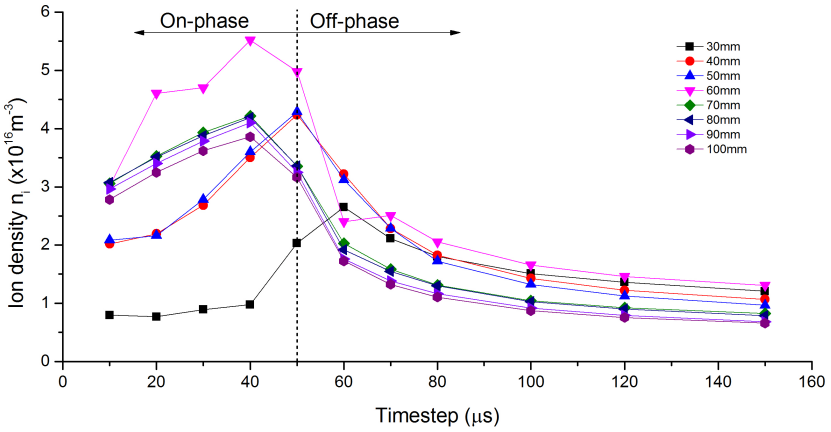

(a) Temporal evolution of ion density n_i on the centreline of the discharge, showing a rapid falloff in density when the discharge is switched off.

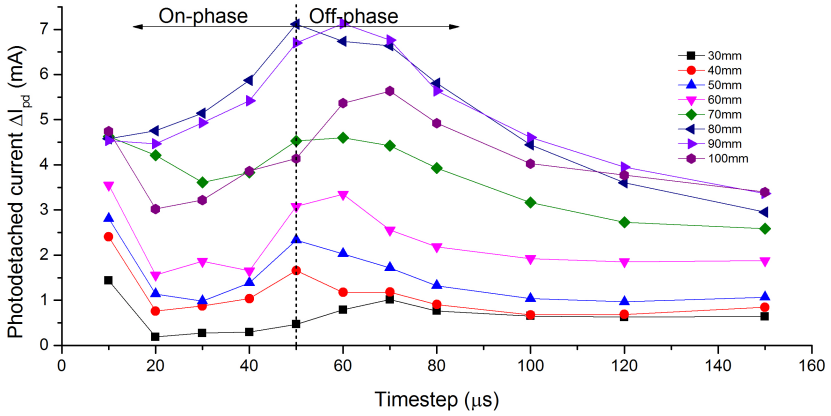

(b) Temporal evolution of photodetachment current ΔI_{pd} on the centreline of the discharge, showing a slow falloff for positions of peak α far from the target ($z \geq 70\,\mathrm{mm}$).

Figure 6.8: Temporal evolution of n_i and ΔI_{pd} on the discharge centreline.

being observed above the trap, away from the centreline, with an off-axis peak density of $\sim 7 \times 10^{15}\,\mathrm{m}^{-3}$ observed soon after the discharge is struck ($10\,\mu\mathrm{s}$) at a position $r = 20\,\mathrm{mm}$, $z = 80\,\mathrm{mm}$. This represents the 'centre' of the annular structure consistent with that described in chapter 5, and with the observations of You *et al.*, who observed a peak density (albeit on the centreline and not off-axis) at the same timestep for the same discharge pulse parameters [49]. High negative ion densities are observed at this position for all times during the on-phase. Densities are significantly lower in the

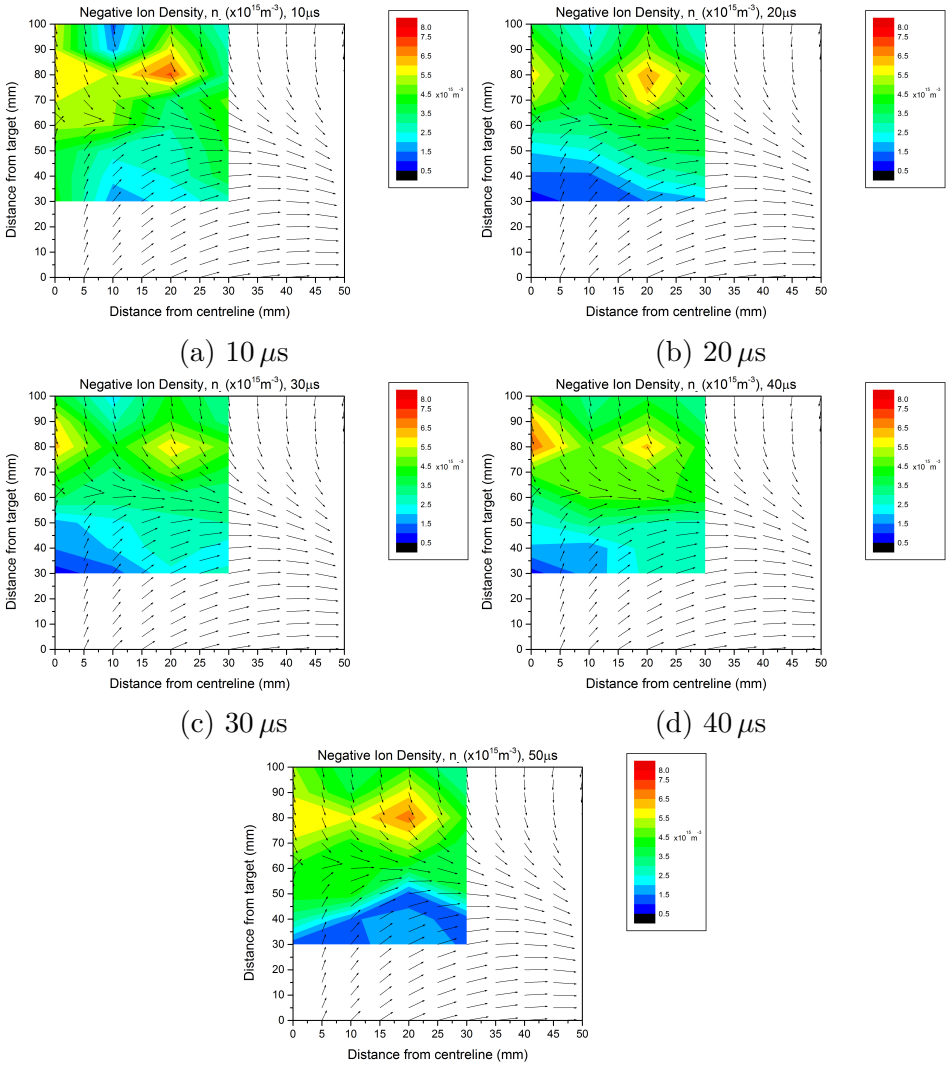

(a) 10 μs (b) 20 μs

(c) 30 μs (d) 40 μs

(e) 50 μs

Figure 6.9: The evolution of the spatial distribution of negative ion density n_- during the on-time of a pulsed discharge. O_2 partial pressure was 20% of the total pressure (10mTorr). Average power over the pulse was 100 W, with a peak on-phase instantaneous power of 245 W.

region closer to the target (within the trap), as in the dc case. Unlike the steady-state dc case, however, where there is a rapid drop in density coinciding approximately with the location of the last closed field-line of the trap (figures 5.5, 5.7 and 5.9), a clear boundary between high and low density regions does not appear in pulsed mode. Instead, a more gradual decline in density towards the target is observed at all times during the on-phase. A density peak is also

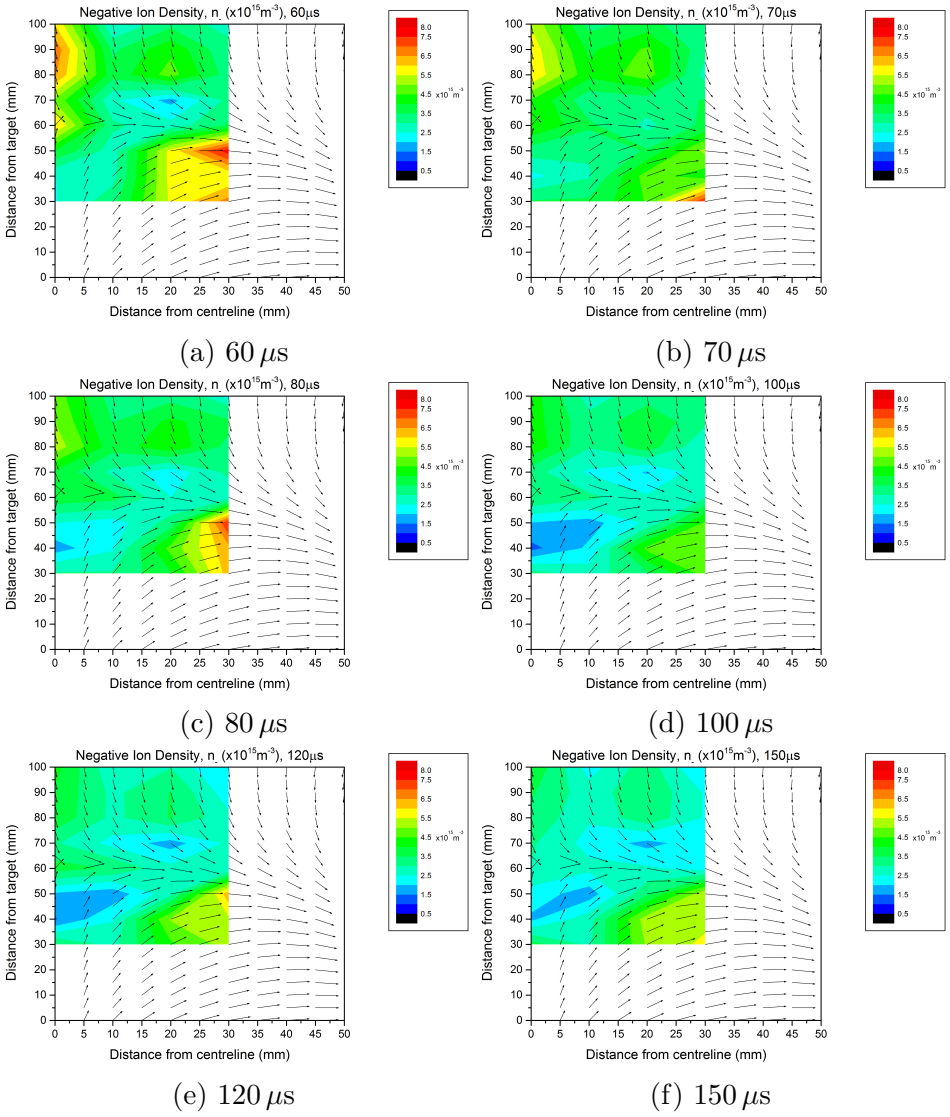

(a) 60 μs (b) 70 μs

(c) 80 μs (d) 100 μs

(e) 120 μs (f) 150 μs

Figure 6.10: The evolution of the spatial distribution of negative ion density n_- during the off-time of a pulsed discharge. O_2 partial pressure was 20% of the total pressure (10 mTorr). Average power over the pulse was 100 W, with a peak on-phase instantaneous power of 245 W.

observed at a distance of ~ 80 mm from the target on the discharge centreline, different from the steady-state dc case but consistent with measurements made in previous pulsed-dc studies [49–51].

In the off-phase of the distribution, the negative ion density is seen to decline at most positions, but much less rapidly than the ion density (figure 6.11a).

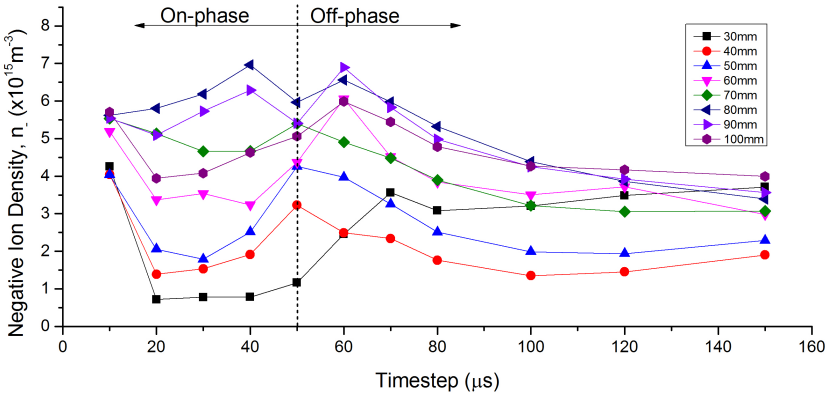

(a) Temporal evolution of negative ion density n_- on the centreline of the discharge, showing a slow falloff in density when the discharge is switched off.

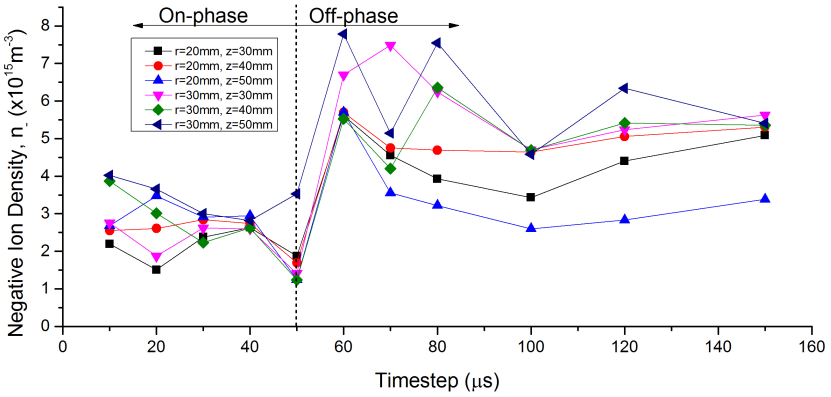

(b) Temporal evolution of negative ion density n_- in the trap region of the discharge, showing a sharp rise in n_- shortly after the on-off transition, and a slow falloff throughout the off-phase.

Figure 6.11: Temporal evolution of n_- on the discharge centreline, and in the trap region closer to the target.

The sharp rise in n_- in the afterglow, as observed by You *et al.* in [50], was not present in this study, with the O^- density being seen to drop in the same positions on the centerline where a rise was previously detected. This could be a result of the difference in plasma potentials between the two studies. Off-time plasma potentials in excess of +20 V were reported in in [50], which would lead to a significantly larger reading for ΔI_{pd} when the probe is biased ~ 30 V more positive than this. In this study, off-time plasma potentials were observed to be low at all locations, with values of $\sim 1.0-2.0$ V consistent with the DC measurements. Typical on- and off-phase plasma

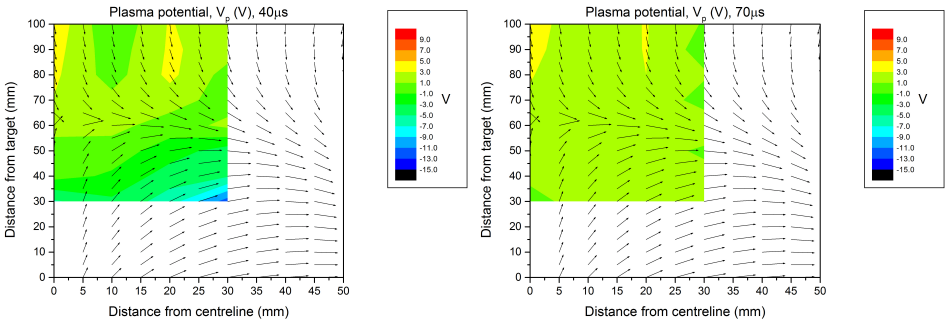

(a) 40 μs (b) 70 μs

Figure 6.12: The plasma potential V_p plotted at $t = 40\,\mu$s and $t = 70\,\mu$s, showing potentials typical of the on- and off-phases of the pulse respectively.

potentials are plotted in figure 6.12 (plots for the other timesteps can be found in the appendix). Plasma potentials were estimated *in situ* from the zero crossing-point of d^2I_e/dV^2, however the error in this method (± 1.0 V) means that the exact values of V_p are unknown. The discrepancy between this study and those of Dodd, You *et al* might also be explained by the differences in discharge powers between the experiments. This experiment was performed with an average power much higher (more typical of commercial discharges) than those used in previous experiments. This provides some support to the suggestion that O^- density is sensitive to the average discharge power as mentioned in chapter 2, and [48].

In the trap region of the discharge, however, a different trend is observed (figure 6.11b). Here, the density rises sharply above the on-phase value, and remains high for the duration of the off-phase, with a slow decline towards the end of the off-phase for most positions. This trend with time is not observed in other regions of the discharge. One possible explanation stems from the discharge voltage waveform (figure 6.1), which does not return immediately to ground at the phase transition. There is a rapid drop in target potential from -350 V to -100 V at t=50 μs, however the falloff to ground throughout the remainder of the off-phase is much slower. As a result of the non-ideal pulse, the electrons in the trap region may be inhibited from returning to ground as rapidly as in the ideal case, remaining instead trapped within this region during the afterglow. This can be inferred from the slower fall-off in ion density in this region (figure 6.4) than elsewhere in the discharge, if n_e is assumed by quasi-neutrality to follow the same behaviour of n_i. As discussed in chapter 5, the presence of metastable molecules (O_2^M) in the plasma leads to production of negative ions by dissociative attachment of cold electrons. Since

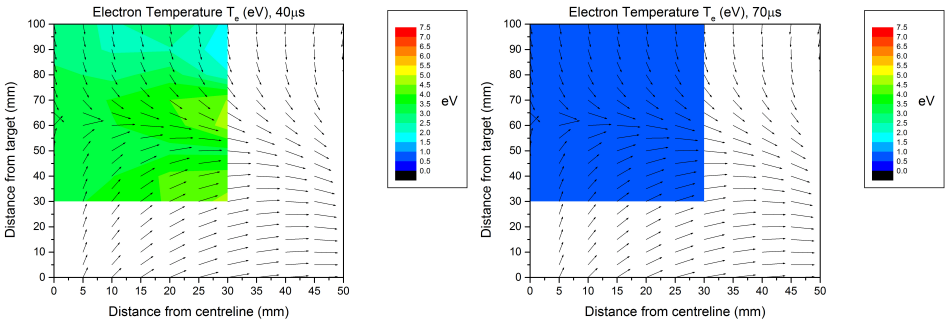

(a) 40 μs (b) 70 μs

Figure 6.13: The electron temperature T_e plotted at $t = 40\,\mu$s and $t = 70\,\mu$s, showing temperatures typical of the on- and off-phases of the pulse respectively.

O_2^M is neutral, and therefore not affected by electro-magnetic considerations, it is reasonable to assume that they are present everywhere in the plasma, although the production and destruction rates of such molecules may vary depending on local plasma temperature. Panda gives the rate coefficient for production (excitation, reaction $K(O_2^M)$) and loss (dissociation, reaction K_d, and dissociative attachment, reaction K_{da}) of O_2^M via the reactions given in table 6.1 [48].

	Reaction	**Rate Coefficient K ($\mathbf{m^3\,s^{-1}}$)**
$K(O_2^M)$	$O_2 + e \longrightarrow O_2^M + e$	$1.27 \times 10^{-14} T_e^{-0.52} \exp(-7.66/T_e)$
K_d	$O_2^M + e \longrightarrow 2\,O + e$	$8.95 \times 10^{-15} T_e^{-0.48} \exp(-4.32/T_e)$
K_{Mda}	$O_2^M + e \longrightarrow O^- + O$	$-1.69 \times 10^{-18} + 6.27 \times 10^{-16}/T_e - 1.30 \times 10^{-16}/T_e^2 + 9.60 \times 10^{-18}/T_e^3$

Table 6.1: Rate coefficient expressions for production and loss of O_2^M

These expressions can be simplified somewhat by incorporating the measured temperatures in the discharge, and calculating a net O_2^M production rate at the off-phase temperatures observed. Figure 6.13 shows the temperature distribution of the discharge typical of the on-phase ($t = 40\,\mu$s, fig. 6.13a) and the off-phase ($t = 70\,\mu$s, fig. 6.13b). Temperature distributions for the other timesteps can be found in the appendix. During the off time the temperature is relatively uniform across the discharge, with values ≤ 1 eV everywhere. Temperatures are more variable with position in the on-phase, but are ~ 4 eV for most locations. The calculated rate coefficients are displayed in table 6.2, assuming an off-phase temperature of 1 eV and on-phase temperatures of 4 eV.

	Reaction	Rate Coefficient K ($\mathbf{m^3\,s^{-1}}$) Off-phase (1eV)	On-phase (4eV)
$K(O_2^M)$	$O_2 + e \longrightarrow O_2^M + e$	5.99×10^{-18}	9.10×10^{-16}
K_d	$O_2^M + e \longrightarrow 2\,O + e$	1.19×10^{-16}	1.56×10^{-15}
K_{Mda}	$O_2^M + e \longrightarrow O^- + O$	5.05×10^{-16}	1.47×10^{-16}

Table 6.2: Calculated rate coefficients for O_2^M reactions, assuming on-phase temperatures $\sim 4\,\mathrm{eV}$ and off-phase temperatures $\sim 1\,\mathrm{eV}$.

Using the rate coefficients and densities, a rate equation for the production of O_2^M can be written as:

$$\frac{\delta\, n(O_2^M)}{\delta t} = K(O_2^M) n_{O_2} n_e - K_d n_{O_2^M} n_e - K_{Mda} n_{O_2^M} n_e \tag{6.1}$$

It is possible to roughly estimate $n(O_2^M)$ at the beginning of the off-phase by noticing that this is a first-order linear differential equation of the form

$$\frac{d}{dt} n(O_2^M) = A - B\, n(O_2^M) \tag{6.2}$$

where $A = K(O_2^M) n_{O_2} n_e$ and $B = n_e(K_d + K_{Mda})$, and solving for $n(O_2^M)$. The general solution to this form of equation is:

$$n(O_2^M) = \frac{A}{B} - C\mathrm{e}^{-Bt} \tag{6.3}$$

where C is the constant of integration. Assuming $n(O_2^M) = 0$ at $t = 0$s (i.e. there are no energetic electrons available to excite the gas molecules before the discharge is struck), we have $C = A/B$. Thus, substituting for A and B and simplifying, we have:

$$n(O_2^M) = \frac{K(O_2^M)}{(K_d + K_{Mda})} n_{O_2} \left[1 - \mathrm{e}^{-n_e(K_d + K_{Mda})t}\right] \tag{6.4}$$

Finally, by expanding in Taylor series neglecting higher-order terms, and simplifying, we arrive at a useable equation, namely:

$$n(O_2^M) = K(O_2^M)\, n_{O_2}\, n_e\, t \tag{6.5}$$

Using order-of-magnitude estimates for gas density $n_{O_2} \sim 10^{20}\,\mathrm{m}^{-3}$ and electron density $n_e \approx n_i \sim 10^{16}\,\mathrm{m}^{-3}$, and the rate coefficients given in table 6.2 we can estimate $n(O_2^M)$ as a function of time. Using the values for K given by the on-phase temperatures of $\sim 4\,\mathrm{eV}$, we can estimate the metastable density at the end of the on-phase (i.e. $t = 50\,\mu\mathrm{s}$). This is calculated to be $\sim 5 \times 10^{16}\,\mathrm{m}^{-3}$.

Inputting this value to equation 6.1, and using the off-time rate coefficients, we can estimate $\delta n_{O_2}/\delta t \approx 6 \times 10^{12}\,\mathrm{m}^{-3}\,\mu\mathrm{s}^{-1}$, i.e. small positive growth in the early off-phase. Such a value suggests that the O_2^M density will rise slowly during the off-phase of the cycle, possibly reaching a limit when $K(O_2^M)n_{O_2}n_e = K_d n_{O_2^M} n_e + K_{Mda} n_{O_2^M} n_e$. However, it is difficult to gain a high degree of quantitiative information from this simplified model. The assumed boundary condition may not be valid, and the linear growth implied by equation 6.5 does not accurately represent the true behaviour of the plasma (since it arises from a first order Taylor expansion, an approximation). It is clear, then, that this simplified model, while mathematically sound, may not be physical due to the somewhat baseless assumption that $n_{O_2^M} = 0$ at $t = 0$. That condition may be true for the initial pulse cycle, however the values given above suggest a steady rise of metastable density during the off-phase which would imply a build-up of O_2^M over several cycles. Clearly the quantity of O_2^M will also be affected by interactions with the neutral species O_2, Ar and O, as well as with Ar^+, O^+ and $O_2{}^+$, and is likely to be significantly lower in the late off-time than this model predicts, however it may be better in this case to consider the process more qualitatively, and treat the metastable production rate described above as a guideline only. It is nevertheless clear that the metastable molecules O_2^M will be produced in some quantity, allowing for the O^- production channel via metastables in addition to the production via dissociative attachment of ground-state O_2. Furthermore, It is sufficient to note that a significant quantity of metastable molecules exists in the plasma, therefore enabling the enhanced production of O^- via dissociative attachment in regions where cold electrons are confined (i.e. the trap during the afterglow), as predicted in the previous chapter, and elsewhere [50].

6.3 Conclusions

The time-resolved density distribution of negative ions has been measured successfully in low power circular dc reactive plasmas with fixed 20% oxygen partial pressure. In the on-phase of the discharge, the density distribution is consistent with that observed in steady-state dc. The area of highest O^- density shifts after the transition to the off-phase, until O^- ions start to occupy the magnetic field trap region close to the racetrack area. This occurs on a very rapid timescale ($\sim 10\,\mu$s after the transition), with negative ions remaining in stable concentrations in the trap region throughout the off-phase. The results show moderately electronegative plasma regions in the areas of the plasma that are typically occupied by the substrate during film growth during the on-phase, and in regions within the trap during the off-phase. In the pulsed-dc case, O^- density is not seen to exceed the electron density anywhere in the discharge. It is suggested that this behaviour is a result of negative ions being produced by the dissociation of metastable vibrationally excited O_2^M.

Chapter 7

Spatial and Temporal measurements in DC and Pulsed-DC H_2 Discharges

7.1 Background to the H_2 Experiment

7.1.1 Negative Ion Neutral Beam Sources

In order for global efforts to produce energy with nuclear fusion to succeed, it is necessary to develop neutral beam heating systems capable of delivering high energy deuterium particles into a tokamak plasma. For such particles to bypass the extreme magnetic and electric fields which are used for confinement of the main fusion plasma, these must be neutral deuterium atoms. The most practical method of accelerating these particles to the desired energies (in excess of 1 MeV for the proposed ITER device [4, 6]) is to begin with a source plasma of deuterium and electrostatically accelerate the ions to produce the required energy, and then subsequently neutralise the accelerated ions.

Most neutral beam systems used on tokamaks to-date have utilised positive ion sources; the extracted beams of D^+ are then passed through a chamber of gaseous hydrogen, where they undergo collisions with H_2 particles and become energetic D^0. These are then able to continue into the tokamak. A problem arises as a result of the efficiency of this neutralisation process. At the high energies required by the next generation of fusion devices, the efficiency of the neutralisation interaction ($[D^+] + H_2 \rightarrow [D^0] + {H_2}^+$, where square braces [ ] are used to denote energetic species) drops to zero (Fig. 7.1).

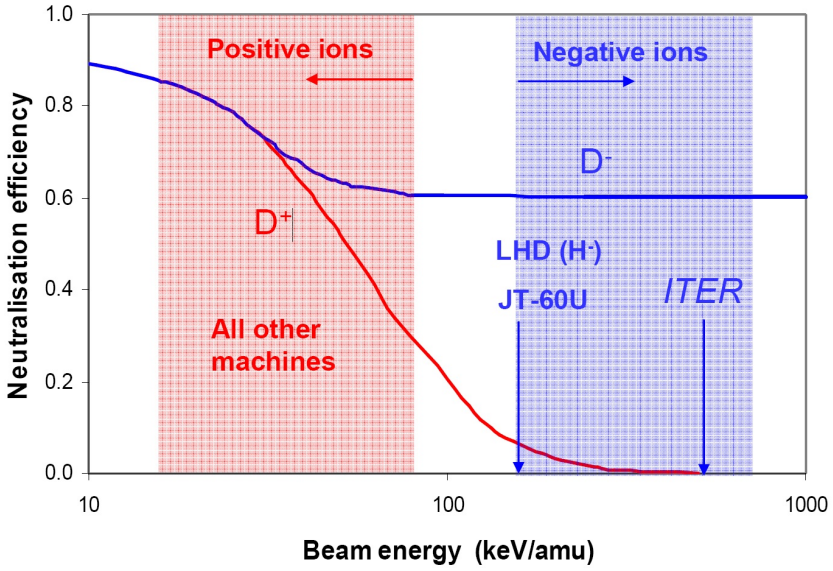

Figure 7.1: Efficiency of neutralisation of D^+ and D^- ions [79]

As a result, it is necessary to utilise beams sourced from negative ion plasmas rather than from positive ion sources. Unfortunately, the electron affinity of hydrogen and its isotopes is relatively modest - only 0.75 eV. As a result of this, it is difficult to create the large concentrations of D^- needed to produce a high-energy, high-current beam. Much of the relevant physics surrounding these problems is discussed further in [5]. In an effort to address some of these issues, an experimental undertaking at CCFE, the Small Negative Ion Facility (SNIF), has been developed. While this plasma source differs in many ways from the magnetron systems being used at the University of Liverpool, there are some broad similarities in size and discharge parameters between the two devices. Further, the ability to perform laser photodetachment experiments to measure the negative ion densities directly does not exist at CCFE. As such, experiments conducted in the magnetron using discharge parameters similar to those of SNIF may provide data that can support the research undertaking at CCFE.

7.1.2 H^- Production Processes

The H^- ion is produced in plasmas predominantly through the dissociative electron attachment reaction. In the hydrogen case, the reaction path is: $e + H_2(v \geq 4) \longrightarrow (H_2^-)^* \longrightarrow H + H^-$ [80], where v denotes the molecular vibrational state of H_2 and * denotes a metastable excited state. The cross

section for this reaction peaks with a value of $K_{da} \approx 3\times10^{-14}\,\mathrm{m^3\,s^{-1}}$ at electron temperatures of 0.4 eV, and declines rapidly with increasing temperature. In most plasmas the electron temperature regularly exceeds this value by a considerable margin, and so the H^- production rate is correspondingly low, particularly in higher power discharges. Further, the presence of the $H_2(v \geq 4)$ precursor molecule is also necessary for this reaction channel. Due to the low efficiency of energy transfer between particles with large mass differences, this is typically produced directly through proton impact ionisation by the reaction $p + H_2(v = 0) \longrightarrow p + H_2(v > 0)$ rather than by electron impact excitation. Elevation of ground-state H_2 to such a high vibrational state, however ($v \geq 4$, since the contribution to dissociative attachment from $v \leq 3$ states is negligible), has a very low cross-section at temperatures typical of the magnetron ($\sigma \approx 3 \times 10^{-21}\,\mathrm{m^2}$ for $T_e = 3\,\mathrm{eV}$, [80]), indicating that production of H^- via this channel is unlikely in the magnetron. Furthermore, the rate coefficients for vibrational excitation K_{ve} are similarly low, with values $K_{ve} \approx 7 \times 10^{-16}\,\mathrm{m^3\,s^{-1}}$ for $T_e = 3\mathrm{eV}$ and $T_i \approx T_{gas} \approx 300K \approx 0.025\,\mathrm{eV}$. However, it has been shown that dissociative electron attachment of vibrationally excited states can occur at significantly higher rates if the reaction proceeds via an intermediate excited Rydberg state. This is discussed in [81], where the authors conclude that at temperatures of approximately 10 eV significant dissociative attachment can occur. These temperatures are still higher than the average temperatures measured in the magnetron, but are sufficiently low that the high energy tail of the electron energy distribution may be able to contribute to H^- production. The rate coefficient for dissociative attachment via this channel is nevertheless considerably lower than for the direct production channel at the temperatures observed (see section 7.4), having values $K_{da} \sim 10^{-20}\,\mathrm{m^3\,s^{-1}}$ at $T_e \sim 3\,\mathrm{eV}$.

The H^- yield in low temperature hydrogen discharges therefore remains relatively low, so various other mechanisms for enhancing the H^- yield in plasmas have been proposed. For instance, it is known that the presence of caesium can enhance the rate of H^- production at the chamber walls [82, 83]. H^- production occurs readily on caesium surfaces due to the close similarity between the caesium work-function and the electron affinity of hydrogen atoms; when a hydrogen atom is close enough to a caesium surface, the electron affinity overlaps with the metal electronic states allowing the electron to tunnel into the atom to form a negative ion. Other low work-function surfaces may exhibit similar behaviour [9], and it is also proposed that other materials such as tungsten [8, 84], tantalum [7, 8, 84] and palladium [85, 86] may achieve a similar role by enhancing the yield of vibrationally excited H_2. This is not clear-cut, however. Furthermore, it is well documented that in

pulsed-DC discharges the negative ion density increases in the off-time of the plasma pulse [87–89]. The relative ease of operating the magnetron plasma in pulsed mode allows simple investigation of this phenomenon, as well as easy switching of the target material to investigate the effect of material choice.

7.2 Preliminary Studies and Plasma Characterisation

The laser power was first optimised by examining the effect of laser energy density on negative ion fraction $\Delta n_-/n_-$ for hydrogen. In this case, the photodetachment cross section $\sigma_{pd} \approx 3 \times 10^{-17}\,\mathrm{m}^2$ for photons of 532 nm [22], giving the theoretical curve plotted in figure 7.2. The experimental curve is also plotted on the same axis, clearly showing the optimum laser power for hydrogen is much lower than that for oxygen, with a value of $\sim 60 - 70\,\mathrm{mW}$. The laser power for the hydrogen experiments was therefore set at 65 mW to ensure that saturation is achieved without overestimating the density of H^-.

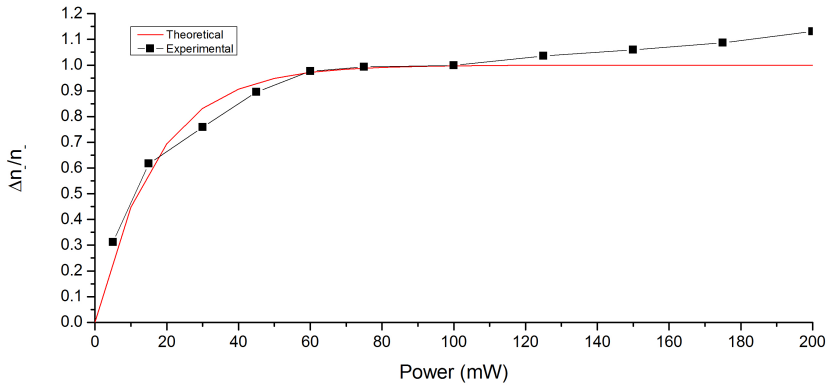

Figure 7.2: A plot of the negative ion fraction ($\Delta n/n_-$) as a function of laser energy density in hydrogen plasmas, for a 532 nm beam and a 300 μm-diameter blocking wire. Discharge power was set to 300 W and total pressure 10 mTorr.

Preliminary experiments to determine the optimum power and pressure for further experimentation were performed, using carbon, copper and tungsten target surfaces. The H^- density against total chamber pressure (mTorr) for a fixed power (300 W) at a single position within the plasma, $(r, z) = (0, 80)$, is shown in figure 7.3 and the corresponding H^+ and e^- densities in figure 7.4.

It can clearly be seen that increasing chamber pressure increases negative ion yield, as it does in the oxygen case. Also of note is the distinction between

the various target materials. It is clear that tungsten and copper yield much higher densities of H^- compared to carbon. Further, within experimental uncertainty there is no significant difference in H^- density between the copper and tungsten cases. It is interesting to see that for the metallic targets, there is no significant difference between n_i and n_e, whereas in the carbon case these two quantities are distinctly different.

The equivalent graphs for varying power at fixed pressure (10mTorr) are shown in figures 7.5 and 7.6. The H^- density remains relatively constant for

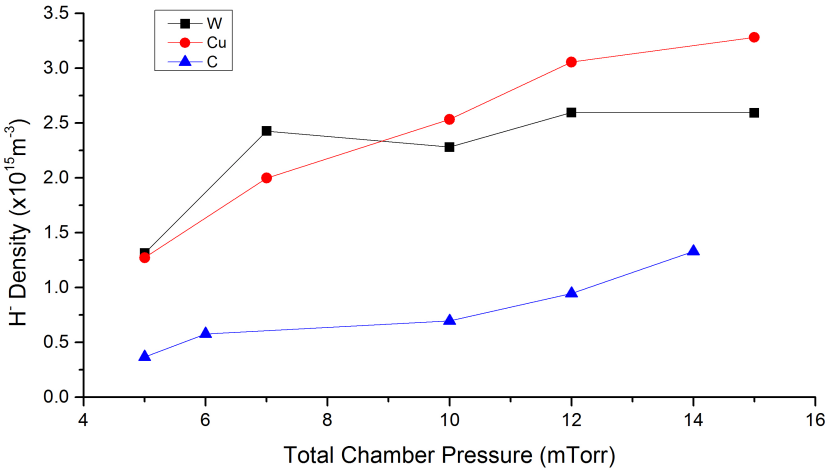

Figure 7.3: Negative hydrogen H^- density, n_- , vs total chamber pressure P_{tot} (mTorr), for Cu, C and W targets.

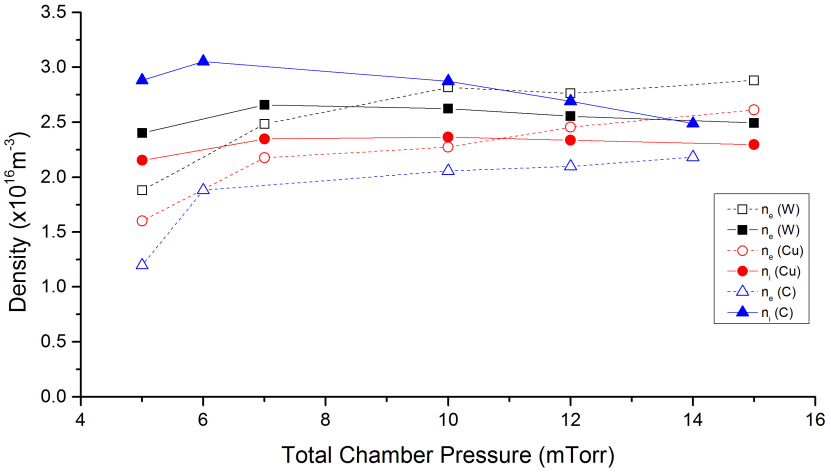

Figure 7.4: Hydrogen ion H^+ density, n_i , and electron density, n_e, vs total chamber pressure P_{tot} (mTorr), for Cu, C and W targets.

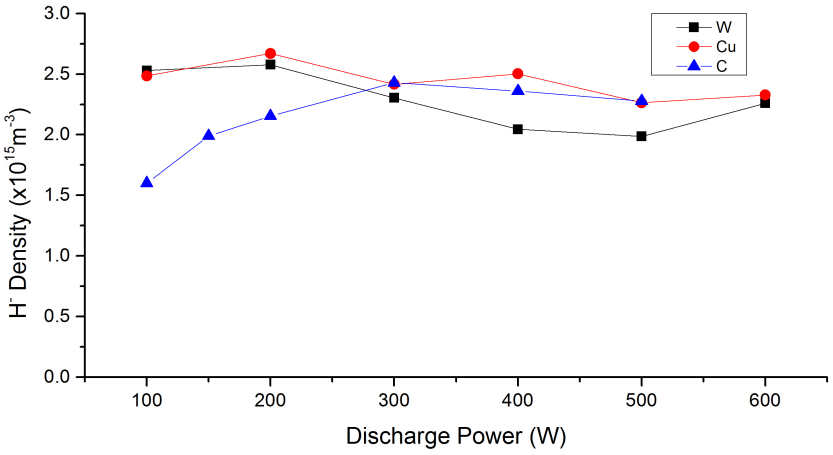

Figure 7.5: Negative hydrogen H^- density, n_- , vs discharge power P (W), for Cu, C and W targets.

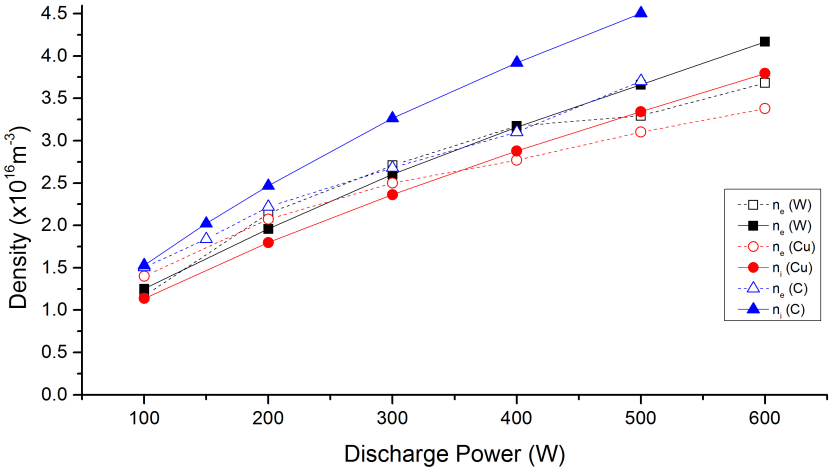

Figure 7.6: Hydrogen ion H^+ density, n_i , and electron density, n_e, vs discharge power, for Cu, C and W targets.

all materials, due to the saturation of production of vibrationally excited molecules. The metallic cases (Cu and W) agree within error, and the carbon case diverges from the metallic values at low powers only. Again, as in the varying pressure case, n_i and n_e agree within error at all powers for all materials, with similar values within error being recorded for both copper and tungsten. The n_i values for carbon deviate from the metallic values at higher powers, however the n_e data remains consistent with the other materials.

Since it there is little variation between the two metallic targets, and tantalum

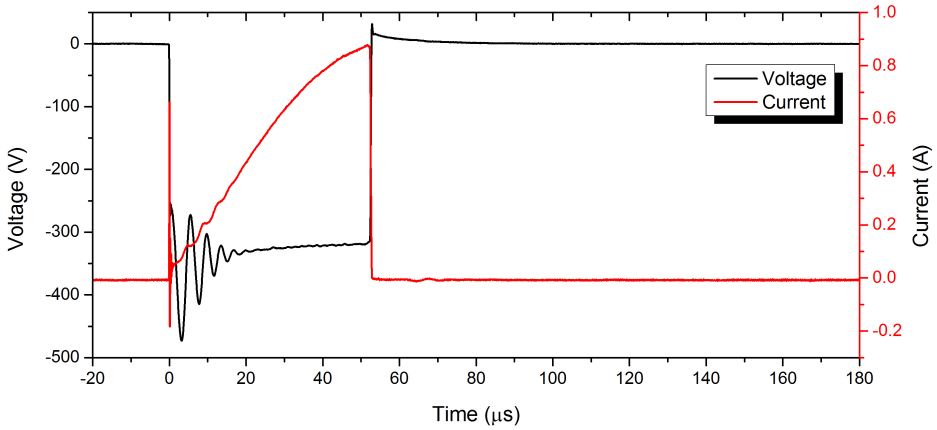

Figure 7.7: Current and voltage profiles for the pulsed discharge. Pulse frequency was set to 5 kHz for a 50 μs on-phase duration, giving a duty cycle of 25%.

and palladium targets such as those discussed in [7, 84, 85] were not available for study, all subsequent work was conducted using the tungsten target. In addition to this constraint, while copper, aluminium and stainless steel are the predominant surface materials inside most negative ion sources, in the case of the magnetron (which is a sputtering device) the sputter rate of copper is significantly greater than that of tungsten. Therefore, tungsten was used in the main hydrogen study to minimise the effects of target erosion and to reduce the proportion of sputtered material present in the discharge. A fixed medium-range average power of 300 W, which is high enough to produce a long-term stable discharge was chosen for subsequent dc work, and pressure of 10 mTorr chosen for its similarity to the design pressures for neutral beam sources and the relatively high H^- density observed.

7.3 Experimental Method

This novel study of hydrogen plasmas was performed following essentially the same method as both the dc and pulsed-dc oxygen experiments, with Langmuir probe characteristics and photodetachment currents being recorded at a fixed DC power and chamber pressure in a pure hydrogen ($>$ 99.9% purity) discharge, and a spatial scan of the discharge performed to produce a 2D spatial distribution. In a neutral beam source plasma, negative ions are predominantly created in a so-called 'expansion region' of the plasma, far from the ionising regions of the discharge where the electron temperature

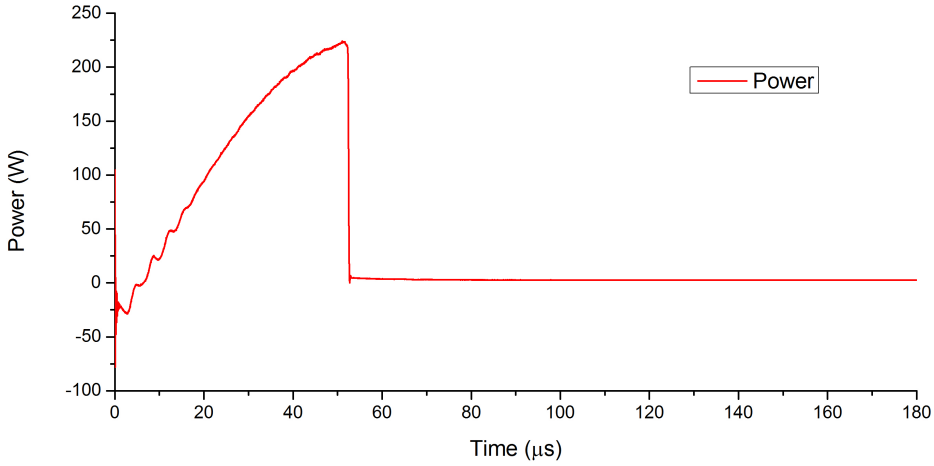

Figure 7.8: Calculated instantaneous power for the pulsed discharge. Peak on-time power was 225 W with an average of $\sim$ 100 W over the cycle.

is lower. For this reason, the measurements were taken at greater distances from the target than in the oxygen experiments, and not inside the magnetic trap region where the low electron affinity of H^- means that any negative ions produced would be extremely short-lived; perhaps even more so than in the oxygen case.

In addition to the spatial distribution, pulsed-dc measurements of the discharge were taken to plot the temporal evolution of H^- density. The time-resolved data were not resolved spatially, however, and instead the data was recorded at the position of highest negative ion density observed in the dc case. The pulsed discharge was operated with a unipolar dc power supply, pulsed using a signal chopper to a frequency of 5 kHz and an on-phase duration of 50 μs, resulting in a 25% duty cycle. The pulse was current-regulated to a fixed average current of 0.25 A, resulting in a peak current of $\sim$ 0.8 A and an average power of $\approx 100W$ (peak power $\approx$ 225 W). Current and voltage profiles are plotted in figure 7.7, and power in figure 7.8.

7.4 Results and Discussion

7.4.1 Time-averaged 2D H^- Distributions

The spatial distributions of ion (H^+) density, electronegativity α and negative (H^-) ion density n_- within the measured region of the discharge are shown in

figures 7.9, 7.10 and 7.11 respectively. These distributions follow the same broad shape and pattern as the oxygen case at mid-range dc pressures, with peak negative ion densities observed off-axis above the trap as usual. Similarly, ion densities are highest on the centreline above the null, decreasing slightly with distance from the target. A peak ion density of $n_i = 3 \times 10^{16}\,\mathrm{m}^{-3}$ is observed on the discharge centreline at a distance $z = 70\,\mathrm{mm}$ from the target, consistent with the position of peak ion density in all previous oxygen experiments. Similarly, the peak negative ion density is seen to be $n_- = 3.3 \times 10^{15}\,\mathrm{m}^{-3}$ at a position $r = 20\,\mathrm{mm}$, $z = 90\,\mathrm{mm}$, again showing consistency with oxygen experiments.

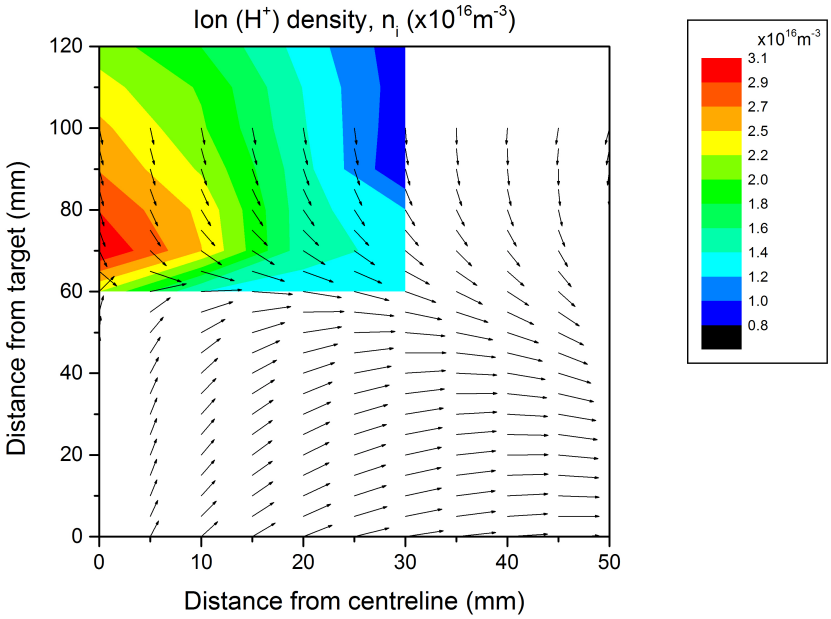

Figure 7.9: The 2D spatial distribution of ion (H^+) density in a 100% H_2 dc discharge. The discharge power was fixed at 300 W and chamber pressure at 10 mTorr.

The photodetached current ratio $\Delta I_{pd}/I_e = \alpha$ follows a similar distribution to the oxygen case, being high in the diffuse region of the discharge far from the target, above the trap and off the centre-line. However, the values in the hydrogen discharge are somewhat lower across the observed region than in the oxygen plasma, with peak $\alpha = 0.5$ being observed at $r = 30\,\mathrm{mm}$, $z = 90\,\mathrm{mm}$. The negative ion densities, therefore, are somewhat lower in hydrogen than oxygen, constituting a fraction typically of around 10-20% of the ion density. In contrast, the oxygen discharge exhibited regions where n_- easily exceeded n_e, giving rise to $\alpha \geq 1.0$ in the same plasma region. It is likely that this is

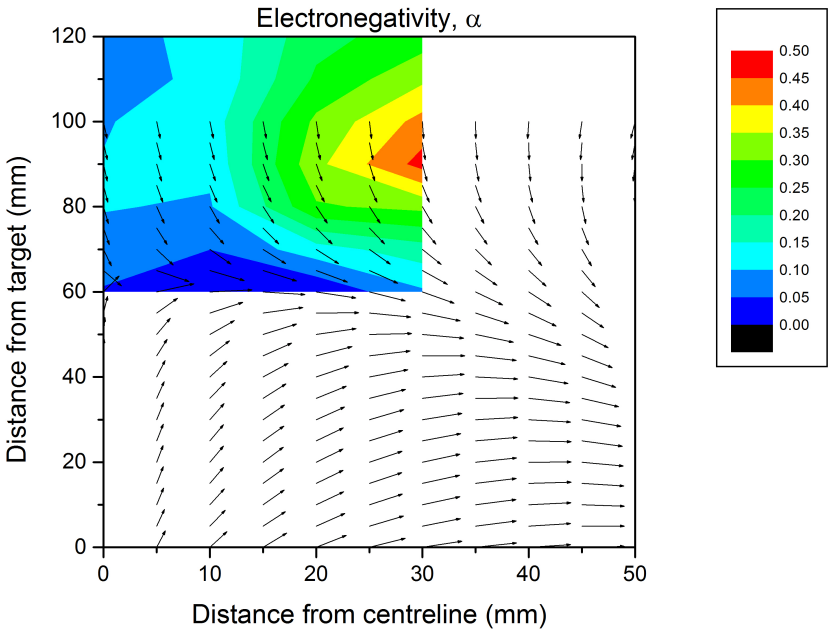

Figure 7.10: The 2D spatial distribution of photodetached current ratio $\Delta I_{pd}/I_e = \alpha$ in a 100% H_2 dc discharge. The discharge power was fixed at 300 W and chamber pressure at 10 mTorr.

simply a case of the lower electron affinity of H^- than O^-, with the surplus electrons being much more readily removed from H^- at similar temperatures. The temperatures observed in this case are typically ~ 2 eV (figure 7.12a), with slightly higher temperatures being observed in the trap region as expected. Interestingly, temperatures in this upper-trap region are approaching the optimum for H^- production by electron impact with vibrationally excited H_2, with values of $\sim 7 - 8$ eV. Plasma potentials (figure 7.12b), although somewhat unreliably obtained from the zero crossing-point of d^2I_e/dV^2 of the Langmuir probe characteristic, show the expected approximately uniform distribution of ~ 3.5 V in the diffuse regions above trap.

Due to the novel nature of this study, there is little directly comparable data available in the literature, however a qualitative understanding of the density distributions may be understood by following a similar procedure to that performed for oxygen in chapter 5. In the hydrogen case we have the production reaction $e + H_2(v \geq 4) \longrightarrow H + H^-$ with rate coefficient $K_{da} = 1 \times 10^{-14}\,m^3\,s^{-1}$ at $T_e = 2$ eV. There are several decay reactions for H^- which may take place in the plasma at the temperatures observed. These reactions with their approximate cross-sections and rate coefficients at $T_e = 2$ eV are shown in table 7.1. Values for all reactions are drawn from the

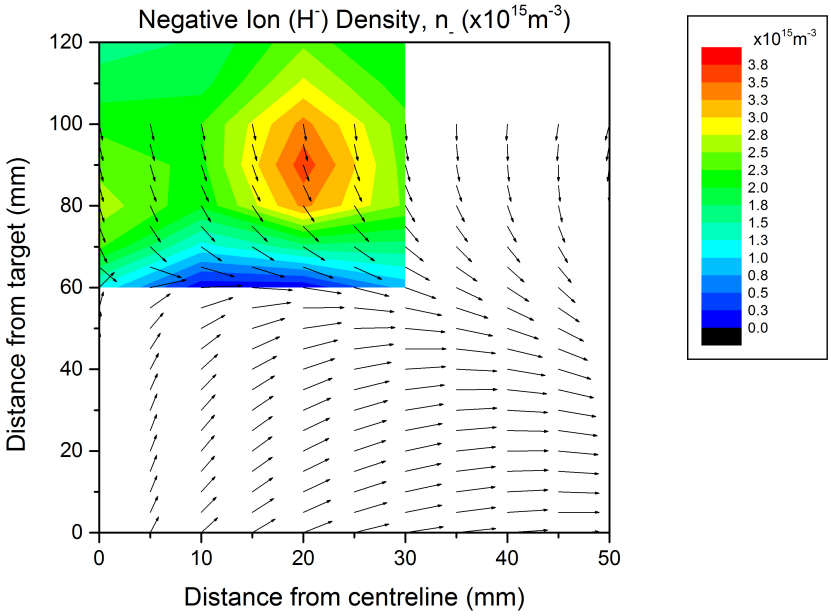

Figure 7.11: The 2D spatial distribution of negative ion (H^-) density n_- in a 100% H_2 dc discharge. The discharge power was fixed at 300 W and chamber pressure at 10 mTorr.

data tabulated and plotted in [80]. The situation can be simplified somewhat, by disregarding reaction 4, since this has both a negligible cross section and rate coefficient in comparison to the charge-exchange reaction (3), and in any case does not affect the total density of H^-. The neutralisation process described by reaction 3 appears from this data to be the dominant decay process for H^-. Electron-impact de-ionisation (reaction 1) may also play a significant role, since although the cross section is a factor of $\sim 100\times$ less than 3, it has a similar rate coefficient.

Since the exact density of neutral H is unknown without recourse to optical spectroscopic analysis (not performed for this plasma), measured values for n_H cannot be used in a rate balance calculation. However, the degree of dissociation of H_2 in inductively-coupled low temperature plasmas has been modelled by Sode *et al.* and was found to be $\sim$1% of the H_2 density [90], which in this plasma discharge would be $\sim 10^{18}\,\mathrm{m}^{-3}$ assuming an ideal neutral gas density of $\sim 10^{19}\,\mathrm{m}^{-3}/\mathrm{mTorr} = 10^{20}\,\mathrm{m}^{-3}$ at 10 mTorr. Similar densities ($2\times10^{18}\,\mathrm{m}^{-3}$) of atomic hydrogen and a similar dissociation fraction of a few percent were also observed in an RF GEC cell by Chérigier [91], suggesting that $10^{18}\,\mathrm{m}^{-3}$ may be a reasonable order-of-magnitude estimate for rate balance in this case. Densities of $H_2(v \geq 4)$ are also unknown in

	Reaction	Rate coefficient K ($\mathrm{m^3\,s^{-1}}$)	Cross-section σ ($\mathrm{m^2}$)
1	$\mathrm{H^- + e \longrightarrow e + H(1\,s) + e}$	7×10^{-14}	1.5×10^{-20}
2	$\mathrm{H^- + H^+ \longrightarrow H^*}(n=2) + \mathrm{H(1\,s)}$	2×10^{-15}	7.0×10^{-20}
3	$\mathrm{H^- + H^+ \longrightarrow H^*}(n=3) + \mathrm{H(1\,s)}$	6×10^{-14}	2.0×10^{-18}
4	$\mathrm{H^- + H(1\,s) \longrightarrow H(1\,s) + H^-(1\,s)}$	3×10^{-17}	1.2×10^{-21}
5	$\mathrm{H^- + H \longrightarrow H + H + e}$	1×10^{-15}	4.0×10^{-20}
6	$\mathrm{H^- + H \longrightarrow H_2 + e}$	2×10^{-15}	8.0×10^{-20}

Table 7.1: Reactions involving $\mathrm{H^-}$, with rate coefficients and cross-sections at $T_e = 2\,\mathrm{eV}$.

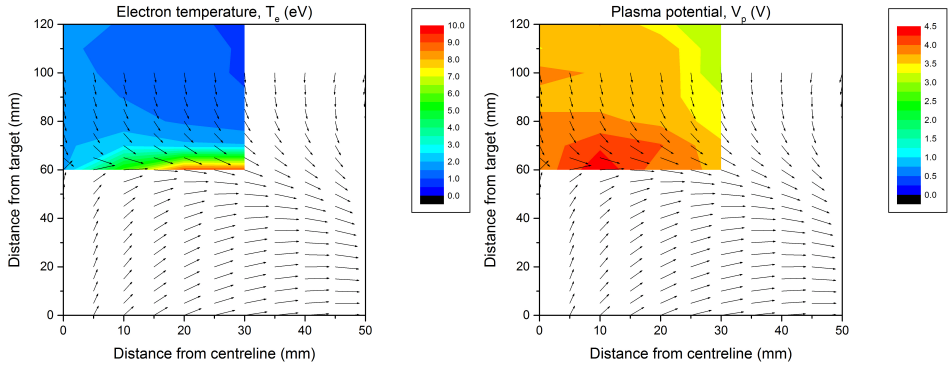

(a) T_e (eV) (b) V_p (V)

Figure 7.12: The spatial distribution of electron temperature T_e and V_p in a hydrogen discharge. Discharge power was 300W and the chamber pressure was 10mTorr.

the magnetron, and experimental measurements in the literature are scarce, however Mosbach *et al.* measured densities of $4 \times 10^{15}\,\mathrm{m^{-3}}$ in a magnetic multipole plasma source [92]. This measurement may be a reasonable estimate for our simple picture given the similarities between the discharge conditions, and lack of suitable alternatives.

A similar rate balance analysis for experimental and calculated $\mathrm{H^-}$ densities in a divertor simulator (MAP-II) was performed by Kajita and Kado [93], where the authors consider only the dominant electron dissociation (reaction 1), mutual neutralisation (reaction 3) and transport loss processes. Following this precedent, our rate balance equation may be simplified. Although the authors of [93] have used a measurement of vibrational states of $\mathrm{H_2}$ obtained

from Fulcher band spectra in their analysis, they unfortunately do not specify the value obtained. Their paper does, however, offer an opportunity to make comparisons with the results of this study. Using the density values as discussed, we can calculate a net production or loss rate for H^-. For production, we have:

$$\frac{dn_-}{dt}_{>0} = K_{da}\, n_e\, n_{H_2(v')} \tag{7.1}$$

and the loss reactions give:

$$\frac{dn_-}{dt}_{<0} = -K_1\, n_e\, n_- - K_3\, n_i\, n_- - \frac{n_-}{\tau} \tag{7.2}$$

where the K_x subscripts correspond to the reaction number labels given in table 7.1 and τ is a confinement time of negative ions given by a characteristic scale length L divided by the drift velocity $v_d = (2e\Delta\phi/m_i)^{1/2}$, as in chapter 5. Assuming a steady-state equilibrium condition (i.e. $dn_-/dt = 0$) to form a rate balance equation, we obtain:

$$\frac{dn_-}{dt} = K_{da}\, n_e\, n_{H_2(v')} - K_1\, n_e\, n_- - K_3\, n_i\, n_- - \frac{n_-}{\tau} = 0 \tag{7.3}$$

Solving for n_-:

$$n_- = \frac{K_{da}\, n_e\, n_{H_2(v')}}{K_1\, n_e + K_3\, n_i + \frac{1}{\tau}} \tag{7.4}$$

Making the assumption $n_e \sim n_i$, this can be simplified slightly, to give:

$$n_- = \frac{K_{da}\, n_i\, n_{H_2(v')}}{n_i(K_1 + K_3) + \frac{1}{\tau}} \tag{7.5}$$

For a characteristic scale length $L \sim 1\,\mathrm{cm}$, we obtain $\tau = L/v_d \sim 0.01/5.5 \times 10^3 \sim 2\,\mu\mathrm{s}$. Using this value, the values for K_x above, and assuming $n_{H_2(v')} \sim 5 \times 10^{15}\,\mathrm{m}^{-3}$ and measured values for n_i, calculated values for n_- can be estimated. At the position of peak negative ion density ($r = 20\,\mathrm{mm}$, $z = 90\,\mathrm{mm}$) $n_i = 1.5 \times 10^{16}\,\mathrm{m}^{-3}$, giving $n_- = 1.5 \times 10^{12}\,\mathrm{m}^{-3}$, a significant underestimate of the measured value. If the drift velocity is substituted for a diffusion term, $D = 1/3\lambda v_{th}$, where $\lambda \sim 0.05\,\mathrm{m}$ is the mean free path (calculated as in section 3.1 using the hydrogen Van der Waals

radius of 120 pm) and $v_{th} = (kT_i/m_i)^{1/2} = 485\,\mathrm{m\,s^{-1}}$ the ion thermal velocity for $T_i \approx T_{gas} \sim 0.025\,\mathrm{eV}$, we obtain $\tau \sim 100\,\mu\mathrm{s}$. This yields $n_- = 1.7 \times 10^{14}\,\mathrm{m^{-3}}$, underestimating n_- by a factor of 10^2, perhaps suggesting an underestimate of $n_{H_2(v')}$ here. Summing the densities of all vibrationally excited states for $v \geq 4$ given by Mosbach [92] increases the estimate for $n_{H_2(v')}$ to $1.3 \times 10^{16}\,\mathrm{m^{-3}}$, which results in a calculated value for $n_- \sim 2 \times 10^{14}\,\mathrm{m^{-3}}$, thus reducing the underestimate of n_- to a factor of ~ 10 at the peak position. The calculated value for n_- does match closely with measured values in the upper trap region, however, although this could be coincidental. The discrepancy elsewhere cannot be accounted for by the assumption $n_e \sim n_i$, as this actually leads to an overestimation of n_- by a factor ~ 1.1, nor does the exclusion of some of the loss mechanisms from the rate balance, which would serve to reduce the calculated value further. This leads to the possible conclusion that some process not accounted for may be increasing the negative ion yield. This could indicate an effect of the tungsten target increasing the density of vibrational excited states in the bulk, for example radiative desorption as suggested in [8], however this is impossible to confirm conclusively from the available data. Alternatively the density of vibrational states $n_{H_2(v')}$ may be dependent upon position within the discharge, although again without detailed spatially-resolved measurements using Fulcher band spectroscopy, this may be difficult to confirm.

7.4.2 Time-resolved H^- Densities in Pulsed-dc

Time-resolved ion density, electronegativity and negative ion density measurements were performed in the hydrogen plasma, using a discharge pulse of the same frequency, power and duty cycle as that used in chapter 6, namely 5 kHz, 100 W average power and 25% duty cycle. Pressure was also kept at 10 mTorr, so that the only difference between the two experiments was the working gas. The time-resolved spatial distributions were not measured for hydrogen, however, with measurements being taken at the position of peak H^- concentration observed in the dc case. In this experiment, electron densities were also estimated by the 'conventional' method (i.e. from the current at the plasma potential $I_e = {}^1\!/_4\, A_p\, e\, n_e\, v_{th}$) for comparison with n_i, since at this particular position within the discharge the zero-crossing point of d^2I_e/dV^2 is distinct and easily identifiable at all timesteps. The uncertainty in V_p is therefore somewhat lower than usual for this method.

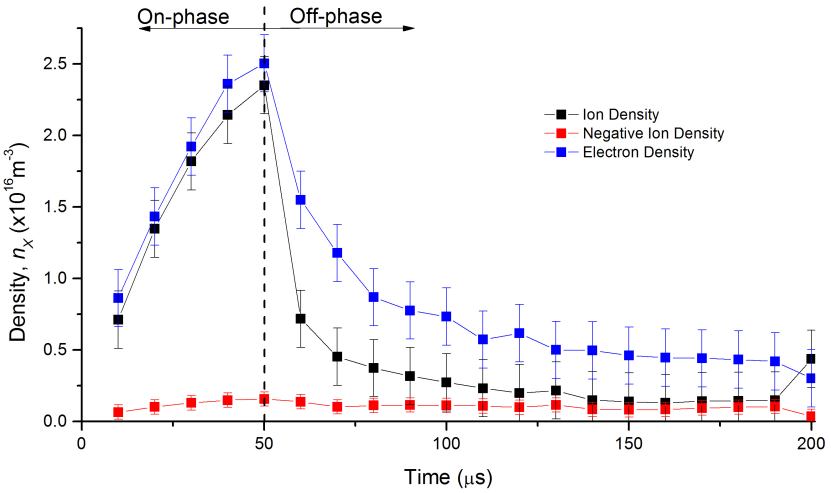

Figure 7.13: The temporal evolution of densities of electrons n_e, ions n_i and negative ions (H^-) n_- in a pulsed-dc H_2 discharge. The plasma was operated at 10mTorr and a fixed average power of 100W and a 25% duty cycle.

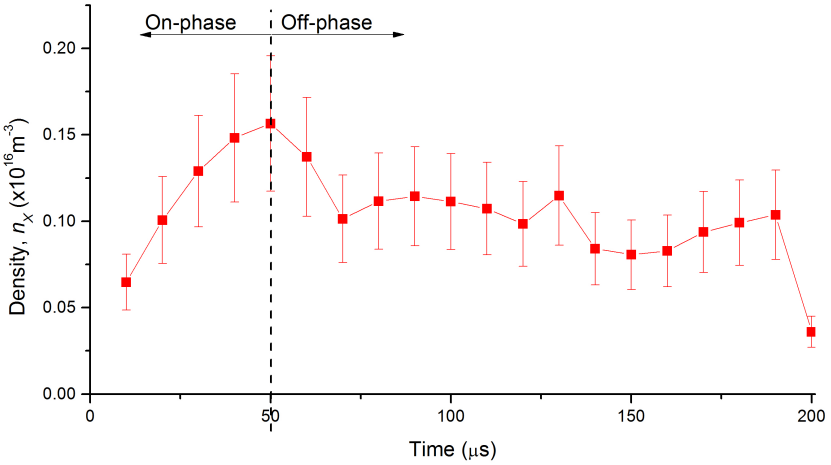

Figure 7.14: The temporal evolution of negative ion density (H^-) n_- in a pulsed-dc H_2 discharge. The plasma was operated at 10 mTorr and a fixed average power of 100 W and a 25% duty cycle.

Figure 7.13 shows the three densities (ion n_i, electron n_e, and negative ion n_-) plotted as a function of time for this position, and figure 7.14 shows n_- on a larger scale. Ion and electron densities behave as expected, with values rising sharply during the on-phase, peaking at $n \approx 2 \times 10^{16}\,\mathrm{m}^{-3}$ at the end of the on-phase, before rapidly declining in the early off-phase. The measurements agree closely within error during the on-phase, but diverge immediately in the

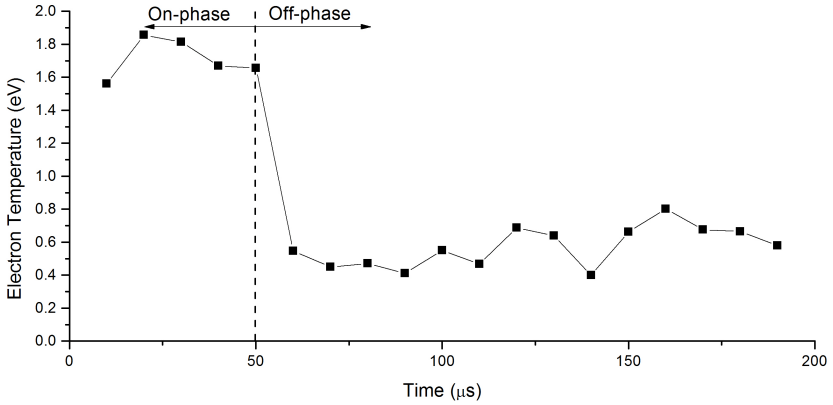

Figure 7.15: The temporal evolution of electron temperature T_e in a pulsed-dc H_2 discharge. The plasma was operated at 10 mTorr and a fixed average power of 100 W and a 25% duty cycle.

off-phase, only showing general agreement in the late off-time. However, this divergence is likely to be simply a result of the somewhat unreliable method of calculating n_e. Negative ion densities are seen to be a negligible fraction of the total during the on-phase ($n_-/n_e \sim 0.04 - 0.1$), and do not rise in the off-time as might be expected from previous studies of H^- in time-varying discharges [88]. As is clear from figure 7.14, n_- varies little over the pulse with only a small rise in the on-phase, and no significant difference within error during the off-phase. The behaviour observed here may be explained by considering the balance between production and loss mechanisms of vibrationally excited H_2 and H^-. Since production of vibrationally excited H_2 requires electron temperatures much higher than those observed here, it seems likely that any $H_2(v \geq 4)$ produced will be easily dominated by the diffusive and collisional loss mechanisms. While in the on-phase the high energy tail of the electron energy distribution may be sufficient to generate some quantity of $H_2(v \geq 4)$, in the off-phase this is unlikely. Therefore, any growth of H^- density in the off-phase would require dissociative attachment of vibrational H_2 produced during the on-phase. This suggests that the loss mechanisms for vibrational H_2 may be the limiting reactions in the volume production of H^-.

An attempt to understand quantitatively the processes here can be made (following the procedure used in the previous chapter) to estimate n_- as a function of t by solving the differential equation 7.3 where $dn_-/dt \neq 0$ and assuming $n_- = 0$ at $t = 0$ as before. This yields the awkward expression:

$$n_- = \frac{K_{da}\, n_i\, n_{H_2(v')}}{n_i\,(K_1 + K_3) + \frac{1}{\tau}} - \frac{K_{da}\, n_i\, n_{H_2(v')}}{n_i\,(K_1 + K_3) + \frac{1}{\tau}} \exp\left(-t\,\left(n_i\,(K_1 + K_3) + \frac{1}{\tau}\right)\right) \tag{7.6}$$

which (by Taylor expansion) again reduces to the somewhat simpler:

$$n_- = K_{da}\, n_i\, n_{H_2(v')}\, t \tag{7.7}$$

Using the previous values $K_{da} = 1 \times 10^{-14}\,\mathrm{m^3\,s^{-1}}$ and $n_{H_2(v')} = 1.3 \times 10^{16}\,\mathrm{m^{-3}}$, and an ion density representative of on-phase values $n_i = 1.5 \times 10^{16}\,\mathrm{m^{-3}}$ and time $t = 50\,\mu\mathrm{s}$ (i.e. the beginning of the off-phase), this predicts $n_- = 1.0 \times 10^{14}\,\mathrm{m^{-3}}$, again a factor of ~ 10 too low although it is a value at least consistent with the dc equilibrium prediction. Temperatures in the discharge are shown in figure 7.15. While off-phase temperatures are close to the optimal temperature of 0.4 eV for dissociative attachment of $H_2(v \geq 4)$, given that the on-phase temperatures do not exceed 2 eV at this position, the quantity of vibrationally excited H_2 is likely to be negligible, leading to a low density of H^- being observed. Comparing the peak H^- concentration to the dc-peak, however, shows a factor of 2 difference (dc peak $n_- \approx 3 \times 10^{15}\,\mathrm{m^{-3}}$ c.f. pulsed-dc peak $n_- \approx 1.5 \times 10^{15}\,\mathrm{m^{-3}}$), indicating that the loss mechanisms of H^- which dominate over the production mechanism are balanced somewhat by a sustained discharge. Operating the magnetron in pulsed mode, at least at this position, does not appear to exhibit the temporal filter behaviour as observed elsewhere [87–89].

7.5 Conclusions

The densities of negative hydrogen H^- ions within the discharge have been successfully measured using laser photo-detachment. The densities have been spatially mapped in a steady-state dc discharge, and resolved temporally at a fixed position in pulsed dc. The results show a spatial distribution which closely mirrors that observed in the oxygen case, suggesting a universal pattern of negative ion distribution within the magnetron that is independent of the discharge gas. Electronegativities in the hydrogen case are low, with a peak α of 0.5 being observed in the region of highest H^- concentration. An analysis of the production and loss mechanisms using a rate balance method underestimates the negative ion density by at least an order of magnitude. This indicates the possibility of additional H^- production processes taking

place in the discharge in addition to the known dissociative attachment process. In pulsed-dc, no significant change in H^- density is observed throughout the pulse cycle, with a small rise during the on-phase being observed, followed by a return to the original density levels during the off-phase. The effect of the 'temporal filter' was not observed at the position studied, however spatial mapping of the temporal evolution may reveal a spatial dependence, as observed for oxygen, so the possibility of enhanced H^- production during the off-phase at other locations in the plasma cannot be precluded.

Chapter 8

Conclusions

8.1 Summary of Research Outcomes

The magnetron has been operated under a wide range of discharge conditions in oxygen/argon and hydrogen atmosphers at various powers and pressures. The laser-photodetachment technique in conjunction with Langmuir probing has been successfully used to measure the densities of negative ions in these discharges, with supporting ion density, plasma electronegativity, electron temperature and plasma potential information also recorded. 2D-spatial distributions of negative ion density, ion density, electronegativity and temperature have been mapped out for the axial plane of the circular discharge, with the accessible region of the plasma extending from a distance of 30mm to 120mm away from the target surface, and extending radially 30mm from the axis in both directions. Results from spatial distribution plotting show a strong positional dependence of the negative ion density, which follows the same trend in dc and pulsed-dc Ar/O_2 mixtures, and in H_2 discharges suggesting that the distribution of negative ions is independent of the discharge atmosphere and operating conditions, however the O^- distribution is seen to vary with total discharge pressure (chapter 5).

Densities of O^- in Ar/O_2 mixtures and H^- in hydrogen discharges are concentrated in a region of the discharge off the centreline (magnetic axis) and away from the target above the trap. This formation results in an 'ring' structure around the magnetic axis of the circular magnetron if rotational symmetry is assumed. One possible explanation for the drop in negative ion density along the centreline is the magnetic mirror effect at the null position. This leads to a flow of electrons away from the target with a higher velocity

parallel to the magnetic axis than at other regions of the plasma, thus enhancing the dissociation of O^- in those locations. In general, negative ions are observed to be more concentrated in the locations where positive ion densities are low. This is true across all discharge conditions observed in this study, and in both gas types.

In the oxygen case, negative ion densities are observed to be typically $\sim 1 \times 10^{16}\,\mathrm{m}^{-3}$ increasing towards $1 \times 10^{17}\,\mathrm{m}^{-3}$ at positions of peak density, consistent with most plasmas of this temperature and pressure range. Negative ions are seen to appear in densities $1{\times}10^{14}\,\mathrm{m}^{-3} \leq n_- \leq 1{\times}10^{16}\,\mathrm{m}^{-3}$ depending on position and discharge conditions. Measurements of electronegativity α suggest regions where the negative ion density exceeds that for ions, with $\alpha \sim 1.5$ being recorded in the diffuse off-axis region of the dc O_2 discharge. This corresponds to a region of the discharge where a substrate might sit in industrial discharges, which in certain cases may affect the quality of a growing film by altering the Bohm criterion of the discharge at those locations thereby influencing the ion flux to the substrate. The extent to which this occurs may depend on discharge conditions, as the modification to the Bohm criterion is significant only for electronegativities ≥ 2 [44].

Pulsed-dc oxygen discharges show the same distribution of negative ions within the discharge, with densities of O^- peaking in the off-axis region above the trap during the on-phase. During the off-phase, the concentration of O^- here is seen to decline, however a sharp rise in n_- is observed within the trap region of the discharge which is sustained throughout the afterglow. Densities of O^- are negligibly small in this area during the on-phase. This can be explained by the presence of metastable vibrationally excited oxygen molecules O_2^M within the discharge, which have a high dissociative attachment cross-section at temperatures ~ 0.5eV similar to those seen in the off-phase of the discharge. During the on-phase of the discharge the electron temperatures in the trap are too high for O^- to be readily produced, however the temperature drops rapidly on a timescale $\leq 10\mu$s after the discharge pulse allowing the O^- formation to increase drastically during that time. The tendency of n_- to remain relatively stable in this region for the duration of the off-phase indicates a balance between production and loss mechanisms, suggesting that electrons trapped within the magnetic field may play a role. This is supported by the observation that ion density and therefore (assuming $n_i \approx n_e$) electron density is seen to decline more slowly within the trap than elsewhere in the discharge. It has been noticed by other researchers that negative ion densities produced via the metastable excited state channel is sensitive to the discharge power, an observation consistent with the data collected here, when compared with previous experiments in the same rig which produced different time-resolved

results [50, 51].

In hydrogen dc discharges, the same distribution pattern is observed as in the dc oxygen at similar pressure for negative ion density and electronegativity. Ion density also peaks on the magnetic axis above the null, with values in the range $1 - 4 \times 10^{16}\,\mathrm{m}^{-3}$. Electronegativity peaks off-axis, above the trap region, however values reach a maximum ~ 0.5, much less than in the oxygen case, indicating a strongly electropositive plasma in most locations. Negative ion density does not exceed the ion/electron density anywhere in the discharge, however peak values of $n_- \sim 0.1\,n_i \approx 4 \times 10^{15}\,\mathrm{m}^{-3}$ are achieved in the annular region. H^- is known to be readily produced by dissociative electron attachment of vibrationally excited H_2 molecules for vibrational states $v \geq 4$. Rate balance for the steady state dc plasma, equating production and loss mechanisms, underestimates the negative ion density by a factor of 10-100, subject to the assumed value of $n_{H_2(v')}$. This could be a result of additional production processes not accounted for here, such as the enhanced production of $H_2(v \geq 4)$ at the tungsten target surface, however without direct experimental measurements of $n_{H_2(v')}$ this cannot be conclusively determined in the magnetron.

In pulsed-dc hydrogen discharges, n_- is seen to rise slightly from initial values $\sim 0.5 \times 10^{15}\,\mathrm{m}^{-3}$ up to $1.5 \times 10^{15}\,\mathrm{m}^{-3}$ in the on-phase, declining slowly throughout the off-phase. The values of n_- are $\sim 4\%$ of the peak on-phase plasma density, reaching a maximum of 6% of n_i at the end of the on-phase. H^- densities have been seen to rise in the off-phase of pulsed discharges in other experiments, a phenomenon which occurs due to the drop in T_e in the off-phase to values which closely match the optimal temperature for dissociative attachment of $H_2(v \geq 4)$, however this was not observed in this plasma. The on-phase temperatures at the position under observation does not exceed 2eV, a temperature too low for significant production of vibrationally excited states, which might explain the low negative ion fraction observed in this case.

8.2 Scope for Future Work

A number of key trends and patterns for negative ion behaviour in the magnetron have been observed, however there are avenues for further work. In the oxygen case, it would be interesting to extend the study of the distribution to additional discharge powers and O_2 partial pressures, to give a more complete picture of the distribution behaviour. The discharge parameters

chosen in this study corresponded to those which yielded highest densities of n_- in previous experiments, except for total pressure which was varied. Extending the field of view of the discharge, to allow mapping of the density over a larger area would also provide additional insights. Operating in pulsed mode enables observation of the temporal evolution of the density. It may prove fruitful to examine the effect of average power on the distribution, as it is strongly implied in the work of Dodd [51], You [50] and Panda [48] (supported to an extent by the work presented here) that the off-phase behaviour may change markedly for otherwise similar plasmas.

In addition to these simple measures of expanding the "parameter space" of the measurements, introduction of a substrate typical of those used in sputtering applications into the plasma (such as a silicon wafer) would undoubtedly alter the plasma behaviour. As such, further investigation of the plasma with the substrate present could offer some different insights into the negative ion distribution, as well as production, transport and loss mechanisms. Furthermore, examination of films grown on such a substrate under different negative ion conditions to determine the effect of local O^- density on the film properties (such as reflectivity, refractive index, carrier concentration, Hall mobility etc.) may provide insights that would allow further optimisation and improvement of the reactive sputtering method of film growth.

The hydrogen study could be made more applicable to neutral beam applications by performing experiments in RF discharges similar to those in a neutral beam source. In order to gain greater insights into the behaviour of H^- and $H_2(v \geq 4)$ in such discharges, the density of vibrational states could be measured using Fulcher band emission spectra. This would allow a more rigorous interpretation of the rate balance and give stronger evidence to indicate whether or not the tungsten surfaces play a role in volumetric H^- production. The natural extension to the pulsing experiment is to map the temporal evolution of the spatial distribution, as was done for the oxygen case. If similar behaviour is observed, this would suggest a tendency of universal patterns of behaviour across discharges of various types, and perhaps make the results more applicable to a neutral beam source plasma.

Bibliography

[1]W. D. Gill and E. Kay, "Efficient low pressure sputtering in a large inverted magnetron suitable for film synthesis", Review of Scientific Instruments **36**, 277–282 (1965).

[2]R. K. Waits, "Planar magnetron sputtering", Journal of Vacuum Science & Technology **15**, 179–187 (1978).

[3]B. Window and N. Savvides, "Charged particle fluxes from planar magnetron sputtering sources", Journal of Vacuum Science & Technology A **4**, 196–202 (1986).

[4]B. Schunke et al., "Status of the negative ion based heating and diagnostic neutral beams for ITER", AIP Conference Proceedings **1097**, 480–490 (2009).

[5]M Bacal, "Physics aspects of negative ion sources", Nuclear Fusion **46**, S250–S259 (2006).

[6]L. Grisham et al., "Recent improvements to the ITER neutral beam system design", Fusion Engineering and Design **87**, 1805–1815 (2012).

[7]M. Bacal et al., "Contribution of wall material to the vibrational excitation and negative ion formation in hydrogen negative ion sources (invited)", Review of Scientific Instruments **75**, 1699 (2004).

[8]R. I. Hall et al., "Vibrational excitation of hydrogen via recombinative desorption of atomic hydrogen gas on a metal surface", Phys. Rev. Lett. **60**, 337–340 (1988).

[9]J. R. Hiskes and A. M. Karo, "Recombination and dissociation of H_2^+ and H_3^+ ions on surfaces to form H_2(v"): negative-ion formation on low-work-function surfaces", Journal of Applied Physics **67**, 6621 (1990).

[10]J. W. Bradley and T Welzel, "Physics and phenomena in pulsed magnetrons: an overview", Journal of Physics D: Applied Physics **42**, 093001 (2009).

[11]R. Dodd et al., "Negative ion density measurements in reactive magnetron sputtering", Plasma Processes and Polymers **6**, S615–S619 (2009).

[12]M. Macias-Montero et al., "Influence of plasma-generated negative oxygen ion impingement on magnetron sputtered amorphous SiO_2 thin films during

growth at low temperatures", Journal of Applied Physics **111**, 054312 (2012).
[13]H. C. Nguyen et al., "The mechanisms of negative oxygen ion formation from Al-doped ZnO target and the improvements in electrical and optical properties of thin films using off-axis dc magnetron sputtering at low temperature", Semiconductor Science and Technology **26**, 105022 (2011).
[14]J. M. Grace, "Effect of oxidant on resputtering of Bi from Bi-Sr-Ca-Cu-O films", Journal of Vacuum Science & Technology A: Vacuum, Surfaces, and Films **10**, 1600 (1992).
[15]D. J. Kester and R. Messier, "Macro-effects of resputtering due to negative ion bombardment of growing thin films", Journal of Materials Research **8**, 1928–1937 (1993).
[16]P. D. Rack et al., "Negative ion resputtering in $Ta_2Zn_3O_8$ thin films", Journal of Vacuum Science & Technology A: Vacuum, Surfaces, and Films **17**, 2805 (1999).
[17]T. I. Selinder et al., "Resputtering effects on the stoichiometry of $YBa_2Cu_3O_x$ thin films", Journal of Applied Physics **69**, 390 (1991).
[18]S. Kajita et al., "Application of eclipse laser photodetachment technique to electron sheath thickness and collection region measurements", Phys. Rev. E **70**, 066403 (2004).
[19]J. L. Hall and M. W. Siegel, "Angular dependence of the laser photodetachment of the negative ions of carbon, oxygen, and hydrogen", The Journal of Chemical Physics **48**, 943–945 (1968).
[20]L. Tonks and I. Langmuir, "A general theory of the plasma of an arc", Phys. Rev. **34**, 876–922 (1929).
[21]H. M. Mott-Smith and I. Langmuir, "The theory of collectors in gaseous discharges", Phys. Rev. **28**, 727–763 (1926).
[22]M. Bacal, "Photodetachment diagnostic techniques for measuring negative ion densities and temperatures in plasmas", Review of Scientific Instruments **71**, 3981–4006 (2000).
[23]S. Kajita et al., "Effect of probe surface ablation on laser photodetachment signals", Contributions to Plasma Physics **44**, 607–612 (2004).
[24]S. Kajita, S. Kado, and S. Tanaka, "Eclipse laser photodetachment method for avoiding probe surface ablation in negative ion measurement", Plasma Sources Science and Technology **14**, 566–575 (2005).
[25]R Dodd et al., "Negative ion density measurements in a reactive dc magnetron using the eclipse photodetachment method", Plasma Sources Science and Technology **19**, 015021 (2010).
[26]S. Scribbins, M. Bowes, and J. W. Bradley, "The spatial distribution of negative oxygen ion densities in a dc reactive magnetron discharge", Journal of Physics D: Applied Physics **46**, 045203 (2013).

[27]M. A. Lieberman and A. J. Lichtenberg, *Principles of Plasma Discharges and Materials Processing* (Wiley New York, 2005).
[28]D. Depla and S. Mahieu, *Springer Series in Materials Science*, Vol. 109 (Springer, 2008).
[29]S. Konstantinidis and R. Snyders, "Reactive ionized physical vapor deposition of thin films", The European Physical Journal Applied Physics **56**, 24002 (2011).
[30]I. Safi, "Recent aspects concerning DC reactive magnetron sputtering of thin films: a review", Surface and Coatings Technology **127**, 203–218 (2000).
[31]S. Schiller et al., "Reactive D.C. sputtering with the magnetron-plasmatron for tantalum pentoxide and titanium dioxide films", Thin Solid Films **63**, 369–375 (1979).
[32]J. B. Webb, "Transparent and highly conductive films of ZnO prepared by rf reactive magnetron sputtering", Applied Physics Letters **39**, 640 (1981).
[33]J. Bradley et al., "Time-resolved langmuir probe measurements at the substrate position in a pulsed mid-frequency DC magnetron plasma", Surface and Coatings Technology **135**, 221–228 (2001).
[34]A. Belkind et al., "Mid-frequency reactive sputtering of dielectrics: Al_2O_3", Surface and Coatings Technology **174175**, 88–93 (2003).
[35]S. Mráz and J. M. Schneider, "Influence of the plasma chemistry on the composition of ZrO_x and NbO_x thin films deposited by reactive magnetron sputtering", Plasma Chemistry and Plasma Processing **26**, 197–203 (2006).
[36]S. Mráz and J. M. Schneider, "Energy distribution of O^- ions during reactive magnetron sputtering", Applied Physics Letters **89**, 051502 (2006).
[37]S. Mráz and J. M. Schneider, "Influence of the negative oxygen ions on the structure evolution of transition metal oxide thin films", Journal of Applied Physics **100**, 023503 (2006).
[38]S. Mahieu and D. Depla, "Correlation between electron and negative O^- ion emission during reactive sputtering of oxides", Applied Physics Letters **90**, 121117 (2007).
[39]S. Mahieu et al., "Modeling the flux of high energy negative ions during reactive magnetron sputtering", Journal of Applied Physics **106**, 093302 (2009).
[40]D. Depla et al., "Hysteresis behavior during reactive magnetron sputtering of Al_2O_3 using a rotating cylindrical magnetron", Journal of Vacuum Science & Technology A: Vacuum, Surfaces, and Films **24**, 934 (2006).
[41]K. Ellmer and T. Welzel, "Reactive magnetron sputtering of transparent conductive oxide thin films: role of energetic particle (ion) bombardment", Journal of Materials Research **27**, 765–779 (2012).

[42]L. W. Rieth and P. H. Holloway, "Influence of negative ion resputtering on ZnO:Al thin films", Journal of Vacuum Science & Technology A: Vacuum, Surfaces, and Films **22**, 20 (2004).
[43]Y. Cai et al., "Influence of negative ion resputtering on Al-doped ZnO thin films prepared by mid-frequency magnetron sputtering", Applied Surface Science **256**, 1694–1697 (2010).
[44]N. S. J. Braithwaite and J. E. Allen, "Boundaries and probes in electronegative plasmas", J. Phys. D: Appl. Phys. **21**, 1733 (1988).
[45]E. Stoffels, "Negative ions in a CCl_2F_2 radio frequency discharge", Journal of Vacuum Science & Technology A: Vacuum, Surfaces, and Films **13**, 2051 (1995).
[46]E. Stoffels et al., "Negative ions in a radio-frequency oxygen plasma", Phys. Rev. E **51**, 2425–2435 (1995).
[47]U. Fantz et al., "Plasma diagnostic tools for optimizing negative hydrogen ion sources", Review of Scientific Instruments **77**, 03A516 (2006).
[48]S. Panda, D. J. Economou, and M. Meyyappan, "Effect of metastable oxygen molecules in high density power-modulated oxygen discharges", Journal of Applied Physics **87**, 8323 (2000).
[49]S. D. You et al., "A study of the plasma electronegativity in an argon-oxygen pulsed-dc sputter magnetron", Journal of Physics D: Applied Physics **43**, 505205 (2010).
[50]S. You et al., "The temporal evolution of the negative ion density in a low duty cycle pulsed reactive magnetron discharge", Surface and Coatings Technology **205**, S378–S380 (2011).
[51]R. Dodd, S. You, and J. W. Bradley, "O^- density measurements in the pulsed-DC reactive magnetron sputtering of titanium", Thin Solid Films **519**, 1705–1711 (2010).
[52]J. W. Bradley et al., "Resonance hairpin and langmuir probe-assisted laser photodetachment measurements of the negative ion density in a pulsed dc magnetron discharge", Journal of Vacuum Science & Technology A: Vacuum, Surfaces, and Films **29**, 031305 (2011).
[53]J. A. Wagner and H.-M. Katsch, "Negative oxygen ions in a pulsed RF-discharge with inductive coupling in mixtures of noble gases and oxygen", Plasma Sources Science and Technology **15**, 156–169 (2006).
[54]V. Vancoppenolle et al., "Glow discharge mass spectrometry study of the deposition of tio2 thin films by direct current reactive magnetron sputtering of a ti target", Journal of Vacuum Science & Technology A **17**, 3317–3321 (1999).
[55]V. Straňák et al., "Study of electronegative Ar/O_2 discharge by means of langmuir probe", Contributions to Plasma Physics **48**, 503–508 (2008).

[56]D. Hayashi and K. Kadota, "Efficient production of O^- by dissociative attachment of slow electrons to highly excited metastable oxygen molecules", Japanese Journal of Applied Physics **38**, 225 (1999).
[57]F. F. Chen, "Langmuir probes in RF plasma: surprising validity of OML theory", Plasma Sources Science and Technology **18**, 035012 (2009).
[58]J. L. Hall, E. J. Robinson, and L. M. Branscomb, "Laser double-quantum photodetachment of I^-", Phys. Rev. Lett. **14**, 1013–1016 (1965).
[59]B Brehm, M. Gusinow, and J. Hall, "Electron affinity of helium via laser photodetachment of its negative ion", Physical Review Letters **19**, 737 (1967).
[60]R Cellota et al., "Electron affinity of O_2 by laser photodetachment", Bulletin of the American Physical Society **16**, 212 (1971).
[61]R. J. Celotta, R. A. Bennett, and J. L. Hall, "Laser photodetachment determination of the electron affinities of OH, NH_2, NH, SO_2, and S_2", The Journal of Chemical Physics **60**, 1740–1745 (1974).
[62]P. C. Engelking, G. B. Ellison, and W. C. Lineberger, "Laser photodetachment electron spectrometry of methoxide, deuteromethoxide, and thiomethoxide: electron affinities and vibrational structure of CH_3O, CD_3O, and CH_3S", The Journal of Chemical Physics **69**, 1826–1832 (1978).
[63]H. Hotop and W. C. Lineberger, "Dye-laser photodetachment studies of Au^-, Pt^-, PtN^-, and Ag^-", The Journal of Chemical Physics **58**, 2379–2387 (1973).
[64]M. Bacal et al., "Measurement of H^- density in plasma by photodetachment", Review of Scientific Instruments **50**, 719–721 (1979).
[65]M Bacal et al., "Measurement of the H^- thermal-energy by 2 laser-pulse photodetachment", in Production and Neutralisation of Negative Ions and Beams, Vol. 210, edited by A Herschcovitch, AIP Conference Proceedings (1990), 489–503.
[66]C. Burkett and J. Eyler, "Dye laser-induced photodetachment of negative-ions", Abstracts of Papers of The American Chemical Society **173**, 119 (1977).
[67]H. Amemiya and T. Suzuki, "Measurement of negative ions by photodetachment with YAG laser in discharge plasmas", Japanese Journal of Applied Physics **29**, L1712 (1990).
[68]H Amemiya and T Suzuki, "Laser-assisted probing method for measuring negative ions in plasmas", Japanese Journal of Applied Physics Part 2 - Letters **30**, L1895–L1898 (1991).
[69]M. Bacal, "Plasma diagnostics in negative ion sources", Plasma Sources Sci. Technol. **2**, 190 (1993).

[70]H. Amemiya, "Plasmas with negative ions-probe measurements and charge equilibrium", J. Phys. D: Appl. Phys. **23**, 999 (1990).
[71]P. M. Bryant and J. W. Bradley, "Optimum circuit design for the detection of laser photodetachment signals", Plasma Sources Science and Technology **22**, 015014 (2013).
[72]H. Amemiya, "Probe diagnostics in negative ion containing plasma", Journal of the Physical Society of Japan **57**, 887–902 (1988).
[73]K. Okimura, T. Nakamura, and A. Shibata, "Mass spectrometry and absorption spectroscopy for oxidation of titanium target in rf magnetron sputtering", Vacuum **59**, 600–605 (2000).
[74]J. W. Bradley, S. K. Karkari, and A. Vetushka, "A study of the transient plasma potential in a pulsed bi-polar dc magnetron discharge", Plasma Sources Sci. Technol. **13**, 189 (2004).
[75]E. Bultinck, "Numerical simulation of a magnetron discharge utilized for the reactive sputter deposition of titanium nitride and oxide layers" (2009).
[76]J. W. Bradley, S. Thompson, and Y. A. Gonzalvo, "Measurement of the plasma potential in a magnetron discharge and the prediction of the electron drift speeds", Plasma Sources Sci. Technol. **10**, 490 (2001).
[77]E Bultinck and A Bogaerts, "Particle-in-Cell/Monte Carlo collisions treatment of an Ar/O_2 magnetron discharge used for the reactive sputter deposition of TiO_x films", New Journal of Physics **11**, 103010 (2009).
[78]J. Bradley, S. Karkari, and A. Vetushka, "Electric probe measurements in pulsed magnetron plasmas", Surface Engineering **20**, 186–188 (2004).
[79]K. H. Berkner, R. V. Pyle, and J. W. Stearns, "Intense, mixed-energy hydrogen beams for CTR injection", Nucl. Fusion **15**, 249 (1975).
[80]R. Janev et al., *Elementary Processes in Hydrogen-Helium Plasmas* (Springer-Verlag, 1987).
[81]R. Celiberto et al., "Dissociative electron attachment to vibrationally excited H_2 molecules involving the resonant rydberg electronic state", Chemical Physics **398**, Chemical Physics of Low-Temperature Plasmas (in honour of Prof Mario Capitelli), 206 –213 (2012).
[82]A. N. Pargellis and J. Greer, "Formation of negative hydrogen ions on cesium surfaces", Bulletin of the American Physical Society **25**, 957–958 (1980).
[83]M. Bacal et al., "Effect of cesium seeding on hydrogen negative ion volume production", Review of Scientific Instruments **69**, 932 (1998).
[84]P. J. Eenshuistra et al., "Observation of exceptionally high vibrational excitation of hydrogen molecules formed by wall recombination", Phys. Rev. Lett. **60**, 341–344 (1988).

[85]M. Lischka and A. Groß, *Hydrogen on palladium: a model system for the interaction of atoms and molecules with metal surfaces*, Recent Developments in Vacuum Science and Technology (Research Signpost, 2003).
[86]D. Wetzig et al., "Rotational alignment in associative desorption of D_2(v" = 0 and 1) from Pd(100)", Phys. Rev. Lett. **76**, 463–466 (1996).
[87]R. M. A. Heeren et al., "Investigation of the extracted H^- current in a continuously pulsed-volume negative-ion source", EPL **17**, 503 (1992).
[88]M. B. Hopkins, M. Bacal, and W. G. Graham, "Enhanced volume production of negative ions in the post discharge of a multicusp hydrogen discharge", Journal of Applied Physics **70**, 2009 (1991).
[89]M. B. Hopkins and K. N. Mellon, "Enhanced production of negative ions in low-pressure hydrogen and deuterium discharges", Phys. Rev. Lett. **67**, 449–452 (1991).
[90]M. Sode, T. Schwarz-Selinger, and W. Jacob, "Ion chemistry in H_2-ar low temperature plasmas", Journal of Applied Physics **114**, 063302, – (2013).
[91]L. Chérigier et al., "Absolute atomic hydrogen densities in a radio frequency discharge measured by two-photon laser induced fluorescence imaging", Journal of Applied Physics **85**, 696–702 (1999).
[92]T Mosbach, V. Der Gathen, and H. Döbele, "Laser diagnostics of high vibrational and rotational H-2-states", CONTRIBUTIONS TO PLASMA PHYSICS **42**, 1st Workshop on Hydrogen in the Plasma Edge, JULICH, GERMANY, OCT 19-20, 2000, 650–656 (2002).
[93]S. Kajita et al., "Measurements of hydrogen negative ion and its comparison with the molecular hydrogen spectra in divertor simulator MAP-II", Journal of Nuclear Materials **313316**, Plasma-Surface Interactions in Controlled Fusion Devices 15, 748 –753 (2003).

Appendix A

Pulsed-dc O_2 Temperature Distributions

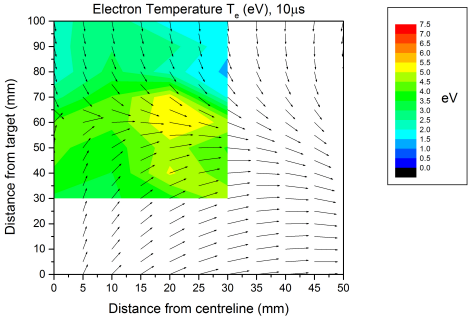

(a) 10μs

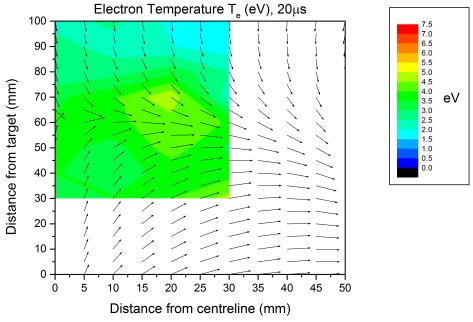

(b) 20μs

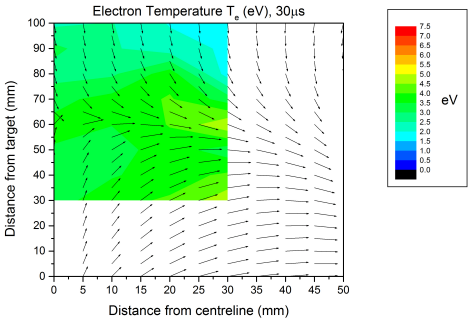

(a) 30μs

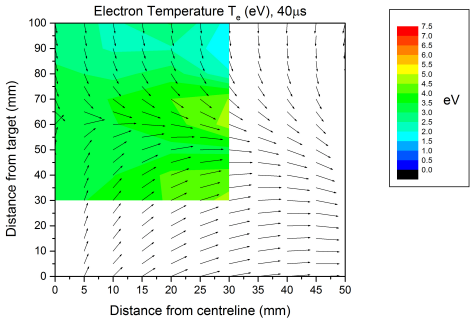

(b) 40μs

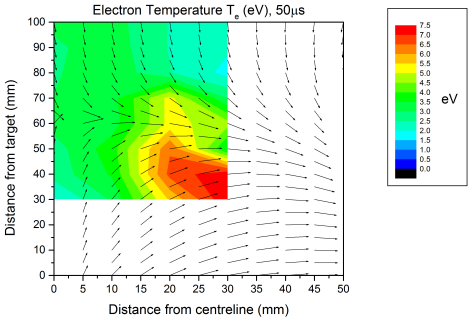

(a) 50μs

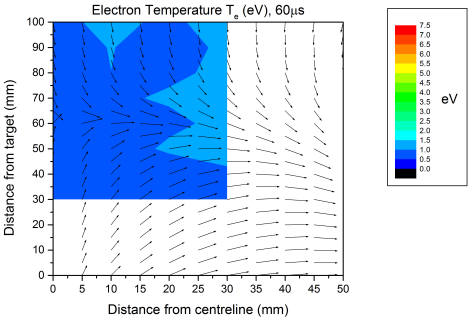

(b) 60μs

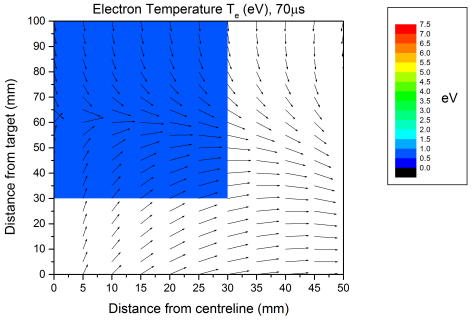

(a) 70μs

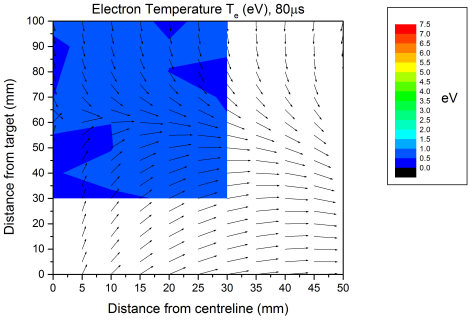

(b) 80μs

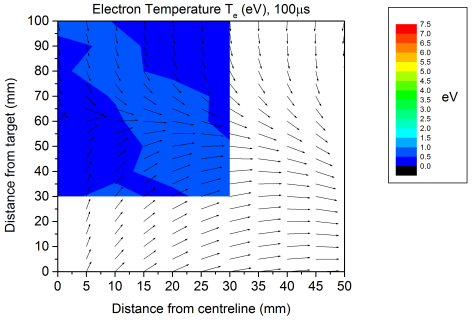

(a) 100μs

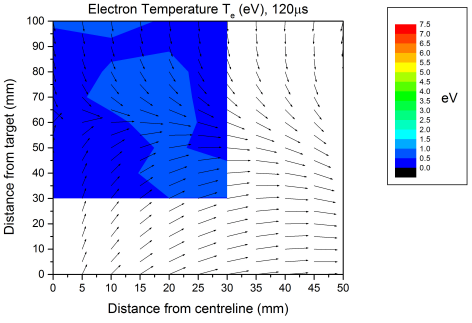

(b) 120μs

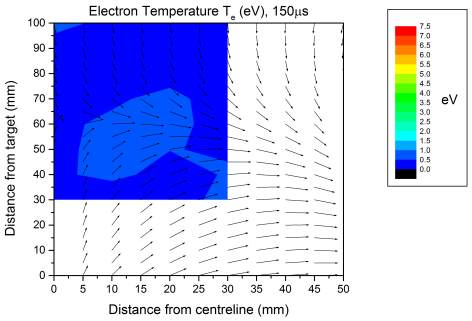

(a) 150μs

Appendix B

Pulsed-dc O_2 Potential Distributions

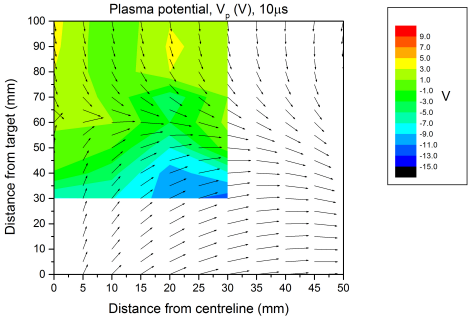

(a) 10μs

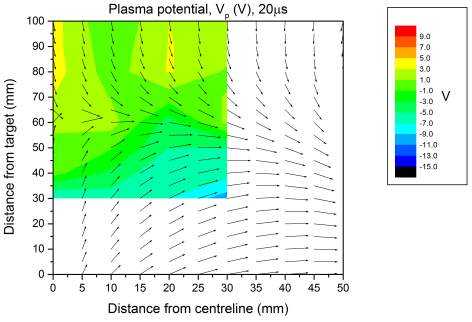

(b) 20μs

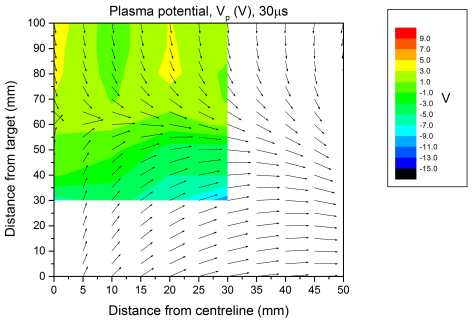

(a) 30μs

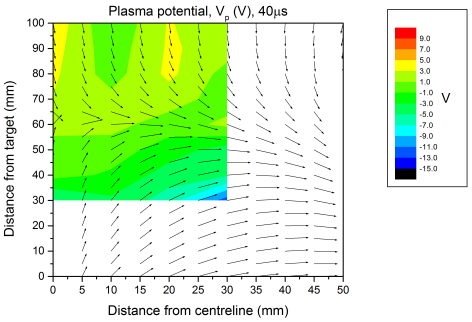

(b) 40μs

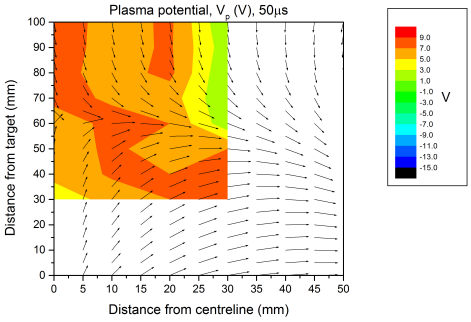

(a) 50μs

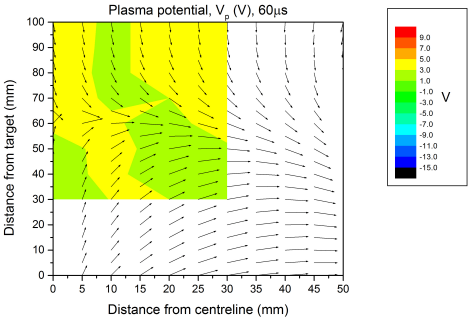

(b) 60μs

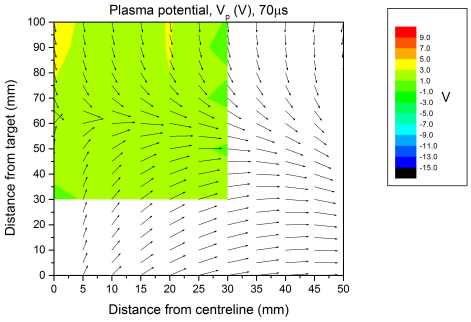

(a) 70μs

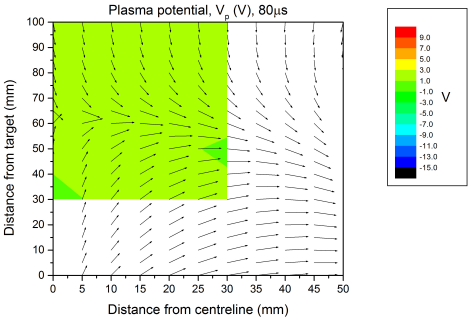

(b) 80μs

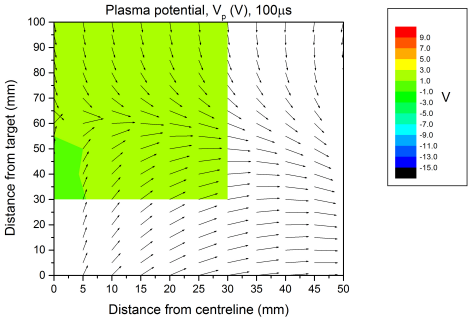

(a) 100μs

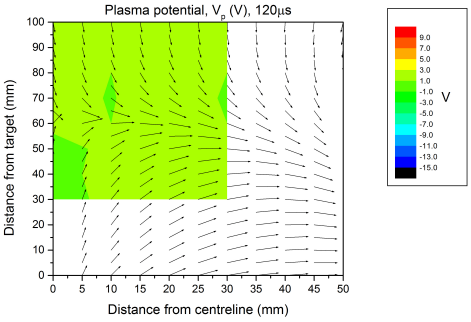

(b) 120μs

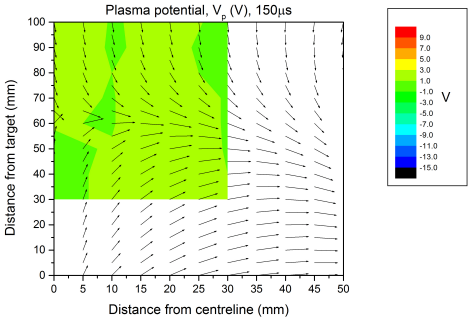

(a) 150μs